SCANNING MICRO INTERFEROMETER WITH TUNABLE DIFFRACTION GRATING FOR LOW NOISE PARALLEL OPERATION

A Dissertation
Presented to
The Academic Faculty

by

Omkar Karhade

In Partial Fulfillment
of the Requirements for the Degree
Doctor of Philosophy in the
School of Mechanical Engineering

Georgia Institute of Technology
May 2009

COPYRIGHT 2009 BY OMKAR KARHADE

SCANNING MICRO INTERFEROMETER WITH TUNABLE DIFFRACTION GRATINGS FOR LOW NOISE PARALLEL OPERATION

Approved by:

Dr. Levent Degertekin, Advisor
School of Mechanical Engineering
Georgia Institute of Technology

Dr. Thomas Kurfess, Co-advisor
Department of Mechanical Engineering
Clemson University

Dr. Steven Danyluk
School of Mechanical Engineering
Georgia Institute of Technology

Dr. Peter Hesketh
School of Mechanical Engineering
Georgia Institute of Technology

Dr. Ali Adibi
Electrical Engineering
Georgia Institute of Technology

Date Approved: December 2, 2008

To my family:

My wife, Namita

My mom and dad, Asha and Gopalkrishna

ACKNOWLEDGEMENTS

I would like to thank my advisor Dr. Levent Degertekin for his guidance and support throughout the completion of this dissertation. I would also like to thank my co-advisor Dr. Thomas Kurfess for his encouragement and support. I am grateful to both of them for making this project a great learning experience for me. It had been a great combination of freedom and direction, which made my journey through this project very exciting and fulfilling. I would also like to thank my reading committee, Dr. Steven Danyluk, Dr. Peter Hesketh and Dr. Ali Adibi for their valuable comments and support. I am thankful to Dr. Byungki Kim and Mike Schmittdiel for building the conceptual base for this project. I would also like to thank all current and former MiST and PMRC group members for their great help and many useful discussions, which helped a lot in overcoming many obstacles during this project. I am grateful to my colleagues and staff-members at the MiRC cleanroom for their help. I would like to thank MiRC and RPL for making their facilities available. I would also like to thank my wife and parents for making their love, support and encouragement.

This project was funded by the National Science Foundation (Grant # CCMI- 0200331), National Instruments and Manufacturing Research Center.

TABLE OF CONTENTS

Table of contents v

List of tables xi

List of figures xii

Summary xxii

CHAPTER 1 1

Introduction 1

1.1 Motivation 1

1.2 Problem statement 3

1.3 Thesis outline 5

CHAPTER 2 7

Literature Review 7

2.1 Existing metrology Techniques 7

2.1.1 Scanning Electron microscopy 7

2.1.2 Optical microscopy 9

2.1.3 Scanning white light interferometry 9

2.1.4 Confocal laser scanning microscopy 11

2.1.5 Scanning probe microscopy 12

2.1.6 Scanning laser Doppler vibrometry 14

2.1.7 Digital holographic microscope systems 15

2.2 Summary of literature review 17

2.3 Miniaturized Scanning Grating Interferometer (µSGI) with tunable grating 19

2.3.1 Diffraction based displacement detection using grating interferometer 21

CHAPTER 3 26

Tunable Gratings 26

3.1 Design of tunable gratings 26

3.1.1 Design requirements 26

3.1.2 Quartz based tunable gratings 27

3.1.3 Novel SOI based tunable gratings 29

3.1.4 FE modeling tool and simulations of µSGI tunable grating 31

3.2 Micro-fabrication of SOI based tunable gratings 38

3.2.1 Mask 1 layout design 38

3.2.2 Mask 2 layout design 42

3.2.3 Process development ... 44

3.2.4 Fabrication results ... 52

3.3 Characterization and comparison with FE model ... 56

3.3.1 Method and setup for characterization ... 57

3.3.2 Static characterization ... 58

3.3.3 Dynamic characterization ... 60

CHAPTER 4 ... 63

Optical Setup for micro-SGI ... 63

4.1 Table-top optical setup ... 63

4.1.1 Single μSGI table-top optical setup ... 63

4.1.2 Single μSGI table-top optical setup ... 64

4.2 Design of miniaturized optical assembly ... 65

4.3 Diffraction optics modeling and simulations ... 66

4.4 Miniaturized optical setup ... 73

4.4.1 Design of optical assembly and fabrication using stereo-lithography ... 73

4.4.2 Miniaturized assembly process sequence ... 76

4.5 Spot size measurement ... 80

4.6 Vertical resolution of the μSGI ... 83

CHAPTER 5 ... 85

Low Noise Controller for Interferometers ... 85

5.1 Design of active path stabilization ... 86

5.1.1 Methods for path stabilization ... 88

5.1.2 Harmonic distortion based path stabilization ... 89

5.2 Recurrent calibration based active control - modeling and experiments ... 99

5.2.1 μSGI system model ... 99

5.2.2 Experimental setup ... 102

5.3 Comparison of simulation and experimental results ... 104

CHAPTER 6 ... 108

Application Oriented Controller Development and Demonstrations ... 108

6.1 Parallel operation of μSGI ... 108

6.1.1 Experimental setup ... 109

6.1.2 Demonstration of parallel operation ... 109

6.2 Long range measurement implementation ... 111

6.2.1 Methods for multi-wavelength displacement measurements ... 112

6.2.2 Long range recurrent calibration based algorithm 113

6.2.3 Experimental setup 115

6.2.4 Demonstration of long range measurement operation 116

6.3 Scanning interferometry with μSGI (Case studies) 120

6.3.1 Dynamic metrology of rectangular actuable membrane with μSGI 120

6.3.2 Dynamic metrology of cantilever probe 125

6.4 Transient response measurements with μSGI 130

CHAPTER 7 132

Conclusion 132

7.1 Conclusions and contributions 132

7.2 Potential applications 134

7.3 Future work and recommendations 135

References 137

Appendices 142

7.1 Finite element code for iterative simulations of structures with varying dimensions 142

7.2 Optical setup simulation – diffraction optics based code 146

7.3 Implementation on FPGA and RT using LabVIEW..150

LIST OF TABLES

Table 1 – Summary of micro metrology techniques (modified from [39])........................17

Table 2 – Current metrology tools and comparison with the proposed tool 18

Table 3 – Dimensional variation in 5x2 arrays: 41

Table 4 – Dimensional variation in 4x2 arrays 42

LIST OF FIGURES

Figure 1 – Large area high precision metrology applications....................................2

Figure 2 – Current and desired metrology solutions 2

Figure 3 – Micromachined grating image by Scanning Electron Microscope 8

Figure 4 – Dynamic metrology by Scanning White Light Interferometry [29] 11

Figure 5 - Confocal Laser Scanning Microscope 11

Figure 6 – Schematic of Atomic Force Microscope..13

Figure 7 – A three-dimensional image of Fresnel lens array captured by digital holographic microscope 15

Figure 8: Schematic of a single μSGI - the tunable grating micro-interferometer with integrated photo-diodes and microlens 22

Figure 9 – Concept of diffraction grating interferometer..23

Figure 10 - Schematic of the optical intensity curve..24

Figure 11 – Need for parallel active path stabilization 25

Figure 12 – Quartz based tunable grating made from Aluminum.................................27

Figure 13 – Schematic of the quartz based tunable grating...28

Figure 14 – Miniaturized assembly of quartz based tunable grating 28

Figure 15 – Schematic diagram of the tunable membrane fabricated on SOI wafer (a) Cross sectional side view (b) Top view 29

Figure 16 – ANSYS multiphysics model of the tunable grating...................................... 32

Figure 17 – Meshed model showing transducer elements and structural elements 32

Figure 18 – Electrostatically actuated membrane with 25V actuation voltage 33

Figure 19 - First four modes of resonance obtained by FE analysis 34

Figure 20 – Displacement of the grating at 25V vs. membrane thickness 36

Figure 21 – Static response of the grating to the DC bias sweep 36

Figure 22 – Simulated frequency response of the tunable grating showing first 4 resonance modes 37

Figure 23 – mask 1 wafer layout 39

Figure 24 – Mask 1 - chip layout 39

Figure 25 – Mask 1 - Device layout 40

Figure 26 – Etch holes and grating fingers 40

Figure 27 – Type 1 and type 2 membrane layouts 41

Figure 28 – Mask 2 overall layout 42

Figure 29 – Chip layout for Mask 2 43

Figure 30 – Alignment mark from both masks (mask 1 - green and mask 2 - blue)........44

Figure 31 – Schematic cross section of the tunable grating membrane 45

Figure 32 – STS ICP etch etching vertical trenches to make 1 μm wide fingers 47

Figure 33 – a tunable grating after front side etching in STS ICP..................................48

Figure 34 – Tunable grating observed from the backside after backside etching...........50

Figure 35: Fabrication process sequence for the tunable grating interferometer............51

Figure 36 – A fabricated tunable grating chip 52

Figure 37 – A fabricated type 1 membrane...52

Figure 38 – A fabricated type 2 membrane layout 53

Figure 39 – Fabricated 4x2 array of tunable gratings on a chip. The devices and the substrate are wirebonded. 54

Figure 40 – Profile of the fabricated tunable grating. The tunable grating shows about 50nm upward buckling deflection 54

Figure 41 – 3D image of the tunable grating structure under DC bias actuation, obtained using an Optical Profilometer. Note that the grating remains flat.............................55

Figure 42 – Grating flatness test under profilometer, the grating is actuated with 41V electrostatic bias voltage 56

Figure 43: Experimental setup for the characterization of μSGI 57

Figure 44: Deflection of grating vs. actuation voltages 58

Figure 45 – Static characterization of multiple devices (tunable gratings) on a chip. Nomenclature indicates the location of the tunable grating e.g. L3 = 3 rd tunable grating from top in the left column of tunable gratings 59

Figure 46 – Measured and FE modeled frequency response of the μSGI tunable grating 60

Figure 47 – Frequency response of multiple tunable gratings on a chip......................... 61

Figure 48 – Schematic of table-top optical setup for single μSGI operation 63

Figure 49 – Schematic of table-top optical setup for single μSGI operation 64

Figure 50 – Mismatching wavefronts interfere to generate circular fringes inside a fringe 65

Figure 51 – Schematic of the micro optical system... 66

Figure 52 – Optical intensity profiles of the beam traveling from the collimator to the microlens (obtained from simulation) 68

Figure 53 – Optical intensity profiles of the beam traveling from the microlens to the photo-detectors (obtained from simulation).. 69

Figure 54 - Optical intensity profiles of the beam traveling from the grating to the photo-detectors when no lens is used (obtained from simulation) 70

Figure 55 – Optical curve obtained from the simulations 71

Figure 56 – Sample optical curve obtained from experiments 72

Figure 57 – Circular fringes generated by the table-top setup 72

Figure 58 – No significant circular fringes are generated by the miniaturized assembly setup.. 73

Figure 59 – Schematic of the miniaturized assembly.. 74

Figure 60 – 3D view of the holder structures and their extensions 75

Figure 61 – Fabricated holders for miniaturized assembly 76

Figure 62 – Miniaturized assembly process sequence 1 77

Figure 63 - Miniaturized assembly process sequence 2 78

Figure 64 – Miniaturized assembly using XYZ stages and sample placed on actuator .. 79

Figure 65 – Miniaturized assembly placed inside a shielded box 80

Figure 66 – Miniaturized μSGI package mounted on a XYZ stage for alignment 80

Figure 67 – Spot size measurement sample.. 81

Figure 68 – Spot size measurement with lens integration – raw data.......................... 82

Figure 69 – Spot size measurement amplitude envelope 82

Figure 70 – Vertical displacement resolution from noise measurements...................... 83

Figure 71 - Schematic of the optical intensity curve..85

Figure 72 – μSGI active noise control system – block diagram 87

Figure 73 – Normalized optical intensity curve for the first diffraction order 88

Figure 74 – Schematic of the harmonic distortion based active path stabilization implemented by Kim and Schmittdiel [70] 90

Figure 75 – A 6 point DFT method implementing harmonic distortion based noise reduction algorithm..94

Figure 76 – Reduction of noise using a 6 point DFT algorithm. The second harmonic shown by f_2 is reduced by the controller and the first harmonic f_1 which is proportional to the sensitivity is increased...95

Figure 77 – 8 point DFT for second harmonic. The second harmonic sinusoid shows the multiplication constants. A sample PD output is used to demonstrate the calculation of the amplitude of the second harmonic 97

Figure 78 – A 4 pt DFT for the first harmonic. The first harmonic sinusoid shows the multiplication constants. A sample PD output is used to demonstrate the calculation of the amplitude of the first harmonic. 98

Figure 79 – Frequency response of the tunable grating obtained from the experiments and the second order approximation of the curve in discrete (z) domain at 180 kHz. 100

Figure 80: Schematic of the active control of tunable grating system...........................101

Figure 81: Root-locus plot of the open loop control 101

Figure 82 – Bode diagram of the closed loop controller..102

Figure 83 – Experimental setup used for demonstration of the active control scheme.103

Figure 84 – Experimental results of the active noise reduction....................................104

Figure 85 – Noise reduction performance – comparison of simulation and experimental results...105

Figure 86 – (A) Blue – without lookup positive gain (B) Green – without lookup negative gain (C) Red – with lookup positive or negative gain. 106

Figure 87 – Experimental setup used for demonstration of the active control scheme.109

Figure 88 - Parallel active noise reduction using two μSGIs on the same chip. (μSGI 1 - blue, μSGI 2 – pink) (a) Both controllers off (b) Controller 1 on, controller 2 off (c) Controller 1 off, controller 2 on (d) Both controllers on..110

Figure 89 – High-pass filtered data. (a) PD1 output with controller off (b) PD1 output with controller 1 on...111

Figure 90 – The quadrature output using harmonic distortion method 112

Figure 91 – Long range detection algorithm – The displacement measurement is done at three different resolutions 1) High frequency (>6.5kHz) high resolution (<0.1 pm/√Hz) data acquisition using path stabilized μSGI 2) Low frequency (<6.5kHz) low resolution (nm level) data acquisition using grating motion, has limited range (λ/4) 3)

Low frequency (<6.5kHz) low resolution (λ/4) data acquisition using grating jump count.......... 114

Figure 92 – Experimental setup to show long range high resolution operation of μSGI115

Figure 93 – High frequency low amplitude vibration obtained from high resolution data acquisition 116

Figure 94 – Low frequency vibrations obtained from the surface tracking of the grating (over 500ms and zoomed in over 100ms).......... 117

Figure 95 – Long range motion obtained from the grating jump counting (over 500ms and zoomed in over 100ms).......... 117

Figure 96 – Addition of low frequency vibration measurement (blue) and jump counting measurements (green) gives total displacement measurement (red) 118

Figure 97 – Total displacement obtained from addition (over 500ms and zoomed in over 100ms) 119

Figure 98 – Grating jump event stabilization time - during this time true high resolution measurement can not be obtained.......... 120

Figure 99 – Rectangular actuable membrane used as sample.......... 121

Figure 100 – Raster scan of the membrane structure.......... 122

Figure 101 – A reflectivity profile of the sample obtained by μSGI 122

Figure 102 – Vibration amplitude map directly measured from photo-detector signal .. 123

Figure 103 – Vibration amplitude map of the membrane 124

Figure 104 – Veeco NP-20 silicon nitride probe [83]... 125

Figure 105 – Reflectivity image of the cantilever 126

Figure 106 – Sensitivity corrected vibration amplitudes in second mode 127

Figure 107 – Phase map of the cantilever showing phase change at node in second mode 128

Figure 108 – Vibration amplitude image of the cantilever in its second resonance mode 129

Figure 109 – Phase map of the cantilever in its second resonance mode.................... 130

Figure 110 – Transient response of the cantilever to an impulse input, obtained using μSGI 131

Figure 111 – The frequency response of the cantilever obtained from the transient response.. 131

Figure 112 – LabVIEW FPGA code – block 1 receives the calibration chart (non-linearity lookup table) from the RT... 151

Figure 113 – Step 2 – Finding the desired point of operation by calibration of the optical curve.. 152

Figure 114 – Step -3 (half screen) The setpoint is found and PID control with gain reversal and look-up table is implemented. 153

Figure 115 – Step 3- second half of the screen 154

SUMMARY

Large area high throughput metrology plays an important role in several technologies like MEMS. In current metrology systems the parallel operation of multiple metrology probes in a tool has been hindered by their bulky sizes. This study approaches this problem by developing a metrology technique based on miniaturized scanning grating interferometers (μSGIs). Miniaturization of the interferometer is realized by novel micromachined tunable gratings fabricated using SOI substrates. These stress free flat gratings show sufficient motion (~500nm), bandwidth (~50 kHz) and low damping ratio (~0.05). Optical setups have been developed for testing the performance of μSGIs and preliminary results show 6.6 μm lateral resolution and sub-angstrom vertical resolution. To achieve high resolution and to reduce the effect of ambient vibrations, the study has developed a novel control algorithm, implemented on FPGA. It has shown significant reduction of vibration noise in 6.5 kHz bandwidth achieving $6x10^{-5}$ $nm_{rms}/\sqrt{Hz}$ noise resolution. Modifications of this control scheme enable long range displacement measurements, parallel operation and scanning samples for their dynamic profile. To analyze and simulate similar optical metrology system with active micro-components, separate tools are developed for mechanical, control and optical sub-systems. The results of these programs enable better design optimization for different applications.

CHAPTER 1

INTRODUCTION

1.1 Motivation

In recent years, growing quality control standards and drive towards miniaturization [1] have posed many challenges to the modern spatial metrology. Static as well as dynamic spatial metrology has become critical in many applications like vibration analysis, precision machining, biomedical applications etc. [2-4] (Figure 1). Micro electro mechanical systems (MEMS) like microphones, accelerometers, digital light processing DLP® systems and infrared imaging systems etc. are emerging with a need for higher precision measurements of the profile and motion of their micro-components [5-8]. Many times, measurements need to be taken at multiple points over a large area on the sample simultaneously e.g. study of acoustic wave propagation. Many micro-systems are manufactured in the form of arrays due to which fast multiple sample metrology has become very important for high yields. Multiple point metrology systems are highly desired for measurement of such systems. Such multi-probe system with probes measuring in parallel gives is useful for improving the yield. Schematic of a multiple point metrology probe system is shown in Figure 2. However, these systems are extremely challenging because it introduces stringent size constraints on each of the metrology probes.

For most of these systems, non-contact methods are preferred to avoid damage to the critical surfaces. However, non-contact methods are prone to environmental vibrations. Reduction of vibration noise and positioning errors has posed another challenge for high resolution metrology. It is even more challenging to achieve noise reduction in a multi-

probe metrology system because of the non-uniformity of the noise over the sample surface.

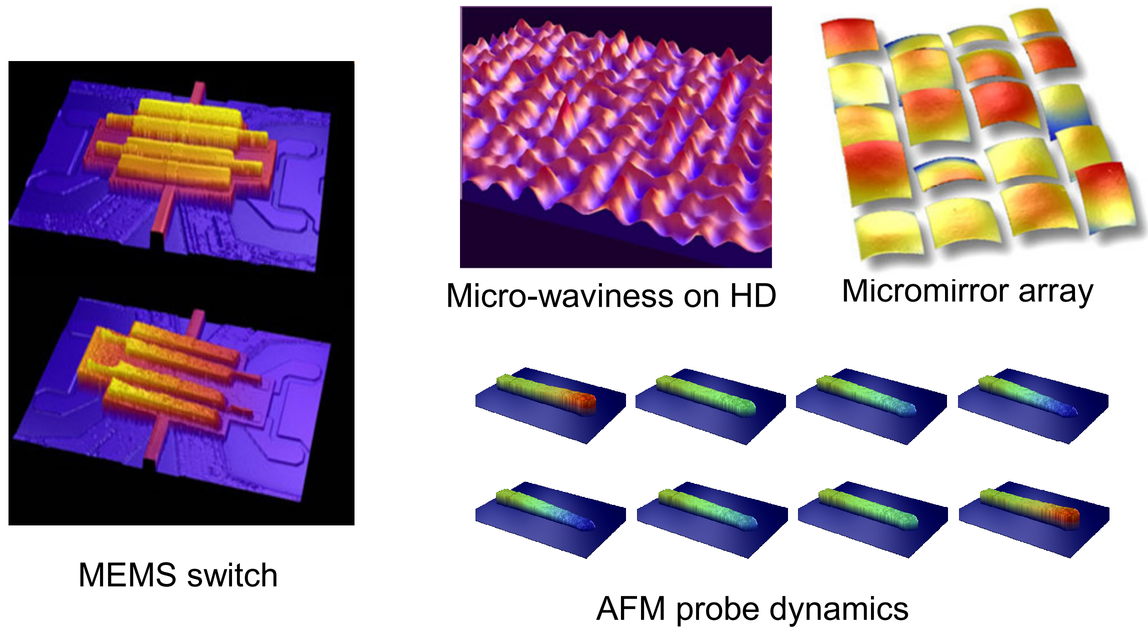

Figure 1 – Large area high precision metrology applications

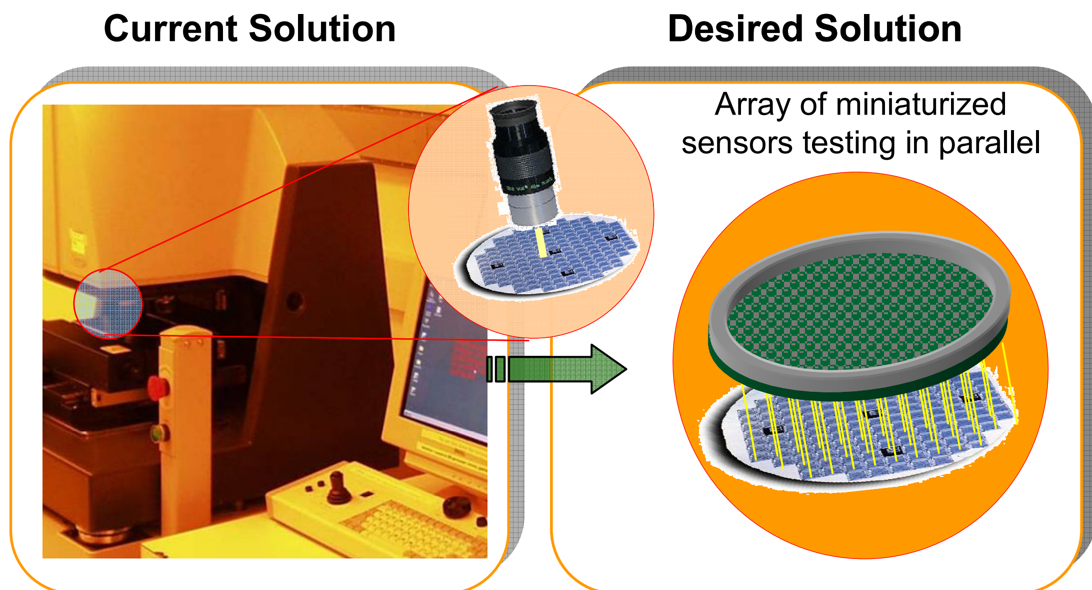

Figure 2 – Current and desired metrology solutions

The bandwidth of the dynamic measurements determines the maximum detectable frequency of sample vibrations. Many MEMS like (Radio Frequency) RF-MEMS [9, 10], (capacitive Micromachined Ultrasonic Transducers) cMUTs [11] or surface wave profiling [12] show bandwidth of several MHz to GHz. Current systems are limited to stroboscopic methods for dynamic metrology which has limited bandwidth (a few MHz – discussed in CHAPTER 2).

Thus, several short-comings in the current technology have been responsible for the unsatisfied needs for this type of metrology. This research aims to fill some of this gap in the technology by further investigating the problem and developing solutions to it.

1.2 Problem statement

As mentioned earlier, the current metrology systems lack one or more characteristics like high resolution, dynamic measurements, fast, high bandwidth, low noise, long range and non-contact operation. The current metrology tools can scan very small areas at a time and simultaneous multiple point measurements are not possible because of their bulky size. High resolution metrology techniques like AFM are limited in range and often are contact-based limiting their use only on hard samples. Non-contact techniques are prone to vibration noise which not only distorts the signal but also affects the resolution. Dynamic metrology has been limited to stroboscopic methods which are currently limited to a few MHz. The growth of MEMS has been suffering from the lack of in-line metrology capability [13]. A small metrology tool which can measure large surfaces in a very short time can have significant impact on the MEMS fabrication and higher yields may help MEMS realize the potential market.

This study aims to fill some gap in the metrology area by developing a miniaturized metrology tool with many desired properties, and which can also be operated in parallel.

The research problem involves several engineering fields i.e. mechanical design, MEMS fabrication, controls and optics. Hence, the effort is in to subtasks. These tasks aim to fill small technology gaps in different fields and may have impact in many different technologies.

- Investigate the feasibility of a tunable grating based μSGI array. Based on the feasibility, design a novel array of tunable gratings with sufficient range of motion under low actuation voltages, with sufficient dynamic bandwidth, low squeezed film damping and flat grating under actuation. Develop a finite element (FE) based analysis tool to analyze the static and dynamic performance of the designed tunable membrane under actuation. Develop a fabrication scheme for the designed μSGIs and implement it. Develop methods to characterize the tunable gratings and implement them. This research can be useful for many membrane based devices like RF-MEMS [10], microphones [14] etc. and could be beneficial to the related technologies.

- Investigate different control schemes for fast active tuning of the gratings, for their ability to significantly reduce the low frequency ambient vibrations. Develop a simulation and analysis tool, for design and optimization of the control algorithms. Develop the control algorithm to achieve parallel operation. Extend the algorithm to deal with the non-linearities incurred with electrostatic actuation and measure distances longer than half wavelength. Extend the algorithm to obtain reflectivity, vibration amplitude and phase information. Enable scanning of samples.

- Develop optical setups for long range and good lateral resolution. Develop an optical analysis tool to aid the design process and optimize performance of the setup. This tool may easily be extended for design and analysis of many other

similar optical systems. Miniaturize the optical setup and develop process for integration.

- Develop experiments and required setups to demonstrate the capabilities of the μSGI using case studies.

1.3 Thesis outline

Realizing the benefits of the micro-machined grating interferometers, this study builds on the concept of the μSGIs introduced by Kim et al. [15]. CHAPTER 2 reviews the existing metrology techniques. It also introduces the concept of diffraction based μSGIs, their active control and miniaturized assembly of the components.

The μSGIs use tunable gratings which can be actuated for noise cancellation. These tunable gratings are discussed in detail in CHAPTER 3. It discusses the design of the tunable gratings and finite element modeling for simulation of the tunable gratings. It also explains the mask layouts and the details of the fabrication process. The fabricated tunable gratings are tested and characterized for their static and dynamic performances which are also discussed in the chapter.

CHAPTER 4 discusses the optical setups developed for μSGI experiments. It explains the diffraction optics based analysis used for the design of optical setups. It explains the design and fabrication of miniaturized setup and characterizes the optical setups.

CHAPTER 5 discusses different active path stabilization algorithms of the tunable gratings. It also introduces a novel active control algorithm for the tunable gratings. A model of the control system is built to design an efficient active noise cancellation system; the comparison of the results from the simulations and the experimental results is discussed in this section.

CHAPTER 6 discusses the development of the control algorithm to achieve different capabilities. It demonstrates the parallel operation, long range operation and scanning of dynamic micro-components.

CHAPTER 7 details the conclusions, contributions and future work.

CHAPTER 2

LITERATURE REVIEW

With the drive towards miniaturization and growing quality control standards, metrology of micromachined components becomes critical. Tools for metrology of micromachined components are primarily derived from the techniques of the semiconductor industry. These tools are typically limited to lateral dimensions and are insufficient for measuring the overall part geometry of micromachined mechanical components. The micromachined components can also have moving parts and the dynamic behavior of the component may be critical to the operation. In such cases the metrology tool needs to be able to measure the dynamics of the component. This chapter surveys the current state of the art in metrology of micromachined components. Each technique is presented with its advantages and disadvantages in this context.

2.1 Existing metrology Techniques

2.1.1 Scanning Electron microscopy

One of the primary tools used for analysis of MEMS devices is the scanning electron microscope (SEM). SEMs are capable of producing high resolution images of conductive objects on the angstrom scale. SEMs operate by scanning a focused beam of high energy electrons across a conductive sample contained in a vacuum. As the electron beam hits the conductive surface, secondary electrons are knocked loose. These secondary electrons are counted and used to create an image of the sample. Current commercial SEMs offer 0.4 nm lateral resolution and magnification up to 2 million times [16]. An example of three-dimensional image captured by an SEM is shown in Figure 3.

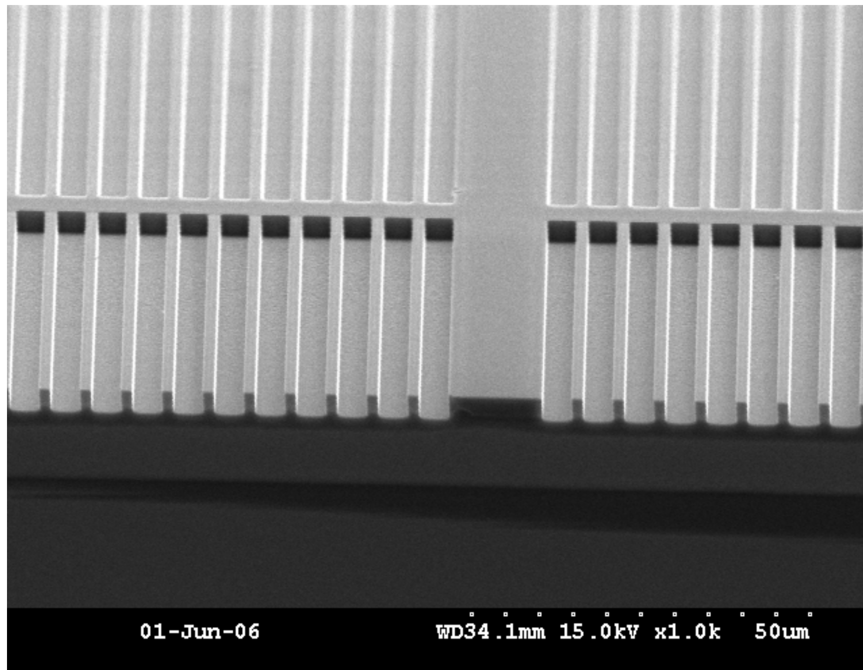

Figure 3 – Micromachined grating image by Scanning Electron Microscope

SEMs scan the sample at video rate hence measurement of high frequency dynamic vibrations becomes difficult. The frequencies that are multiples of the video rate can be strobed with SEMs. For other frequencies Gilles [17] showed that the amplitude of lateral vibrations can be estimated by the blur area to find the Q-factor of dynamic devices in a vacuum. Wong [18] implements dynamic stroboscopic in-plane imaging by time-gating the secondary electron detector signal to achieve 3.58 MHz bandwidth 24 nm resolution dynamic measurements with instantaneous velocities obtained by pixel blurring analysis.

In another study, Storment, Borkholder et al. [19] noticed warping in delicate MEMS devices after imaging them using an SEM. It was noted that the rapid evacuation of the chamber before creating the SEM image was most likely the cause of the warping. The vacuum requirement also makes operation of SEM difficult.

An alternative SEM process is called X-SEM. This process is destructive and requires the sample to be cross-sectioned. The cross-section is then imaged in an SEM. Often

this technique is used to determine sidewall and height characteristics [20]. Lagerquist, Bither et al. [21] discuss use of the X-SEM process to characterize top-down SEM images, which require interpretation of intensity and are sensitive to sidewall geometry.

2.1.2 Optical microscopy

The underlying operating principles for optical microscopes include spatial resolution determined by the Rayleigh criterion and detected edge sharpness determined by a combination of hardware (e.g. lens type, CCD camera) and lighting conditions (e.g. coaxial lighting, ring lighting).

Optical microscopes have the advantage of being fast and non-destructive. Optical microscopes tend to be repeatable for features as small as 0.25 μm. The limiting factors for resolution of optical metrology hardware are diffraction and the ability to produce images with clear intensity changes. Other significant errors of optical techniques typically stem from interference, resonance, shadowing, secondary reflections, and lens distortions [22, 23].

An important limitation of optical microscopes for inspection is the inability to acquire true three-dimensional data. Using a stroboscopic method, in-plane dynamic motions can be measured; however, dynamic measurement of out-of-plane dimensions is difficult. Petitgrand and Bosseboeuf [24] showed that an optical microscope can be combined with a phase shifting stroboscopic interferometer to obtain sub-nanometer resolution three-dimensional dynamic measurements.

2.1.3 Scanning white light interferometry

Another method of inspection is scanning white light interferometry (SWLI). Although initially developed for surface characterization, such as finding surface roughness, SWLI is currently being used to make dimensional measurements of micromachined parts [25].

White light interferometers have sub-nanometer resolution in the scanning direction, at best sub-micrometer resolution in the lateral directions, and can be used on a multitude of parts with different surface finishes [26].

An interferometer works on the principle of interference. Within the objective, a light beam is split, with one beam going to the object surface and the other to a reference surface. These light waves bounce back and interfere with each other, forming a pattern of light and dark bands, called fringes. For scanning interferometers, a piezoelectric crystal is used to create small movements in the objective perpendicular to the surface of interest. As the reference surface within the objective moves, the result of the combination of the reflected light varies. Several images are captured and then combined. Based on the interference pattern, or fringes, and the wave length of light employed, it is possible to extract coordinate data [27].

White light is commonly used in scanning interferometers because it allows for higher resolution by comparing data from multiple wavelengths. Additionally, it is possible to resolve step height changes greater than lambda/4 [28]. SWLI has the ability to quickly measure step height changes and deflections. Additionally, when integrated with an image processing system, SWLI can provide lateral dimensions.

Dynamic metrology can be achieved with a white light interferometer using stroboscopic illumination. Veeco's DMEMS [29] system offers 15 Hz to 1 MHz frequencies and 0.1 nm scale resolution. The synchronized capture of a set of three-dimensional measurement data is used to generate a video. An example of dynamic motion measurement is shown in Figure 4, which shows the motion of a cantilever at its resonant frequency.

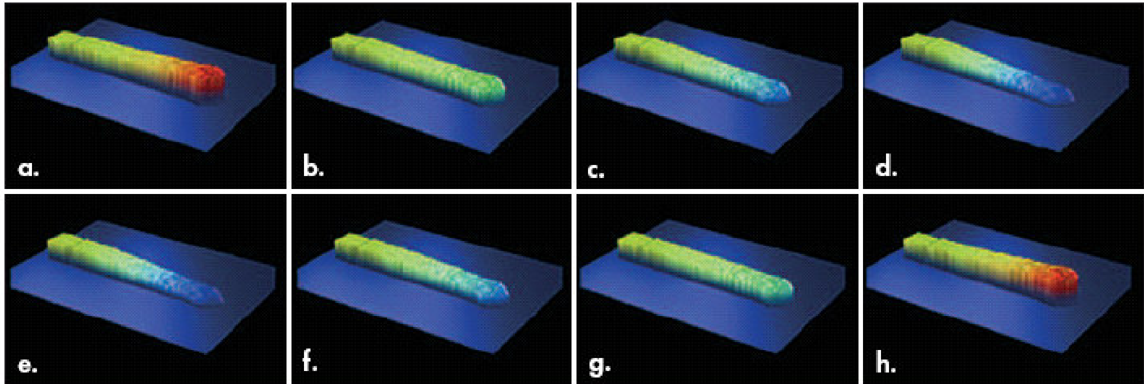

Figure 4 – Dynamic metrology by Scanning White Light Interferometry [29]

2.1.4 Confocal laser scanning microscopy

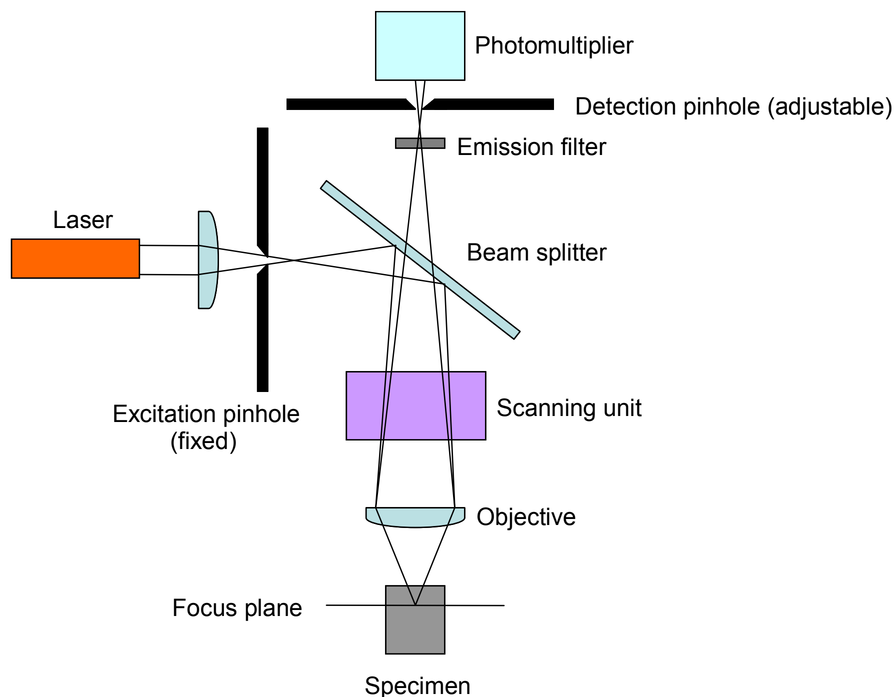

Figure 5 - Confocal Laser Scanning Microscope

Confocal Laser Scanning Microscopy (CLSM) combines a confocal microscope with a scanning system in order to gather a three-dimensional data set. Confocal microscopy is different from conventional microscopy in that it creates an image point by point. CLSM uses a double pinhole lens system (Figure 5). It allows the system to focus on a single plane. A different plane can be imaged by moving the detection pinhole. With a scanning

system added, the system has the ability to scan multiple times on different imaging planes, resulting in a three-dimensional data set. Dimensional measurements are in the range of micro-meters with nanometer accuracy. Scanning can be performed in several different ways, it is most often done by moving the beam, which alleviates focus problems caused by objective lens scanning and is faster than specimen scanning [30].

One of the most important advantages found is the ability of the microscope to measure steep slopes, up to almost 90 degrees on a part with minimal surface roughness. This measurement requires a high-resolution, high-numerical aperture objective, which has a limited lateral measuring field unsuitable for measuring the entire object. Because of this limitation, a stitching procedure is needed to combine scans taken with several objectives (Sung, et al., 2004; Ulmann, et al., 2003).

Shin et al, designed and constructed a single-fiber-optic confocal microscope (SFCM) with a microelectromechanical system (MEMS) scanner and a miniature objective lens [31]. Axial and lateral resolution values for the system were experimentally measured to be 9.55 μm and 0.83 μm respectively, in good agreement with theoretical predictions. Reflectance images were acquired at a rate of 8 frames per second, over a 140 μm x 70 μm field-of-view. In anticipation of future applications in oral cancer detection, they imaged ex vivo and in vivo human oral tissue with the SFCM, demonstrating the ability of the system to resolve cellular detail.

2.1.5 Scanning probe microscopy

Scanning probe microscopes (SPMs) offer a high resolution (sub-angstrom) alternative to non-contact techniques. The two most widely used SPMs are the scanning tunneling microscope (STM) and the atomic force microscope (AFM). The older of the two technologies, the STM, uses a metallic probe that is brought into close proximity of a

conductive surface so that a small current flows between the probe and surface. The current is held constant by a feedback control scheme, allowing the probe to track the height of the surface [22]. Sub-angstrom resolution is attainable in the normal direction of the surface, and angstrom-scale resolution is attainable in the lateral direction of the surface.

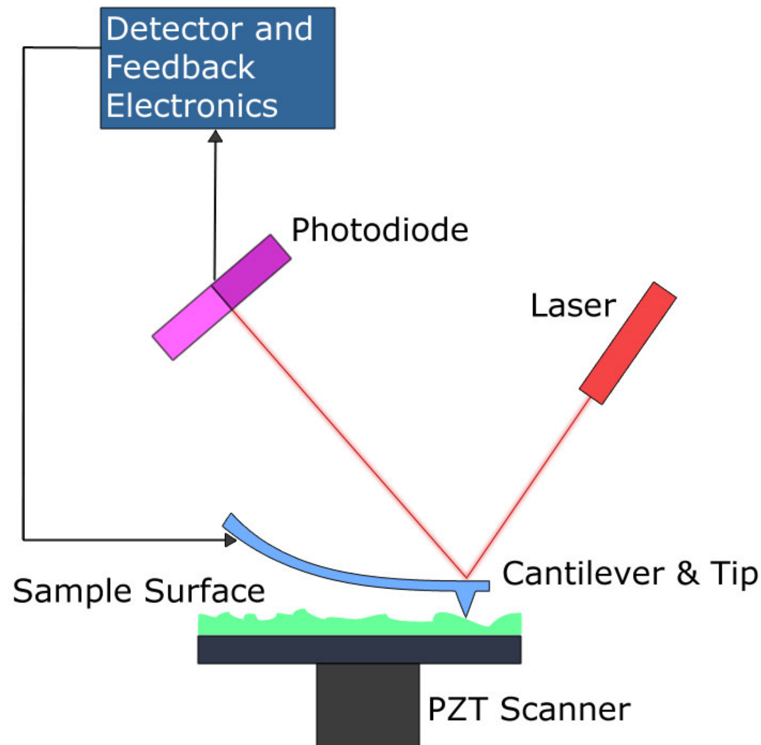

Figure 6 – Schematic of Atomic Force Microscope

Atomic force microscopy is the newer SPM technology and retains the resolution of the STM, but is not limited to conductive surfaces [32]. A schematic of AFM is shown in Figure 6. The measurements of an AFM are performed with a sharp probe that collects a series of line scans across the surface of a part. The topography of the part is measured by bringing the probe close to the specimen and measuring the repulsive and attractive forces on the probe tip. Though having the advantage of not contacting the surface of the specimen and therefore eliminating tip erosion [33], this method has lower resolution

and is less stable than either the sliding or tapping modes. The SPMs have atomic resolution but are limited to a few micrometers level range [34].

Dynamic measurements can be achieved by high speed AFMs scanning at fast rate using a mechanical feedback loop and resonant scanning mechanism [35]; however this is a contact method. Onaran and Van Gorp [6, 36] developed an AFM with force sensing integrated readout and active tip (FIRAT) with high bandwidth actuator, high interferometric resolution and extended-range. This is an active area of research.

2.1.6 Scanning laser Doppler vibrometry

Laser Doppler vibrometry (LDV) is a non-contact vibration measurement technique using the Doppler effect. LDV is designed to measure the dynamic motions of components.

It typically includes two-beam interferometric devices that detect the phase difference between an internal reference and the measurement beam. A scanned laser spot measures the dynamic profile of a surface under observation. Lawrence et al. used LDV to measure the dynamic vibrations of a two-axis micromirror MEMS [37].

By itself LDV is insufficient to measure the topography of a sample surface. To complete this system, Polytec Inc. combined scanning LDV with a scanning white light interferometer [38].

2.1.7 Digital holographic microscope systems

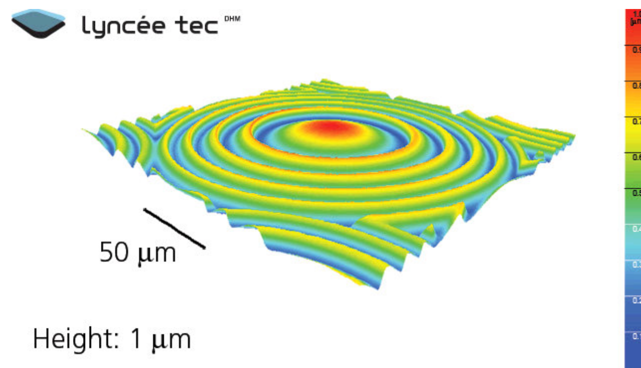

Figure 7 – A three-dimensional image of Fresnel lens array captured by digital holographic microscope

Digital holographic systems have been employed for many years to measure vibrating devices. In this technique, a digital camera is used to record a hologram produced by interfering a high-quality reference beam with a beam reflected from the sample under test. As the test object is later deformed, the modified object beam is compared with the original digitally recorded hologram, and the deformation can be quantified using standard phase-shifting or other interferometric techniques. These systems can therefore achieve nm-level measurement of out-of-plane motion of devices. An image of a three-dimensional structure captured by a Digital Holographic Microscope (DHM) is shown in Figure 7. Using high-speed cameras deformations of up to several thousand hertz can be measured. The systems can also be combined with stroboscopic methods to measure motions up to several MHz [39].

Off-axis configuration enables capturing entire part information by a single image acquisition. The image can be reconstructed at any object plane and the DHM can work from long distances (20-30 cm). The lateral resolution can be substantially high (i.e. ~300 nm) and vertical resolution can range from 27 nm [40] to interferometric (0.2 nm). However, this resolution is either for static or a low bandwidth measurement. Including

the processing time, with 1000 nm lateral resolution, 100 ms is sufficient time to scan and reconstruct a 1 mm x 1 mm area. [41].

There are different methods of image reconstruction, including the Fresnel-approach, Fourier approach, and convolution-approach. Lensless Fourier Holography is the fastest and most suitable algorithm for small objects. Lateral resolution ranges from a few micrometers to hundreds of micrometers without any additional optics [42]. Phase unwrapping is still necessary in digital holography since the fringe-counting problem remains.

In the time averaged Electro-optic holographic microscope (EOHM) (the sample is vibrated at one of its resonant frequencies. The sample is exposed for an extended period of time (relative to the time period at that frequency) to capture a single image. The reconstruction of this image involves interference of all the positions incurred by the moving sample. The zero velocity points on the sample lead to the strongest contributions to the reconstruction and the maximum velocity points lead to lowest contributions. The reconstruction is computationally more involved and is often approximated by look-up tables [43]. This method can show the mode shape at a particular frequency. It is easy to use this method to find the resonant frequencies and mode shapes. The bandwidth of operation is not limited, but in the time domain only one frequency can be analyzed in a given measurement.

The DHM method also may suffer from aberrations such as spherical (for off-axis configuration), coma or astigmatism, field curvature, or distortion [44].

2.2 Summary of literature review

Table 1 – Summary of micro metrology techniques (modified from [39])

Method	Measurement Outputs	Approximate Resolution	Major Advantages	Major Disadvantages	Key Options
Optical Microscopy	2D Static In-plane Dynamic	X.Y: 0.4µm Lateral Motion: 10nm	Cost. Speed. Ease of use. Variable fields. Long working distance. Measure through glass or films	No vertical information	Blur analysis Strobing. Image processing. Dark-field.
Scanning Electron Microscope	3D Static	X.Y: nm-level Z: nm-level	High aspect ratios Variable fields Sidewall angles	Ease of Use, Vacuum No packaged devices No dynamic	Magnification range. stages
Confocal Microscopy	3D Static	X.Y: 0.4µm, Z: nm-level	Ease of Use. Variable fields High angles	Vertical resolution NA. No dynamic	Film thickness. Image processing automation
Scanning Probe Microscopy	3D Static characteristic Atomic scale roughness	X,Y: nm-level Z: 0.1nm	Highest lateral and vertical resolution Magnetic. electrical characterization	Ease of Use. Speed. Vertical Range. No packaged devices No dynamic	Tapping mode. Different tip geometries, enclosure. sidewall roughness
Laser Doppler Vibrometry	Out-of-plane Dynamic	X.Y spot size: about 1µm Out-of-plane Motion: 1nm, 0.1pm/√Hz	Speed. Out-of-plane resolution. True transient motion.	Sensitive to surface texture, no static, Out-of-plane only	Area scans. Different frequency ranges. Strobed microscope for in-plane
Digital Holographic Systems	In and out of plane dynamic motion	X,Y: 1µm Out-of-plane Motion: 1nm	Speed. modal analysis	Not good static capability,	Hologram resolution, phase and amplitude capability.
Scanning Optical Interferometry	3D Static, In-Plane Dynamic, Out-of-Plane Dynamic,	XY: 0.4µm Z: <1nm, In-Plane Motion: 5nm,Out of Plane Motion 1nm	Can measure most required parameters	Angles > 35 degrees not possible. Slower for dynamic than LDV	Image processing Film thickness Dynamic capability. through-glass objectives
(Proposed) µSGI Miniaturized Scanning Grating Interferometer	3D static, out-of-plane dynamic, metrology at multiple sample points	X,Y: 5µm, Z: 0.8 A°, Motion: Z: 0.06pm/√Hz	True transient motion, high out of plane resolution, static + dynamic, Parallel	Angles > 35 degrees not possible	Active noise control, custom placement and orientation

			measurements, Size 12mm2 per device		

As mentioned earlier, the current metrology systems partially satisfy the requirements like high resolution, dynamic measurements, fast, high bandwidth, low noise, long range and non-contact operation. Table 1 lists the current metrology techniques and compares them based on the parameters under consideration. (Note: For comparison, the last rows in these tables list the specifications of the proposed metrology tool, obtained from the preliminary results, which are discussed in detail later in this report.) Table 2 lists some of the current tools and their specifications.

Table 2 – Current metrology tools and comparison with the proposed tool

Instrument	**Static performance**			**Dynamic performance**		**Benefits**	**Limitations**
	Vertical resolution	Lateral resolution	Field of view	Vertical resolution	Bandwidth		
Veeco DMEMS NT-3300 [29]	<1Å			≤1nm	15 Hz to 1MHz	Static and dynamic together.	Stroboscopic, Size
Wyko NT9800 System [45]	<0.1nm	0.1 to 13.2µm	8.45mm-0.05mm	NA	NA		size 124cmX 77cmX154cm
HS10 long-range laser scale [46]	NA	NA	NA	79 nm	NA	Up to 60m	No static
TMS-100 TopMap Metro.Lab [47]	20nm	47µm	35mmX22 mm	NA	NA	Compact	Low resolution
MSV-400 Microscope Scanning Vibrometer [48]		1µm	100 µm x 70 µm	0.1pm/√Hz	20MHz	3D Dynamic characterization, vertical resolution	Limited FOV, no static
Dimension 5000 Scanning Probe Microscope [49]	<0.5 Å in acoustic hood	<1.8nm	~90 µm square	1nm	0.1Hz-5KHz	Good lateral and vertical resolution	Contact device, size, low bandwidth, slow
Dektak 150 [50]	1Å	NA	55mm	NA	NA		
Lyncee Tec DHM [51]	0.2nm	300nm	4.40mm	~1nm	15 fps	Good lateral and vertical	Low bandwidth

						resolution	
μSGI Miniaturized Scanning Grating Interferometer array	<1Å	1μm	No limit (Discrete set of points)	<0.1pm/√Hz	GHz range	Lateral/vertical resolution, dynamic vertical, compact, flexible placement, parallel operation	Scanning is slow

It can be seen from Table 1 that the conventional scanning optical interferometry is one of the ideal metrology systems because it offers high resolution, large bandwidth, phase information and is non-contact. It is being used extensively for precise static and dynamic displacement metrology. However, it can measure a small area at a time (~1mm^2) [52] and larger samples are measured by moving the sample relative to the interferometer [53, 54] which is relatively slow because of slow mechanical motion of the sample. Implementation of multiple-point metrology has been hindered by the bulky size of the interferometers. Most of other metrology tools also suffer from large size and hence lack parallel operation capability.

2.3 Miniaturized Scanning Grating Interferometer (μSGI) with tunable grating

To overcome the shortcomings in the current metrology systems, miniaturization of the metrology systems is advantageous. Earlier in this project, Kim et al introduced micromachined diffraction gratings to miniaturize the laser interferometer. Micromachined diffraction gratings have been successfully used for interference based miniaturized display systems like Grating Light Valves™, interference based miniaturized displacement measurement systems used for Atomic Force Microscopes (AFM), optical modulators etc [55-57]. Kim et al successfully used this micromachined scanning gratings interferometer (μSGI) to measure both the transient and steady state vibrations of MEMS devices with sub nm resolution [54].

As mentioned earlier, in most of the conventional non-contact metrology techniques, the metrology tool and the sample are mounted on two different stages which make them prone to ambient and acoustic vibrations. Several methods have been used to detect and reduce the error introduced by environmental vibrations and drifts. These include detecting the harmonic distortions by modulating the length of optical fiber, modulating the Fabry-Perot cavity [58], modulating the reference position [59]. Other phase-locking methods like optical intensity feedback [60] and optical feedback [61] actively tune the frequency of the laser to achieve highest sensitivity and vibration reduction. Fringe motion has also been used for phase-locking [62]. Fourier analysis techniques to separate low frequency error has also been demonstrated [63].

Graebner et al demonstrated that a scanning laser interferometer with active noise control can reduce the effect of low frequency vibrations successfully [53]. As the sensitivity of the optical interferometer depends on the optical path difference, this technique enabled phase-locking to the point of highest sensitivity while recording measurements. This has the dual benefits of increasing the resolution while reducing the impact of vibrations on the system. A resolution of 0.3pm/√Hz and a bandwidth of 6GHz was demonstrated using this technique [12]. Optical scanning interferometers are also shown to be used for measuring in-plane motion [64, 65].

Kim et al implemented the phase-locking to highest sensitivity point and vibration reduction by mounting the µSGI on a piezo-electric transducer (PZT). However bulky PZTs can not be used to individually tune multiple µSGIs. To solve that problem, a tunable (i.e. movable) grating was micromachined on aluminum membrane fabricated on a quartz wafer [66]. The tunable membranes showed sufficient displacement range to reach the closest highest sensitivity position on the optical curve from any given point. The µSGI also demonstrated successful integration of tunable grating array, photo-

detector array and micro-lenses. However, it suffered from low yield, poor mechanical properties, poor optical performance and high squeezed film damping. Active control using the tunable gratings could not be successfully implemented on this device. The active noise reduction used by Kim et al was based on analog lock-in amplifier based harmonic distortion method [53, 54]. However, the analog implementation of the active noise reduction scheme is also not suitable for simultaneous operation of multiple μSGIs.

The next section explains the concept of metrology with diffraction grating interferometer. It also introduces the active path stabilization for noise reduction and sensitivity optimization.

2.3.1 Diffraction based displacement detection using grating interferometer

The μSGI is a diffraction-based optical displacement measuring system. Figure 8 shows a schematic of the μSGI with photo-detector integration. The main feature of the grating interferometer is a phase sensitive optical diffraction grating, wherein the diffraction pattern is determined by the distance between a reflective grating and a reflecting surface. The μSGIs can also operate in parallel with individual actuation and many sample points spread over a large area can be tested simultaneously.

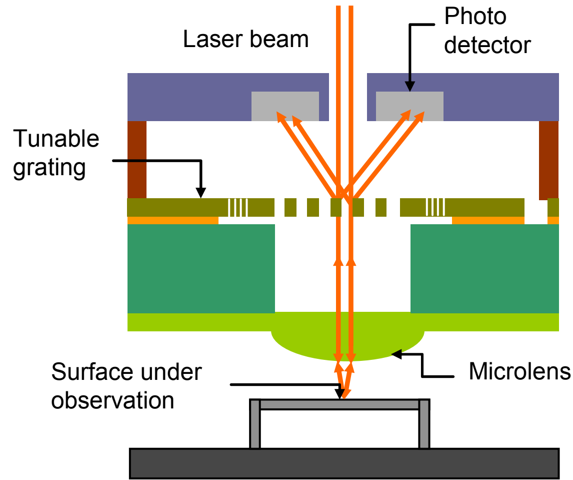

Figure 8: Schematic of a single µSGI - the tunable grating micro-interferometer with integrated photo-diodes and microlens

The grating is illuminated by a laser beam as shown in Figure 8. Part of the incident beam is diffracted back (shown by orange rays) by the grating fingers and the remaining light passes through the spacing between the fingers. This beam reflects back from the surface under observation to the grating fingers. A microlens can also be used to focus the beam to achieve a good lateral resolution, if required [54, 66]. The reflected light (shown by red rays) passing through the grating fingers interferes with the light reflected from the fingers generating diffraction orders. A photo-detector (PD) can be used to measure the intensity of the 1st order. The intensity of the first order is a function of the phase difference between the two interfering light beams and can be used to measure the relative displacement between the grating and the sample. The intensity of -1st order can also be detected by another photo-detector to obtain higher signal to noise ratio.

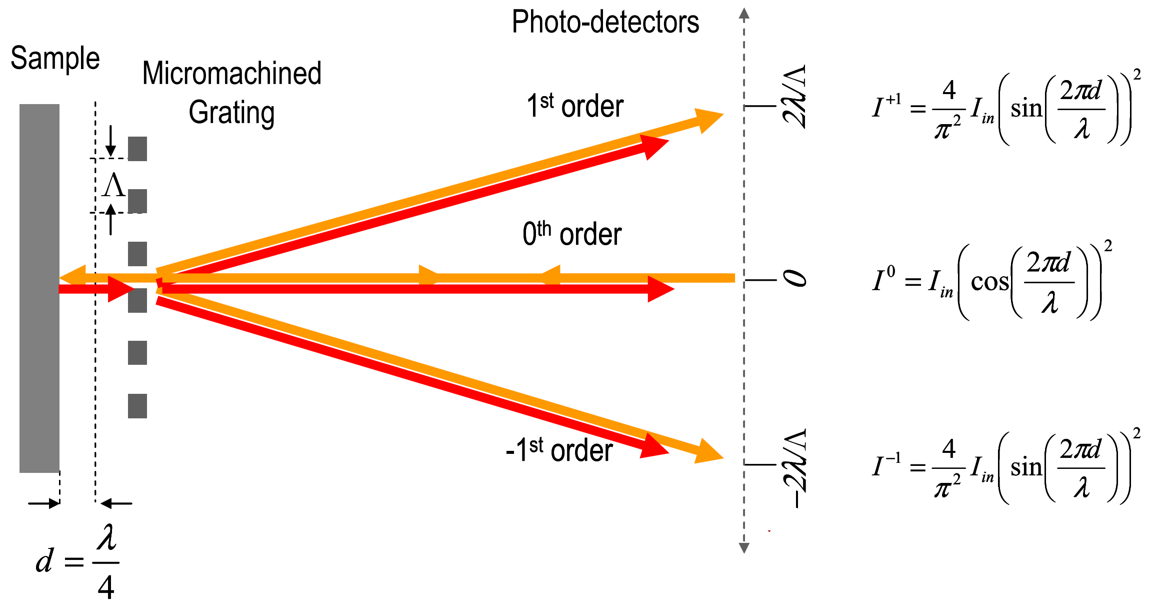

Figure 9 – Concept of diffraction grating interferometer

Figure 10 depicts the intensity of a diffraction order as a function of the distance between the grating and the surface under observation. In this figure, it can be seen that the sensitivity or the slope of the curve changes with the distance between the grating and the surface. At the maximum sensitivity point, which is the inflection point, this curve is linear and is ideal for the measurements of vibrations of very small magnitudes. Many factors like initial positioning, low frequency vibration, uneven profile of the sample surface and acoustic noise may shift the distance between grating and sample. This can cause a significant change in the sensitivity of the measurements as well as introduce errors in the readings. Hence, an active control needs to be implemented to negate these effects.

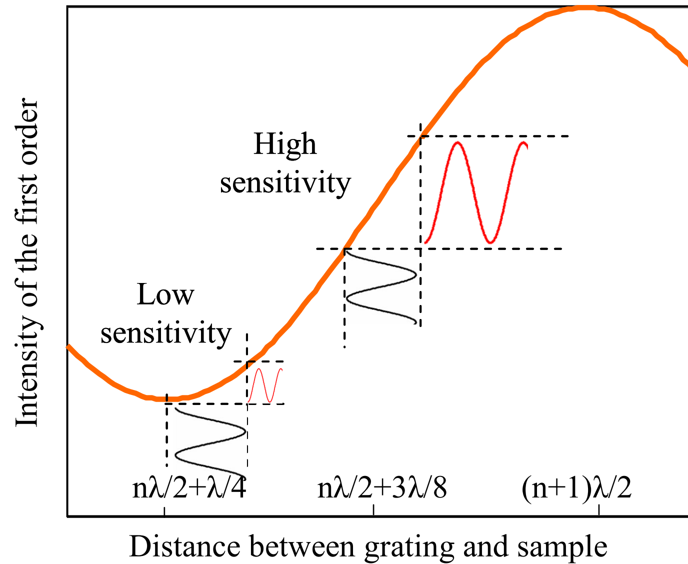

Figure 10 - Schematic of the optical intensity curve

The noise at different locations on the sample can differ. The stage on which the samples are mounted may have a tilt. (See Figure 11) The different sample points under observation may be fabricated at different heights by design. Hence for array operation, disturbances need to be reduced at each of the points under observation simultaneously. The tunable grating of μSGI is designed to reduce this effect by implementing an active control. Each μSGI has a tunable membrane on which the gratings are micromachined that can be displaced with electrostatic actuation as described above. This independent actuation capability enables an array of μSGIs to be used simultaneously with high sensitivity and reduced noise.

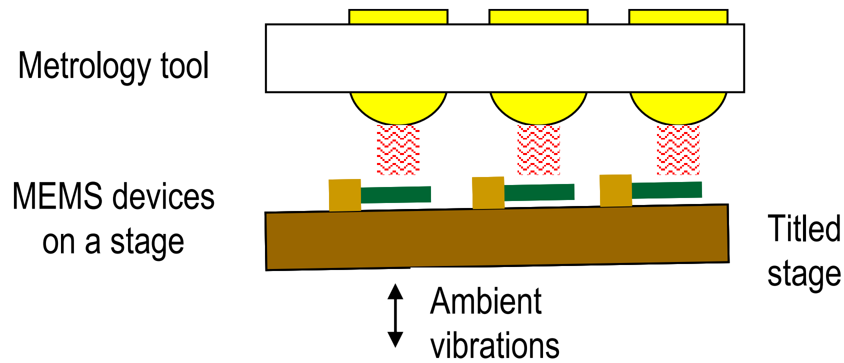

Figure 11 – Need for parallel active path stabilization

As seen in the problem statement, the measurement range is critical for many metrological applications. Interferometric readout, as seen in Figure 10, repeats itself with half-wavelength pitch. So typically it is required to use a quadrature method to measure displacements longer than half-wavelength. The tunable grating makes use of the active control algorithm to track the surface motion beyond the limits of half-wavelength.

Thus the Micromachined Scanning Grating Interferometer with tunable grating and recurrent calibration based method enables parallel operation of miniaturized interferometers with high resolution, large bandwidth and long range. Following chapters explain different aspects of μSGI in detail.

CHAPTER 3

TUNABLE GRATINGS

Tunable gratings of the μSGI enable miniaturized method for interferometry. It can be tuned by electrostatic actuation which enables active path stabilization for low noise operation. This chapter explains the design, fabrication and characterization of tunable gratings in detail.

3.1 Design of tunable gratings

3.1.1 Design requirements

For the μSGI to operate properly, a few critical design requirements are identified. The maximum sensitivity position on the optical curve repeats every half-wavelength of displacement as shown in Figure 10. Hence, the range of displacement of the tunable grating needs to be greater than half the wavelength of the laser used (He-Ne laser), i.e. greater than 316nm, to achieve a maximum sensitivity position from any position on the optical curve. The ambient mechanical vibration noise mostly occurs below 300Hz. Hence, the dynamic range or bandwidth of operation should be sufficient to reduce noise below approximately 1 kHz. The bandwidth is determined by the first resonance frequency, which needs to be more than 20 kHz and the squeezed film damping should be negligible in the bandwidth of interest. Actuation voltage range should be easily achievable i.e. below 30-40V. The grating needs to be flat, even under actuation for good optical performance. The design should also be easy to fabricate so as to have good yield. The control algorithm needs to run in parallel for multiple devices and cancel noise in the required bandwidth.

3.1.2 Quartz based tunable gratings

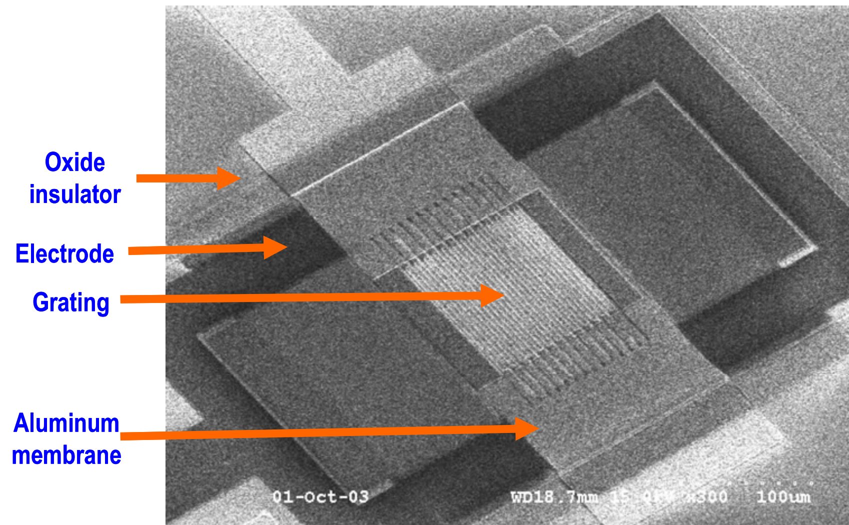

Figure 12 – Quartz based tunable grating made from Aluminum

Kim et al designed and fabricated the first micromachined tunable gratings [15, 66]. These tunable gratings are built on quartz substrate. A fabricated tunable grating is shown in Figure 12 and the schematic of the design is shown in Figure 13. This grating contains an Aluminum bottom electrode layer on which an insulating Silicon dioxide (oxide) layer. Another layer of Aluminum is deposited on a sacrificial photo-resist layer. The tunable grating and the membrane are etched on this layer. The grating portion of the top aluminum membrane is kept thicker than the rest of the membrane. The grating membrane serves as the top electrode and it can be pulled down by electrostatic actuation. The thickness of the gratings helps keeping the grating flat when the grating membrane is actuated.

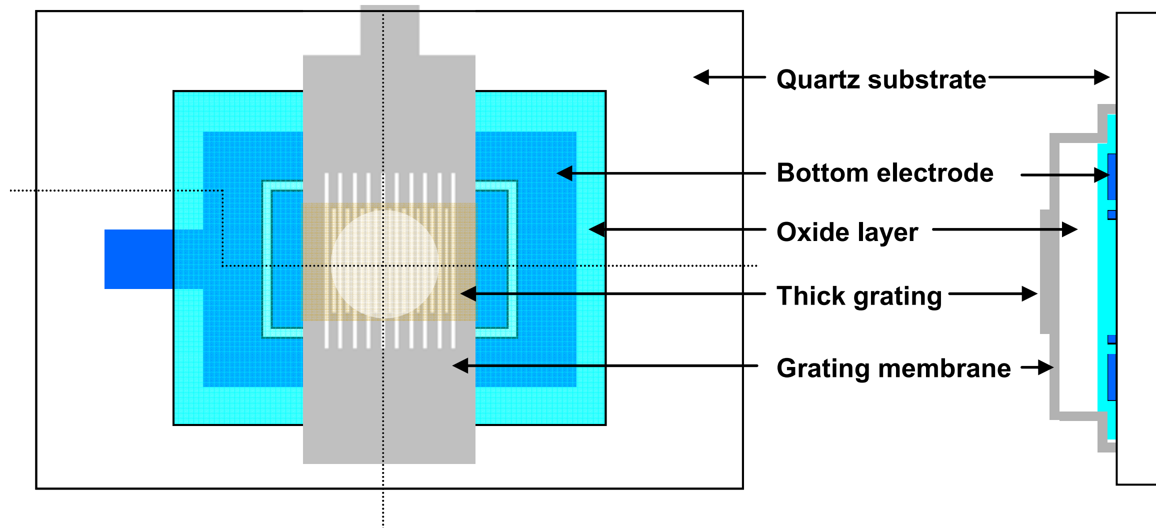

Figure 13 – Schematic of the quartz based tunable grating

This quartz based tunable grating achieved sufficient range of motion (0.6 μm) and 20 kHz bandwidth. Kim et al successfully demonstrated integration of photo-detector chip and micro-lenses. External He-Ne laser and lenses were used to illuminate the grating. Figure 14 shows an integrated device array wirebonded to a printed circuit board (PCB).

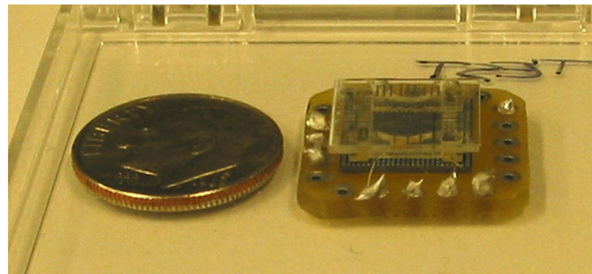

Figure 14 – Miniaturized assembly of quartz based tunable grating

This μSGI suffered from residual stresses on the Aluminum membrane. The membrane sagged down due to the stresses when fabricated. The fabrication process was complex and it involved 6 masks. The process took long to fabricate and resulted in a low yield. The bandwidth of the membrane was limited by squeezed film damping. This damping is caused by the air film trapped between the membrane and the substrate.

Aluminum was found unsuitable as a structural material. The active path stabilization was implemented using external piezoelectric transducer (PZT). The sample was mounted on a PZT stage and path stabilization was achieved by actuating the PZT. PZT being bulky actuators, array operation of active path stabilization could not be achieved. The harmonic distortion error was obtained using analog phase locking circuitry.

3.1.3 Novel SOI based tunable gratings

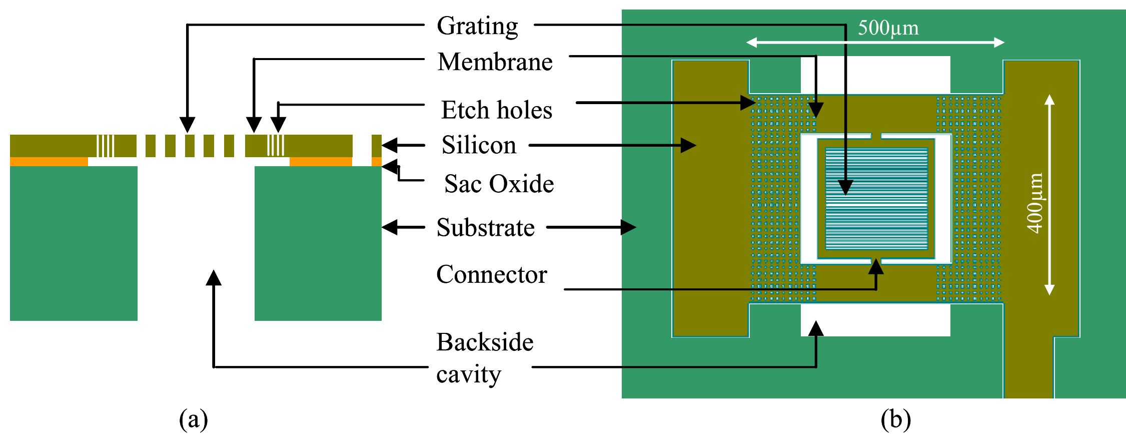

Figure 15 – Schematic diagram of the tunable membrane fabricated on SOI wafer (a) Cross sectional side view (b) Top view

To overcome the problems faced by quartz based µSGI, the µSGI was redesigned. To make the membrane structurally strong and less prone to residual stresses Silicon on Insulator (SOI) wafers are chosen. An SOI wafer has been advantageous for MEMS with membrane structures because of the excellent mechanical properties of the silicon membrane and the embedded sacrificial and insulating buried oxide [67]. The schematic of the SOI based tunable grating is shown in Figure 15. The SOI wafer used for fabrication has a 2.7µm thick p-doped silicon device layer, a 1µm thick sacrificial silicon dioxide layer and a 500µm thick p-doped silicon substrate. The tunable grating is fabricated on the silicon membrane layer (or the device layer) and part of the grating membrane with etch holes is released by etching the sacrificial oxide underneath. The

backside cavity allows the laser beam to pass through the grating. Backside cavity reduces the squeezed film damping effect and also significantly reduces stiction during release and actuation. The cavity also provides extra range of motion for the grating. The silicon membrane is p-doped and acts as one of the electrodes. The substrate is also p-doped and serves as the other electrode. These electrodes provide electrostatic actuation for the tunable grating. The design does not require any special mask for the electrical connections.

As shown in Figure 15, the tunable membrane is a 500μm x 400μm rectangle holding a 200μm square grating at the center. Residual stresses and the electrostatic attraction force from the substrate electrode make the membrane bow. However the grating on the membrane needs to be flat for good optical performance. To solve this problem the tunable membranes have a layout to reduce the effect of the residual stresses and bending of in the membrane on the grating. The grating is connected to the membrane by small connectors or hinges, as shown in the figure, which do not transfer the bending moment to the grating. The intention is to get a flat grating throughout the required range of membrane deflection. However, the connectors also act as torsion springs which gives rise to an unwanted resonance mode in which the grating hinges on the connectors. The width of the connector determines the stiffness of the torsion springs which in turn determines the resonance frequency of that mode. A wide connector keeps the resonance frequency of this unwanted mode greater than the first resonance frequency of the membrane which ensures less impact of this unwanted mode on the operation of the tunable grating. However, a wide connector is a stiffer torsion spring and transfers bending moment from the membrane to the grating. To deal with this trade-off a Finite Element (FE) analysis is used and connector-widths ranging from 10μm to 40μm are chosen.

Gratings of periods ranging from 4μm to 6μm are designed, which give a sufficient (6° to 9°) angular separation between the diffraction orders for a He-Ne laser. The laser beam passing through the microlens undergoes ~30% optical loss and depending on the reflectivity of the sample some intensity can also be lost in the reflection [54, 66]. For a complete optical interference, i.e. high modulation, the intensities of the two interfering beams should be the same. To compensate the losses, the fingers are designed to cover only 25% to 40% of the grating area. Etch holes of 4μm square at a period of 12μm are used as shown in the figure, to facilitate the release of the membrane at selected regions. The tunable gratings are laid on 12mm x 12mm chips in the form of 4x2 and 5x2 arrays.

3.1.4 FE modeling tool and simulations of μSGI tunable grating

A finite element model of the grating membrane was built using ANSYS multiphysics. This model is used for simulating the mechanical deflections under electrostatic loads, squeezed film damping and the dynamic characteristics of the grating membranes. The design parameters were optimized using the finite element model.

Figure 16 shows the top view of the model of the μSGI tunable grating. The region shown by different colors indicates the electrode region (where there is substrate underneath the membrane) and the non-electrode regions (which hang over the backside cavity). The ends of the membrane are clamped at the two ends. The grating is simplified to a 5 finger grating keeping the mass constant. This reduces the computational complexity of the model. The grating remains flat when it operates in the lower frequencies; hence the simplification is not expected to cause a significant effect on the grating dynamics when it operates at lower frequencies.

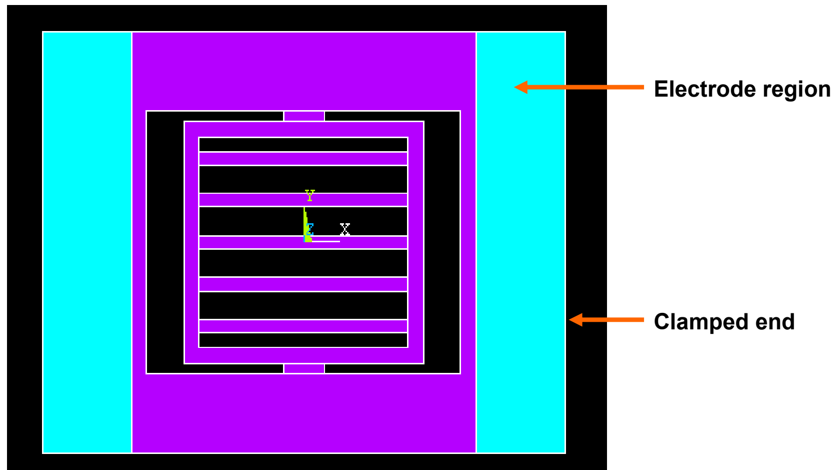

Figure 16 – ANSYS multiphysics model of the tunable grating

Three types of elements are used for this analysis. Mesh200 element is a meshing facet, plane42 is a 2D structural solid and solid45 is 3D structural solid. The FE is done in μMKS units with the following material properties for Si – density = 2300E-18 units, Young's modulus = 169E3 units and Poisson's ratio = 0.2. The details of the code are given in the appendix 7.1.

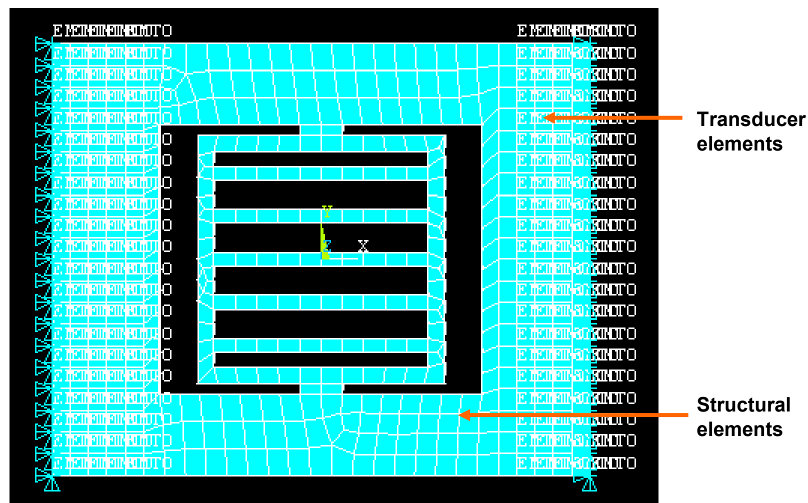

Figure 17 – Meshed model showing transducer elements and structural elements

This code is an iterative simulation tool for electrostatic, static, dynamic FE analysis of electro-mechanical components. Multiple loops can be specified for varying dimensions

and the deflection or frequency output can be stored in a file named “results”. A sample output is also given in the appendix 7.1.

One example of static characterization is shown in Figure 18, which shows the electrostatically actuated tunable grating membrane at 25V bias voltage. It can be seen that the membrane bends and the grating remains flat with a displacement of 0.14 μm.

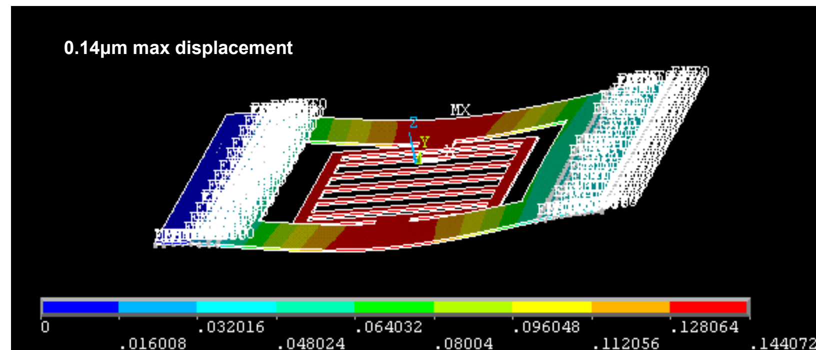

Figure 18 – Electrostatically actuated membrane with 25V actuation voltage

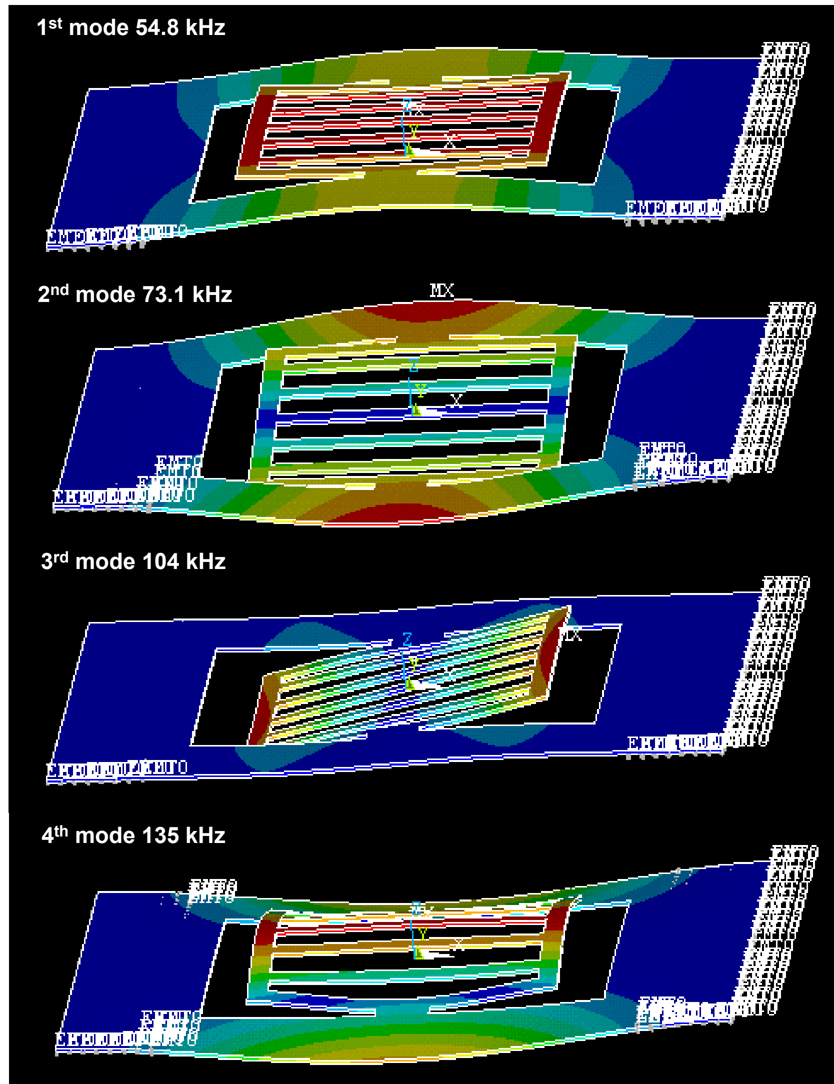

Figure 19 - First four modes of resonance obtained by FE analysis

The same FE model is also used for harmonic analyses of the tunable gratings. Fluid 136 elements are used to simulate the squeezed film damping. The compressive residual stress of 12MPa also affects the harmonic response of the membrane. This stress was introduced in the length direction by displacing one of the fixed walls by the appropriate distance. The mode shape results for the grating resonating at fist four modes are shown in Figure 19. It can be seen that the first resonance occurs at around 54.8 kHz and the mode shape shows a flat vertical displacement of the grating. This determines the bandwidth of the actuation for active control of the grating. The second

mode of resonance occurs at 73.1 kHz where the grating does see-saw motion in the width direction and is not useful. The third mode is the see-saw motion of the grating about the connectors. The design under consideration has 40 μm wide connectors and the resonance mode occurs at around 104 kHz. The fourth resonance mode is as shown in the Figure 19 and occurs at 135 kHz.

The iterative capability of the simulation tool is very useful in optimizing the parameters of the structures. An example result from the iterative too is shown in Figure 20. The iterative tool enables continuous run of the code without any active user input. It can be seen that the displacement reduces as the thickness of the membrane increases. Also, the first resonance frequency of the tunable grating increases with the thickness as expected. There is a trade-off between these two parameters. For the tunable grating a bandwidth of 50 kHz is chosen (~2.5 μm thickness) where the required range of motion at 25V is about 0.2 μm, however a voltage range of 10V to 40V is chosen to achieve the required range of motion. This is explained in the static characterization of the tunable grating.

The simulated static characterization of the tunable grating is shown in Figure 21. It can be seen that the displacement of the grating increases with increase in voltage. The rate of change of displacement also increases with the bias voltage, as expected. This is due to the electrostatic voltage which applies force has squared proportionality to the bias voltage. It collapses at around 55-60V.

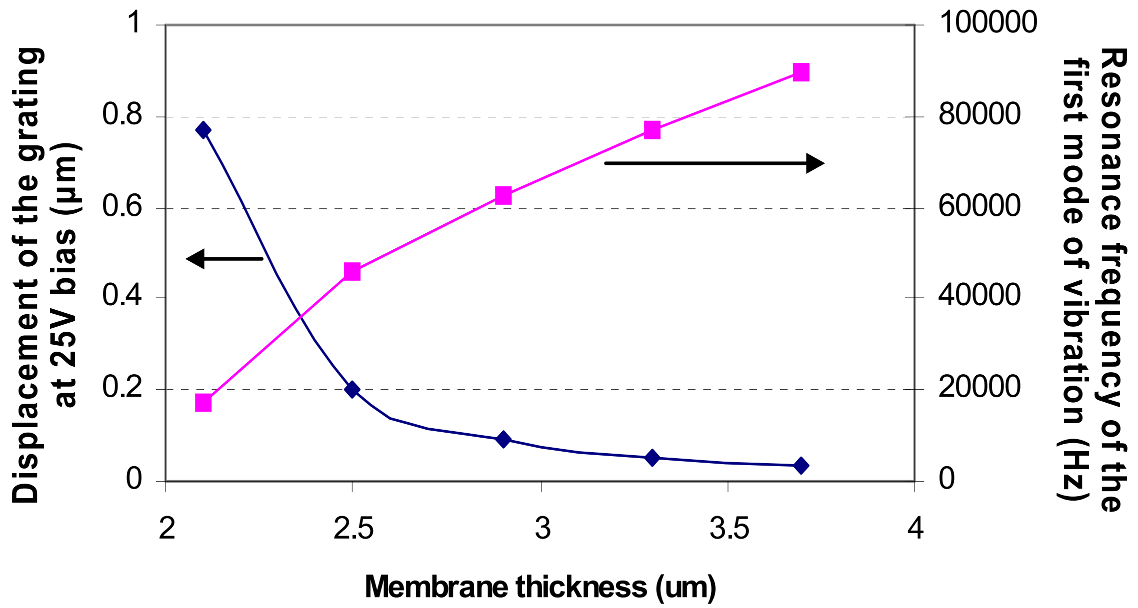

Figure 20 – Displacement of the grating at 25V vs. membrane thickness

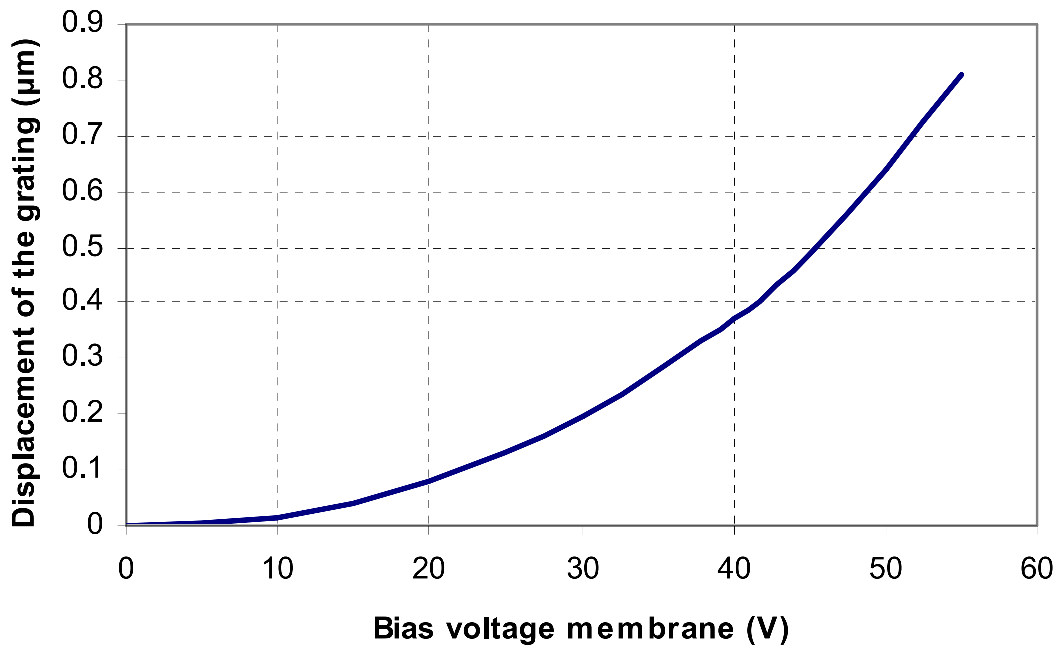

Figure 21 – Static response of the grating to the DC bias sweep

The frequency response of the tunable grating is also obtained from the same model. It is shown in Figure 22. It shows first 4 modes of the resonance frequencies. It can be seen that the response of the tunable grating is flat in 30 kHz bandwidth. The third mode

of resonance frequency has high amplitude in the frequency response and it can be problematic in the operation of the tunable grating if it is actuated. It is important not to measure the vibration amplitudes at the center of the grating. Mode 2 and mode 3 shows a zero amplitude node at the center of the grating; hence the peaks could be missed in the frequency response. The displacements are obtained at a point at a corner of the grating area. For the first 3 mode shapes, this point has the maximum displacement over the grating area. For the fourth mode also, this does not represent a zero amplitude node.

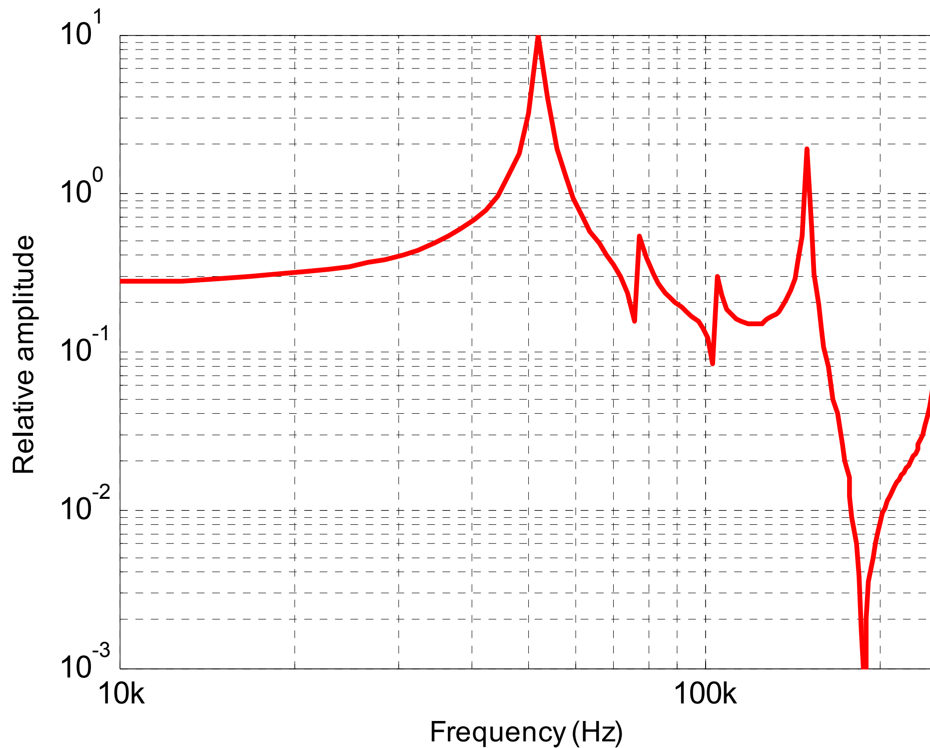

Figure 22 – Simulated frequency response of the tunable grating showing first 4 resonance modes

The displacement of this point on the grating is not the correct representation of the amplitude of the optical output from the miniaturized interferometer. This is due to the fact that the laser beam is aligned with the center of the grating and it is averaged over

the cross-sectional area of the beam. The amplitude of the optical output also gets affected if the grating tilts or deforms as shown in mode 2, 3 and 4.

3.2 Micro-fabrication of SOI based tunable gratings

The fabrication of tunable gratings using Silicon on Insulator wafers uses well standardized processes. The tunable gratings are designed to be fabricated in a 2 mask process. Two methods of fabricating the tunable gratings were developed. One method used Potassium Hydroxide (KOH) based solution for etching the backside cavity. The other method uses Induction coupled plasma (ICP) to etch the backside cavity. The ICP method was used to fabricate the devices. It is explained in detail in this section. The KOH method is briefly described at the end of the ICP method.

The design of first or the grating mask defines the tunable grating, etch holes, membrane and electrode layout. The second or the backside etch mask defines the size of the backside cavities. The details of the mask layout are as follows

3.2.1 Mask 1 layout design

A mask consists of 32 tunable grating chips as shown in Figure 23. The top row containing 4 chips contain large areas of gratings. These gratings have the same period as of the tunable gratings and are used for destructive testing to see the cross section of the grating under Scanning Electron Microscope. The parallel lines at the top of the mask are used for alignment with the wafer flats. This is important in the case of KOH etch as it is anisotropic. The 32 chips are divided in to 16 identical pairs of chips in Figure 23. The chips have 4x2 arrays or 5x2 arrays of tunable gratings as shown in Figure 24.

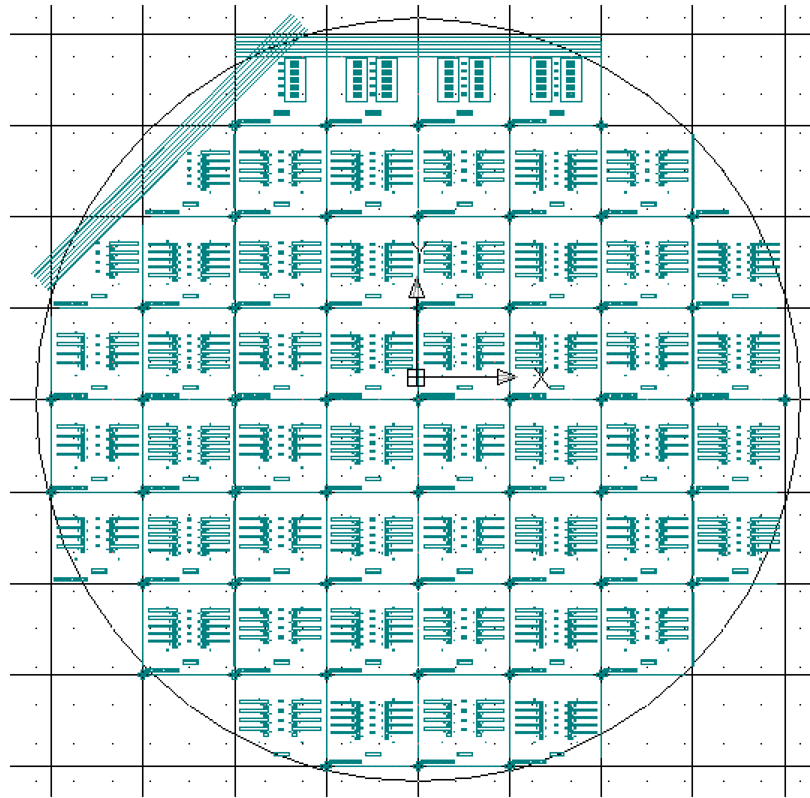

Figure 23 – mask 1 wafer layout

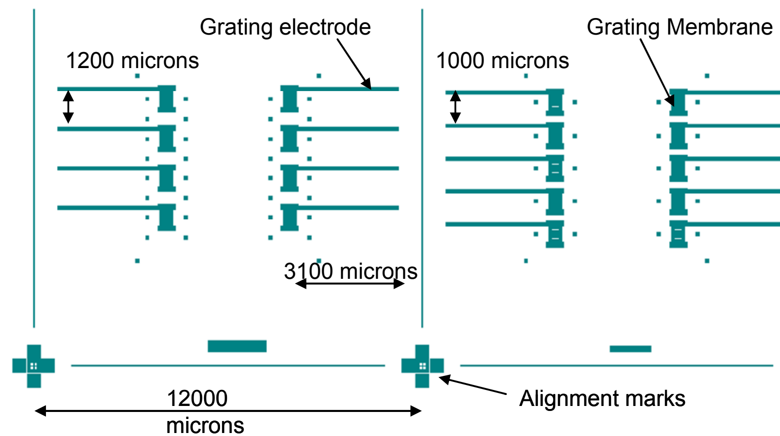

Figure 24 – Mask 1 - chip layout

Each chip is 12 mm x 12 mm in area and has guidelines for dicing at the borders of the chips. The chips have alignment marks at the 4 corners and also on both sides of each tunable grating. The other relevant dimensions are shown in Figure 24.

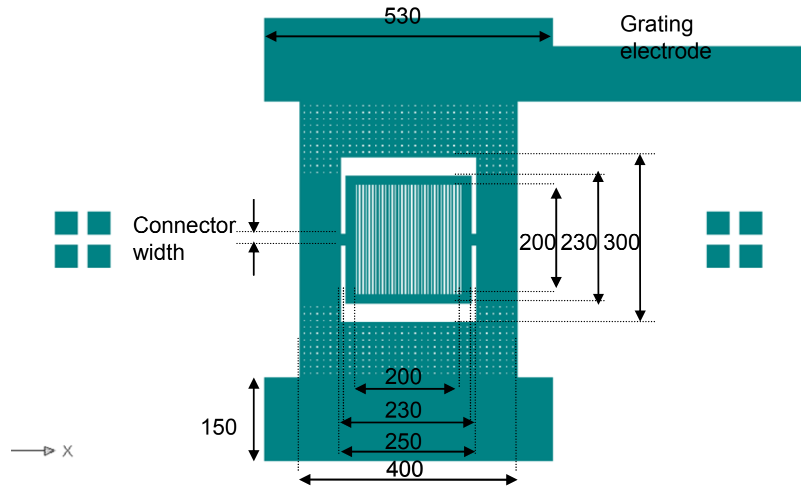

Figure 25 – Mask 1 - Device layout

Figure 25 shows the layout of a tunable grating membrane. All dimensions are specified in Figure 25 except the connector width which is varied over the tunable gratings in a pair of chips.

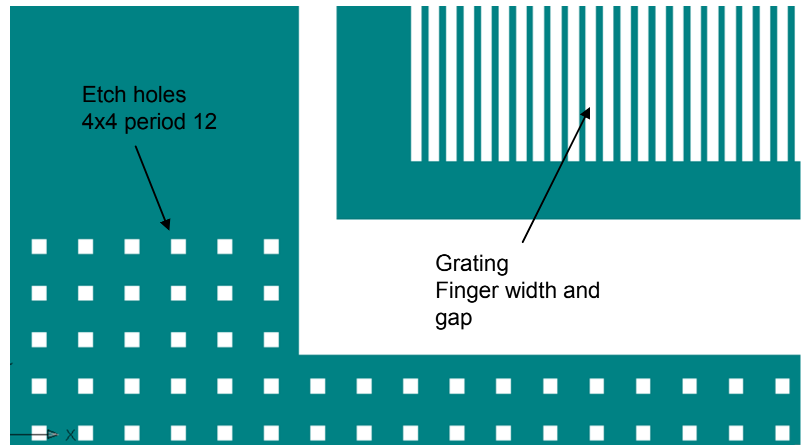

Figure 26 – Etch holes and grating fingers

Figure 26 shows a close-up of the grating and the etch holes. The etch holes are 4μm x 4μm in size and placed at a period of 12 μm. The spacing between the etch holes determines the etch time for the buried oxide wet etch process to release the

membranes. The gratings are designed to have different periods and spacing and the details are as follows.

3.2.1.1 *Variation in a chip*

Connector width and the grating finger width and gap are varied as shown below. The grating finger width is varied from 1 µm to 2 µm and the grating period is varied from 4 µm to 6 µm. The connector width is varied from 10 µm to 40 µm. A set of tunable gratings are designed not to have a stress-free gratings where the gratings are directly etched on a continuous membrane. These are called the type 1 gratings and the stress free gratings are called type 2 gratings and are shown in Figure 27.

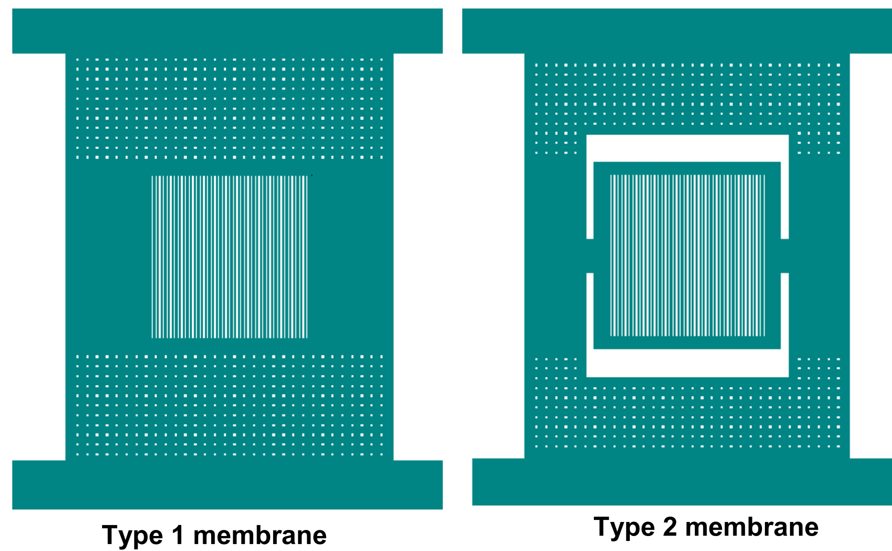

Figure 27 – Type 1 and type 2 membrane layouts

Table 3 – Dimensional variation in 5x2 arrays:

First column devices		Second column devices	
finger width, period	Connector width	Gratings spec	Connector width
1 µm, 4 µm	40 µm	1 µm, 4 µm	type 1
1.5 µm, 4.5 µm	10 µm	1.5 µm, 4.5 µm	20 µm
2 µm, 5 µm	40 µm	2 µm, 5 µm	type 1
1.5 µm, 5.5 µm	10 µm	1.5 µm, 5.5 µm	20 µm
2 µm, 6 µm	20 µm	2 µm, 6 µm	20 µm

Table 4 – Dimensional variation in 4x2 arrays

First column devices		Second column devices	
finger width, period	**Connector width**	**finger width, period**	**Connector width**
2 µm, 6 µm	10 µm	2 µm, 6 µm	20 µm
1.5 µm, 4.5 µm	40 µm	1.5 µm, 4.5 µm	type 1
2 µm, 5 µm	10 µm	2 µm, 5 µm	20 µm
1.5 µm, 5.5 µm	40 µm	1.5 µm, 5.5 µm	type 1

3.2.2 Mask 2 layout design

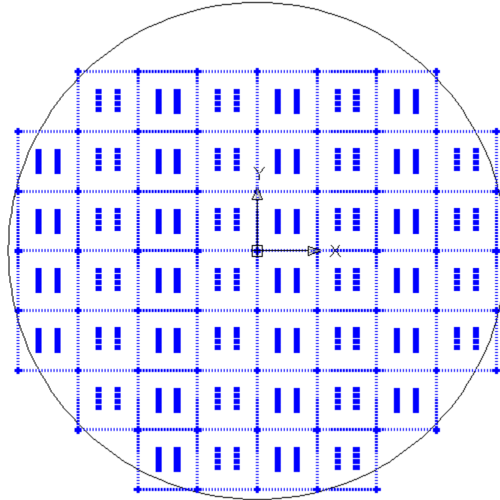

Figure 28 – Mask 2 overall layout

Mask 2 defined the geometries of the backside cavities. Figure 28 shows the overall layout of the cavities. It follows the same guidelines of the mask 1. The top row of chips does not have backside cavities as those do not contain any tunable gratins. Figure 29 shows the chip layout for mask 2 for a 5x2 array and a 4x2 array. Note that this is a dark field mask – i.e. the regions shown in blue are transparent and the white regions are opaque. The chip boundaries are marked with lines made of rectangles orthogonal to the boundaries. This enables view of the chip boundaries from the Mask 1 for easy alignment.

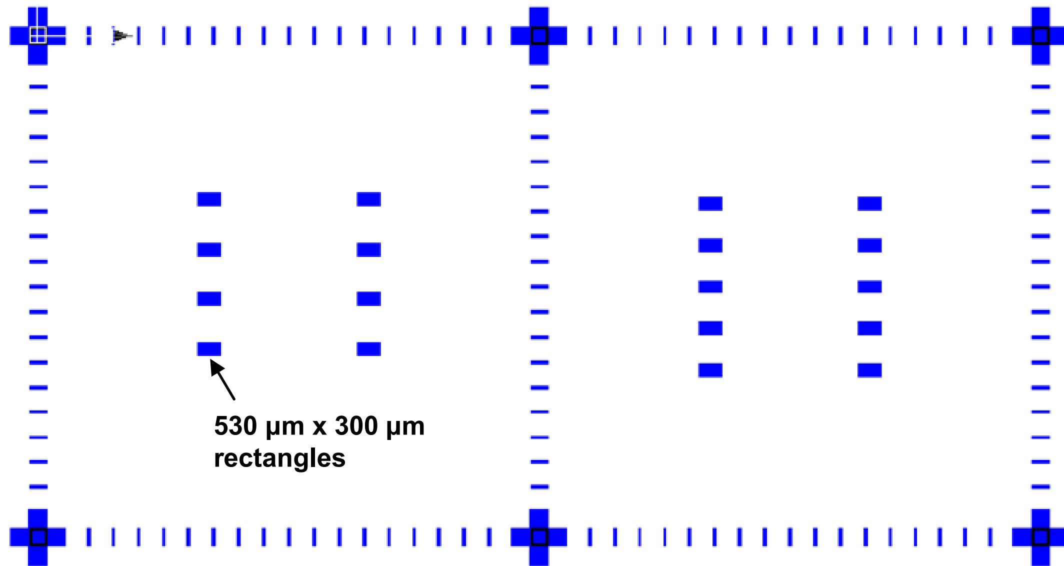

Figure 29 – Chip layout for Mask 2

For KOH processing the holes need to be larger in size as the etching occurs along the (1, 1, 1) plane of the single crystal silicon. This (1, 1, 1) plane makes an angle of 54.74° to the plane of the wafer. Depending on the thickness of the wafer the size of the backside cavity can be calculated. One problem with the KOH etching method arises due to the uncertainly or inaccuracy in the wafer thickness. This results in a smaller or larger cavity under the tunable grating membrane. The size of the cavity determines the size of the bottom electrodes which provide the electrostatic forces and also determines the squeezed film damping. ICP etch is enables etching the wafers with almost 90° etch angle which reduces the dependence of the cavity size on the thickness of the wafer. Hence, ICP method is preferred when it is feasible. In comparison with the KOH etch, ICP etch is faster, convenient and the other hand it also involves high temperature processing.

3.2.2.1 Alignment marks

The alignment marks have 3 levels of alignment. Figure 30 shows the detailed view of the alignment marks. The size of the alignment marks is about 1.3 mm x 1.3 mm with 5

big squares for coarse alignment. The central square has another set of 4 squares each for both masks. The outer edges of the squares can be used for finer alignment, and the inner edges of the squares are very finely placed to give a smallest feature of 4 μm.

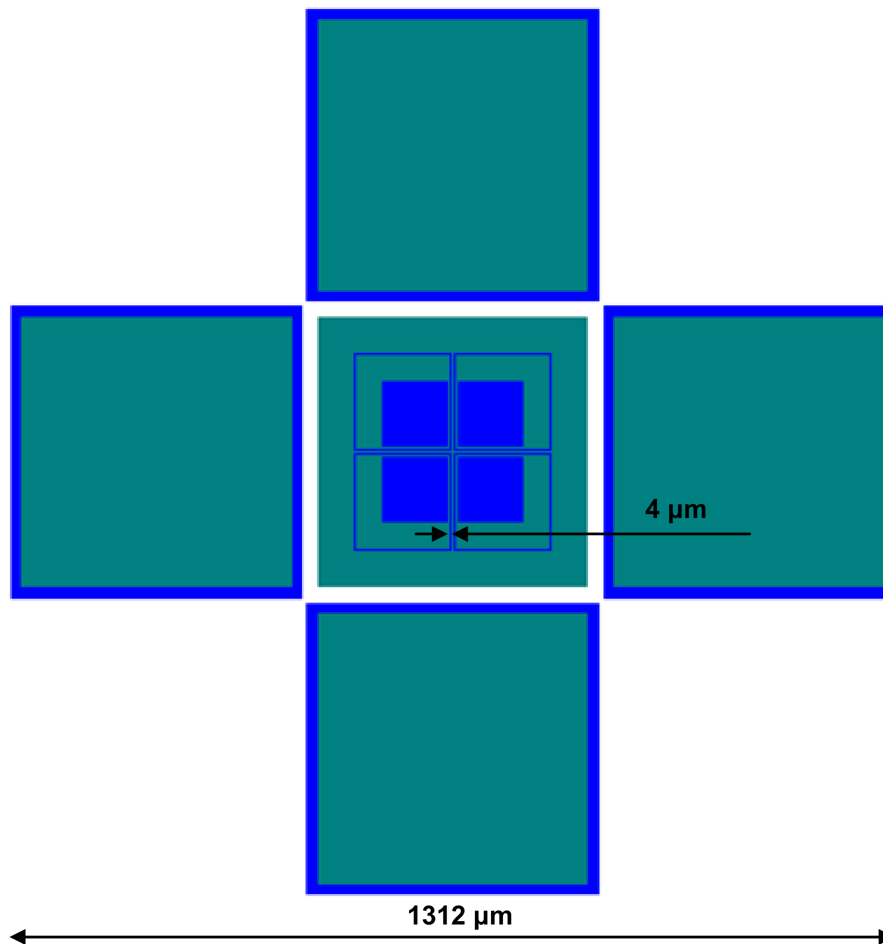

Figure 30 – Alignment mark from both masks (mask 1 - green and mask 2 - blue)

3.2.3 Process development

The developed process sequence for the SOI based tunable membranes is shown in Figure 35. The fabrication is a simple two mask process on SOI wafers. The top mask patterns the device layer which consists of the movable membrane with grating; etch holes and openings for the substrate electrode. The second mask is used to pattern the

oxide for backside cavity. This oxide is the mask for backside Induction Coupled Plasma (ICP) etching. The wafers are then diced in to chips.

The process is explained in the following section. Figure 31 shows the schematic of the cross section of the tunable grating.

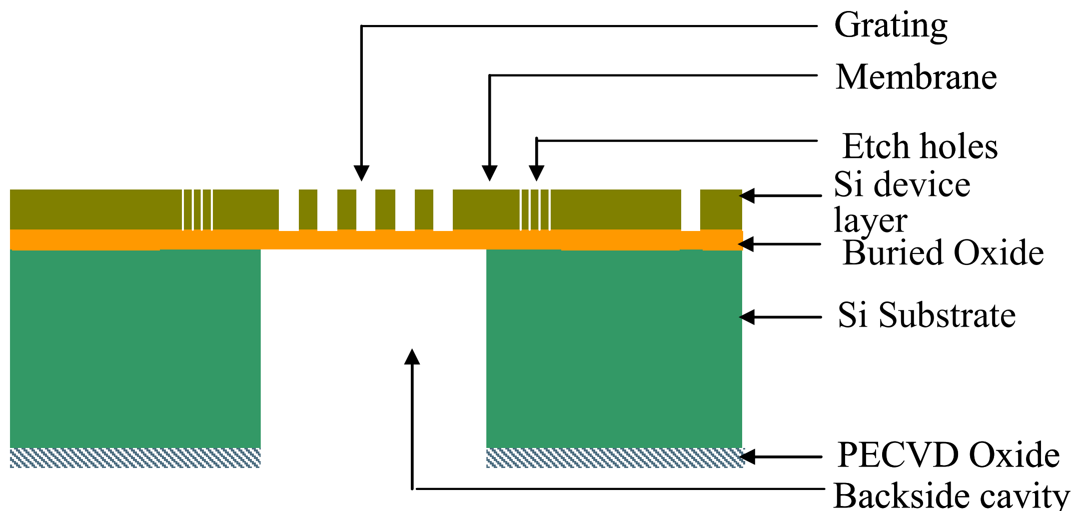

Figure 31 – Schematic cross section of the tunable grating membrane

Silicon on insulator wafers with 500 μm substrate, 1 μm oxide layer and 2.5 μm silicon device layer is used. The thickness of the device layer varies from 2.4 μm to 2.8 μm. The process steps are described as follows

3.2.3.1 Front side processing with Mask 1

1. HMDS is spun for 4000/1000/60 and dried in air for a minute

2. Photo-resist 1813 is spun for 4000/1000/60

3. Soft bake 120°C for 1 min on hotplate

4. Expose for 7s channel 2 (20mW for 7s is 140mJ)

5. Develop in MF319 till the oxide surface looks uniform (takes variable time ~ 15 minutes shake the container once in a while).

6. DI water rinse until the oxide surface becomes hydrophobic ~ 2-3min

7. Etch in STS ICP – module 3 (for SOI wafers – recipe ok_mod3) 3.5min ~ 13 cycles. Actual etch rate is 0.4μm/cycle which corresponds to 5.2 μm however for a small run the etch rate is slower. STS ICP allows etching of vertical cavities with high aspect ratios. Trial Silicon wafers are etched to test the capability. The wafer is over-etched (~5 μm) and is broken at the grating. An SEM image of the cross section is shown in Figure 32. It can be seen that 1 μm wide finger structures can be successfully fabricated using the tool.

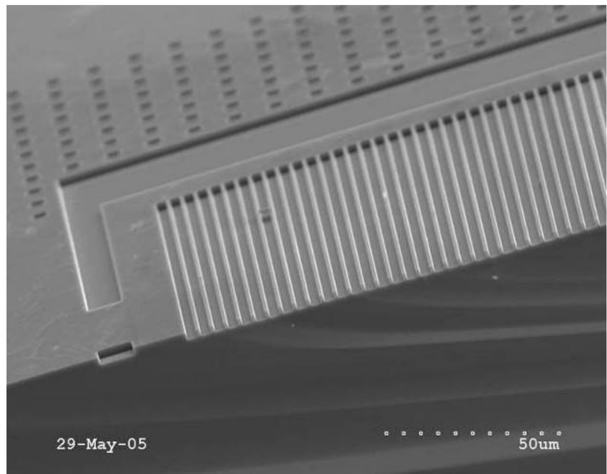

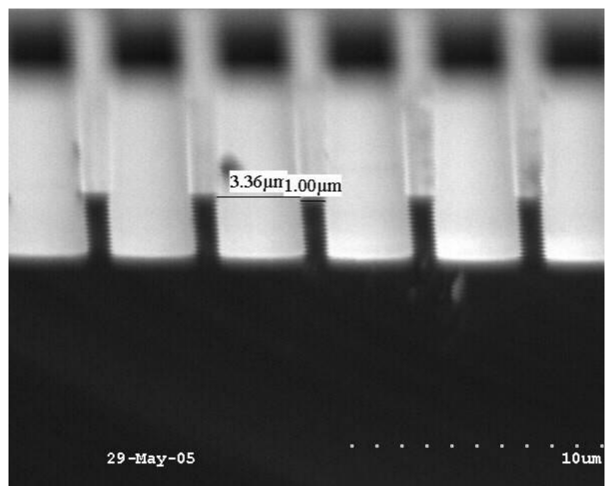

Figure 32 – STS ICP etch etching vertical trenches to make 1 μm wide fingers

8. PR and HMDS removal using acetone in ultrasonic bath for 20 min.

9. Observe the steps under profilometer – reads 2.4 to 2.8 μm

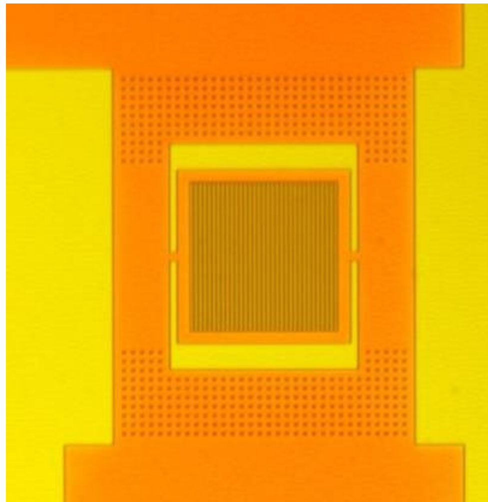

Figure 33 – a tunable grating after front side etching in STS ICP

3.2.3.2 Backside processing – Mask 2

1. Deposit 3 μm of oxide on backside in STS PECVD (recipe name: std_ox)

2. SPR220 spin 2000/250/40

3. Soft bake 110-115° C for 6:30min

4. Backside alignment using MA6 and Ch2 15s exposure i.e. 300mJ

5. Develop in MF319 until features look clean about 1-2min

6. Remove SPR220 from the borders so that it can be clamped in Plasma Therm ICP without sticking to the clamp

7. Hard bake at 120° C for 25min in convection oven

8. Etch in Plasma Therm ICP for 21min (do in 2 steps 15+6 to make sure that the etch rate matches)

9. Do not remove the SPR220, the wafer is ready for dicing

3.2.3.3 Dicing of wafer

1. Keep the devices facing up on the dicing tape. (It can be very sticky and sometimes can pull off deposited layers. SPR220 facing the dicing tape protects deposited layers).

2. Dice wafers into chips along the chip borders

3.2.3.4 Backside processing continued

1. A handling wafer is used to process the chips. A silicon wafer is coated with thick (>5 μm) PECVD silicon oxide layer. Chips mounted on this handling wafer using Cool Grease. The Cool Grease is applied using cotton swab only near the edges of the chips. It is important to make sure that the Cool Grease seals all the edges so that the gases in the ICP chamber do not enter to etch the front side.

2. STS ICP etch module1 400 cycles (0.9 μm/cycle) 360 μm etch (recipe name: ok_mod1E)

3. STS ICP etch module-3 (ok_mod3) for approximately 350 cycles (0.4 μm/cycle) 140 μm etch (total ~500 μm) Do in steps and measure the depth under Wyko profilometer. Do until the oxide window looks clean visually. Some deformation or cracking is visible due to the thermal stress mismatch between the sacrificial oxide and device silicon layer. (Figure 34)

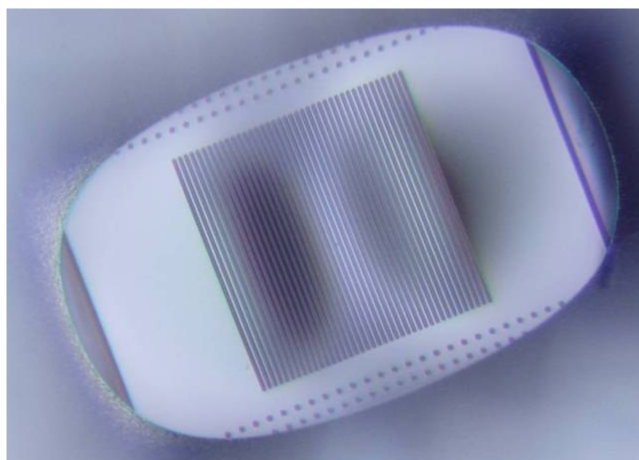

Figure 34 – Tunable grating observed from the backside after backside etching

4. Remove the chips from the mount wafer using tweezers and razor. Support one edge of a chip and flip it over slowly by sliding a razor under it. Make sure the features underneath do not touch any surface in the process.

5. Cool Grease needs is removed using a cotton swab and acetone. After backside etching the membranes are very easy to damage. Also, it is difficult to clean the Cool Grease from surfaces with features.

3.2.3.5 Releasing the membranes

1. To release the membranes 49% HF is used. The chips are dipped in 49% HF for ~ 12min.

2. The chips are dipped in DI water container and slowly water in the container is changed

3. Chips are dipped in acetone for 1 hour (change acetone 2 times at 5 min and 10min).

4. Chips dried in Super Critical Dryer.

5. The chips are observed under Profilometer (Wyko) to check if the membranes are properly released. The membranes show a small (~50nm) upward buckling deflection which shows the released portion of the membrane.

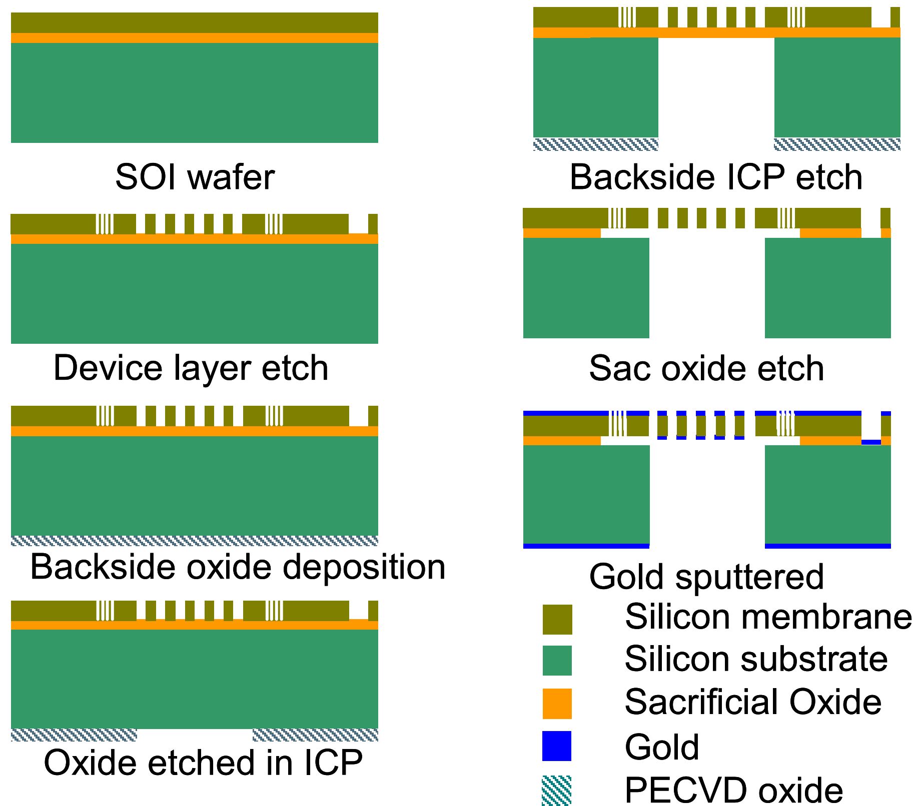

Figure 35: Fabrication process sequence for the tunable grating interferometer

A thin layer of Gold (~100nm) may be evaporated or sputtered on top surface to improve electrical bonding and reflectivity; however it is optional and is not done for the μSGIs studied in this paper. The number of process steps and masks are significantly less as compared to earlier designs [66].

3.2.4 Fabrication results

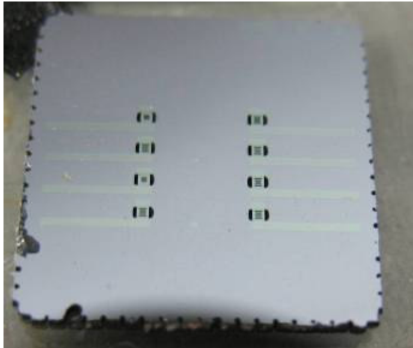

Figure 36 – A fabricated tunable grating chip

Figure 36 shows a fabricated tunable grating chip with 2X4 array of tunable gratings. The edges of the fabricated chips are damaged by backside ICP etching through the holes designed for ease alignment and dicing over it. The fabricated chips are observed under microscope and the pictures of type 1 and type 2 membranes under microscope are shown in Figure 37 and Figure 38. The membrane layout, the substrate and the backside cavity can be clearly seen in the pictures.

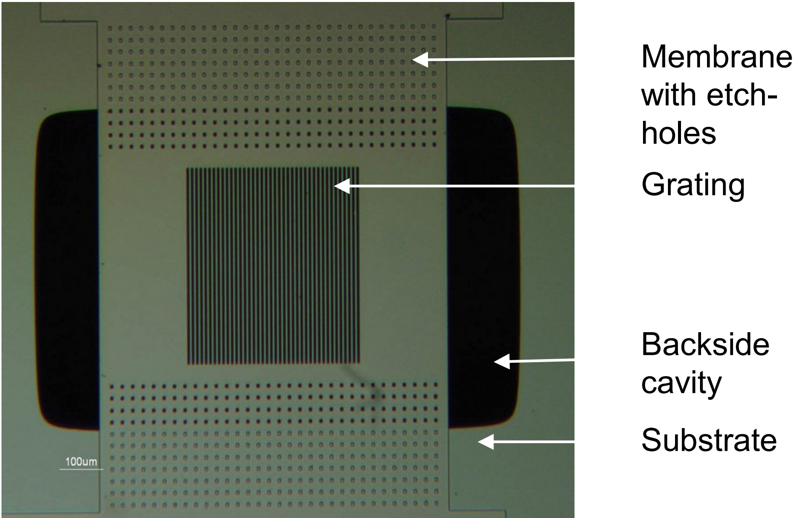

Figure 37 – A fabricated type 1 membrane

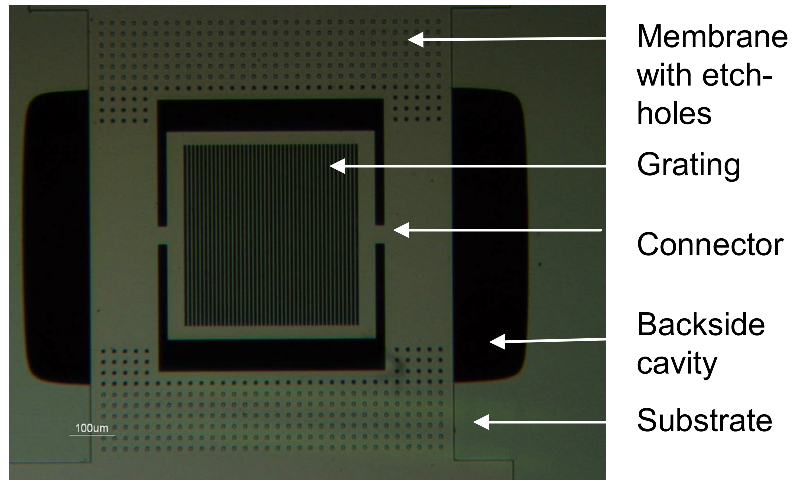

Figure 38 – A fabricated type 2 membrane layout

The chips are mounted face-up on printed circuit boards and the electrodes are wire-bonded. The conductive silicon is easy to wirebond without any metal electrode layer. Figure 39 shows such a picture of such an array.

The fabricated chips are examined under an optical profilometer and it is observed that the membranes are under a residual compressive stress, making them buckle upwards by approximately 50 nm (Figure 40). This upward displacement is at the center of the membrane which is 500 μm in length.

The devices have a very flat grating in buckled state and under actuation. Figure 41 shows a 3D profilometer picture of an actuated tunable grating. It can be seen that the tunable grating remains flat when the membrane bends due to the electrostatic actuation.

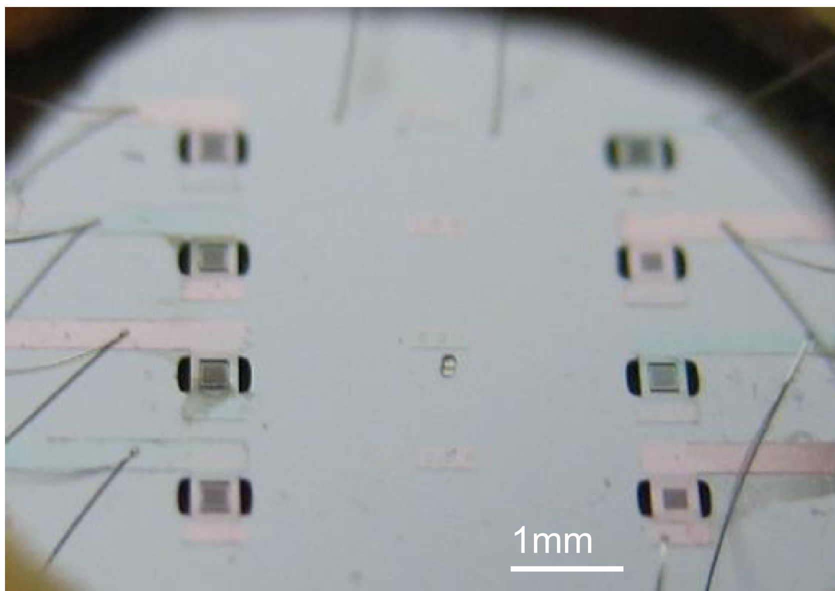

Figure 39 – Fabricated 4x2 array of tunable gratings on a chip. The devices and the substrate are wirebonded.

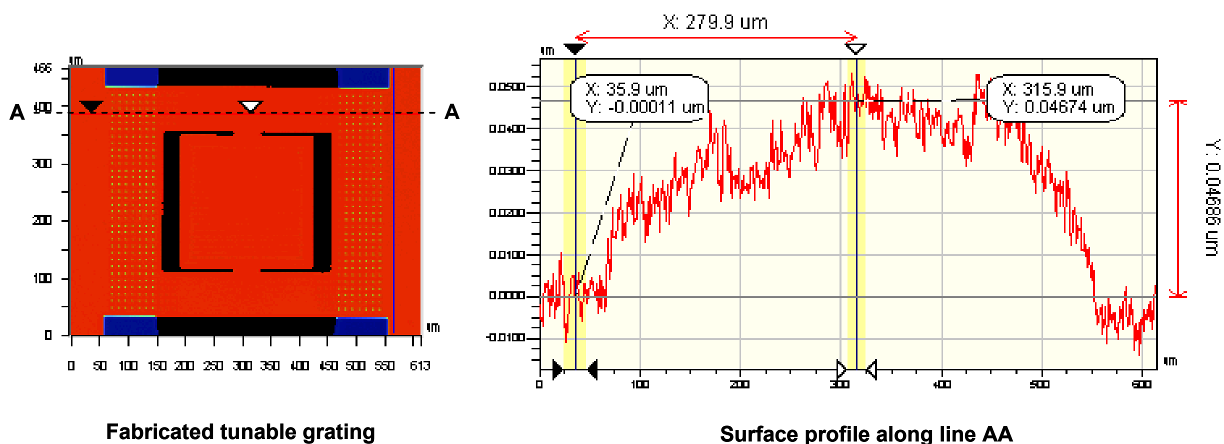

Fabricated tunable grating **Surface profile along line AA**

Figure 40 – Profile of the fabricated tunable grating. The tunable grating shows about 50nm upward buckling deflection

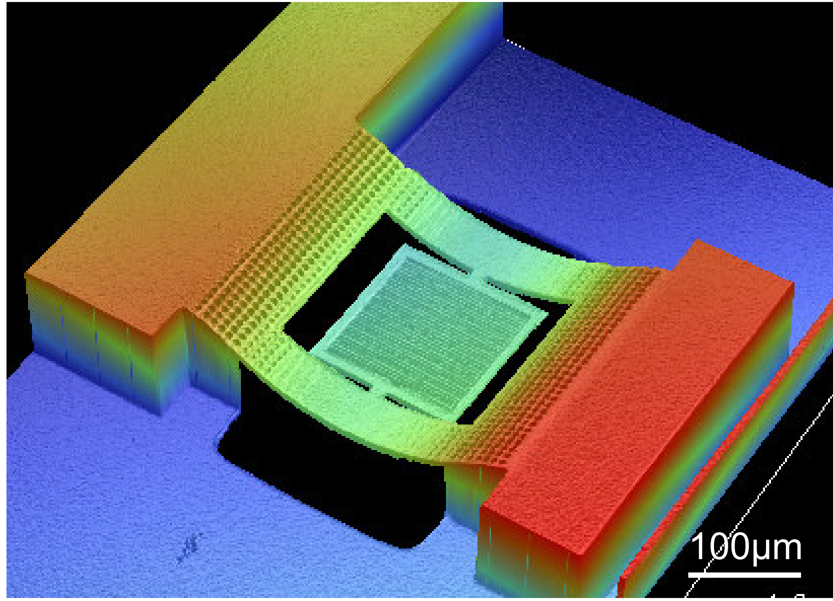

Figure 41 – 3D image of the tunable grating structure under DC bias actuation, obtained using an Optical Profilometer. Note that the grating remains flat

To test the flatness of the grating under the worst condition the membrane was actuated with 41V bias voltage (1V more than the maximum voltage in the operation). An optical profilometer image of this tunable grating is shown in Figure 42. It can be seen that the grating shows ~50 nm maximum deflection in the X profile whereas the Y profile shows less than 20 nm maximum deflection. For a laser beam of 50 nm diameter focused at the center of the grating, the flatness error of the grating is less than 10 nm at 41V bias.

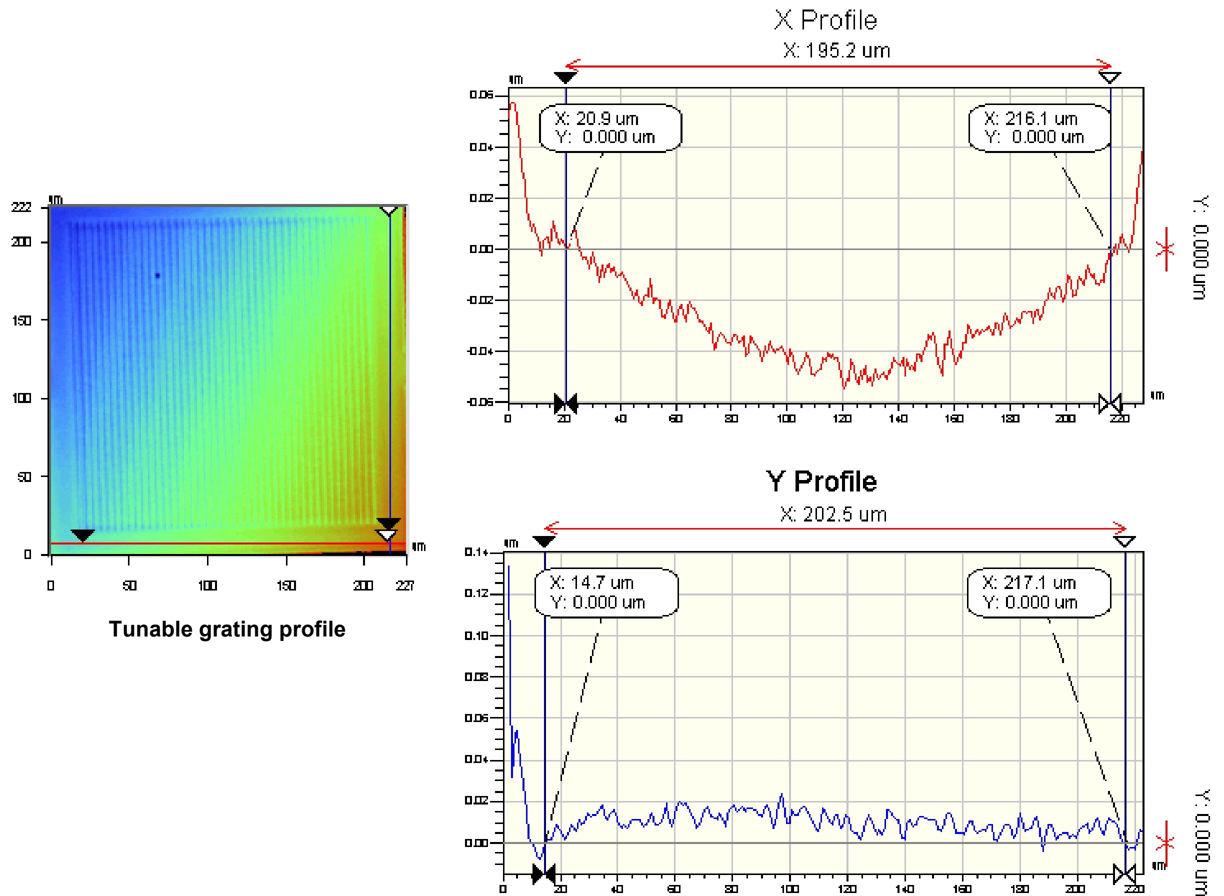

Figure 42 – Grating flatness test under profilometer, the grating is actuated with 41V electrostatic bias voltage

The fabrication process showed a yield of ~90% after parameter optimization. These devices were then assembled in a table-top optical setup to characterize their static and dynamic behavior using laser interferometry.

3.3 Characterization and comparison with FE model

As mentioned earlier, the tunable gratings enable miniaturized laser interferometry. Laser interferometry is used to characterize the tunable gratings.

3.3.1 Method and setup for characterization

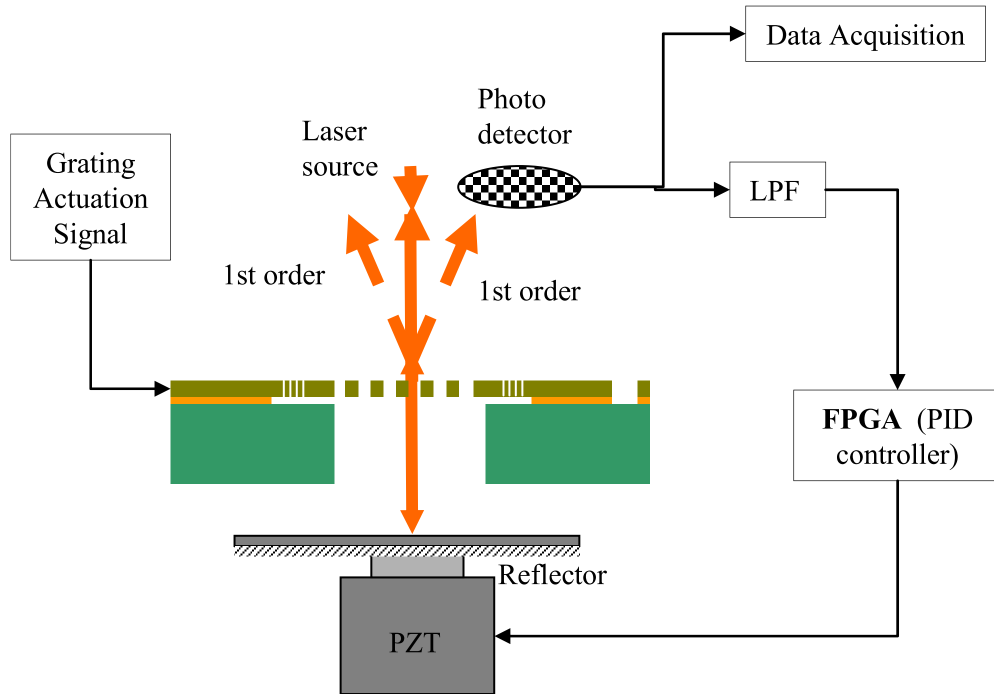

Figure 43: Experimental setup for the characterization of μSGI

For the static and dynamic characterization of the tunable gratings a pre-calibrated PZT is used as shown in Figure 43. (This characterization method uses a novel control algorithm developed for high bandwidth surface tracking and noise reduction, run on a Field-programmable gate array (FPGA) which discussed in detail in CHAPTER 4.) As shown in Figure 43, the reflector, mounted on a pre-calibrated PZT, is placed in front of the tunable grating. Focused laser beam is passed through the grating of the μSGI. One or both of the first orders of interference are captured by Photo-detectors (PD). The PD output is filtered using a low pass filter before it is fed to the FPGA, to avoid interference of the high frequency signal with the low frequency noise. The FPGA generates a real time analog output which tunes the PZT to the maximum sensitivity position on the optical curve. This way the PZT follows the motions of the grating at low frequencies (~1 kHz).

3.3.2 Static characterization

For static calibration, the grating bias voltage is varied sinusoidally in the operating voltage range (10V to 40V) at a low frequency (~20Hz). The PZT with active control, which maintains the distance between the grating and the sample to the highest sensitivity position in a fringe, in turn follows the displacement of the grating. The PZT behaves linearly in the given range of motion at this frequency; hence the bias voltage applied to the PZT can be converted in to displacements if the sensitivity of the PZT is known.

Finite element (FE) method is used with the help of ANSYS multiphysics to simulate the behavior of the grating under electrostatic loading as discussed in Section 3.1.4. The displacements obtained experimentally and from the FE simulation are plotted against the bias voltage of the grating as shown in Figure 44, which shows a good agreement. The membranes have a small upward buckling which snaps downwards around below 10V hence this voltage range is not used. The results are shown in operating voltage range; the initial displacement at 10V is matched for the two curves.

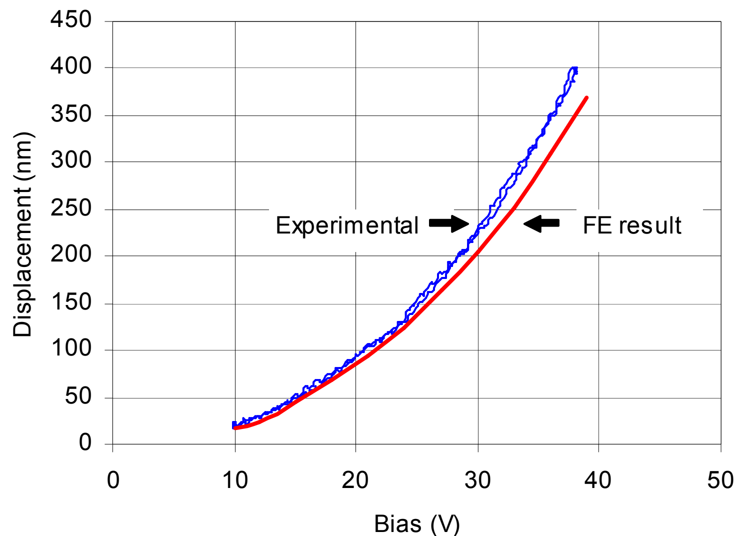

Figure 44: Deflection of grating vs. actuation voltages

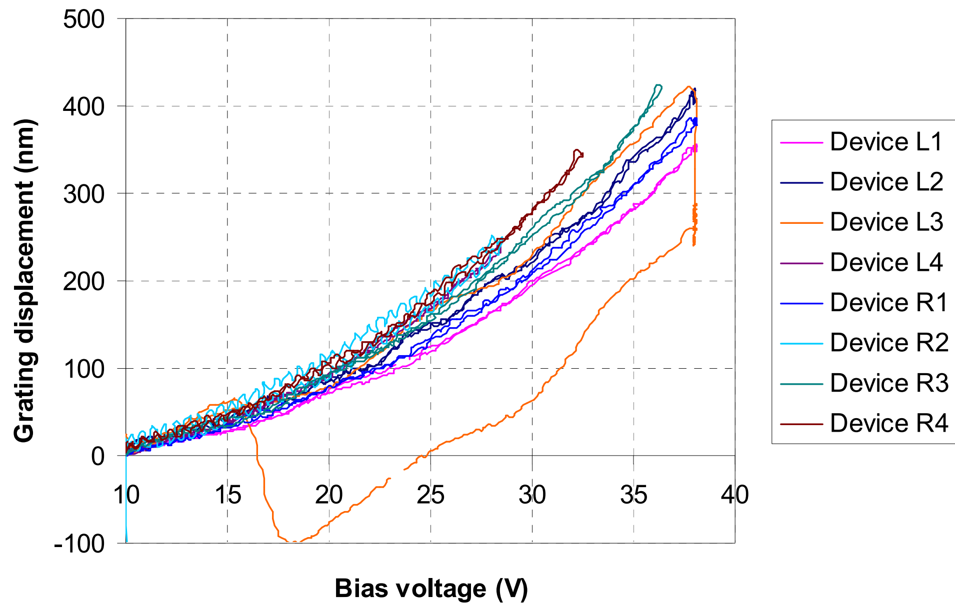

Figure 45 – Static characterization of multiple devices (tunable gratings) on a chip. Nomenclature indicates the location of the tunable grating e.g. L3 = 3 rd tunable grating from top in the left column of tunable gratings

Figure 45 shows the response of multiple gratings on a chip. It can be seen that the gratings have different displacement responses for voltage range between 10V to 38V. Device L3 shows a hysteresis curve with snapping of gratings at ~17V. For such gratings the useful range of voltages is from the snapping voltage to the maximum voltage applied. Different snapping voltages imply that the gratings are under different residual stresses which may be a result of fabrication non-uniformities. These calibration curves show some high frequency noise which results from the ambient vibrations. The calibration curve is filtered to obtain a smooth curve.

3.3.3 Dynamic characterization

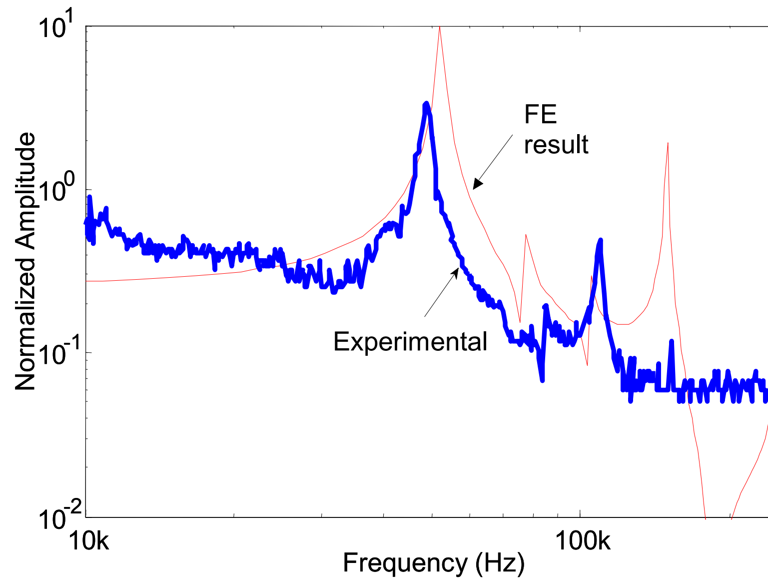

Figure 46 – Measured and FE modeled frequency response of the µSGI tunable grating

For the dynamic characterization of the tunable grating membranes the same setup is used. The grating is excited with a small magnitude (~0.1V peak to peak) sinusoidal signal. This signal is swept through the frequency range of interest and the amplitude PD output for each frequency is stored. Using the sensitivity of measurement, this output can be converted to displacement in nm.

The experimental and FE frequency response of a grating is shown in Figure 19. It can be seen that the first resonance occurs at around 50 kHz, which is high enough for active noise reduction in the required bandwidth of 1 kHz. The second order approximation of the frequency response has a small damping ratio of ~0.05. The FE result shows good agreement with the measured data in terms of capturing the resonance for the first 4 modes. The slight mismatch in the resonance frequencies can be due to different squeeze film damping effects for different mode shapes. The third harmonic shows a higher response magnitude in the measured data. The third mode of resonance is as shown in Figure 19 and the reflected beam from the grating fingers is at

an angle and do not interfere throughout the cycle of motion. This generates periodic oscillations in the amplitude of the PD output which are not related to interference. The fourth mode of resonance is not prominent in the measured data because of the high deformation of the grating surface in this mode.

Multiple devices are tested for their frequency responses using a dynamic spectrum analyzer. The responses are shown in Figure 47. 25V DC bias was applied to the tunable gratings and 200mV or 400mV amplitude AC signal was used to sweep the frequencies across the spectrum.

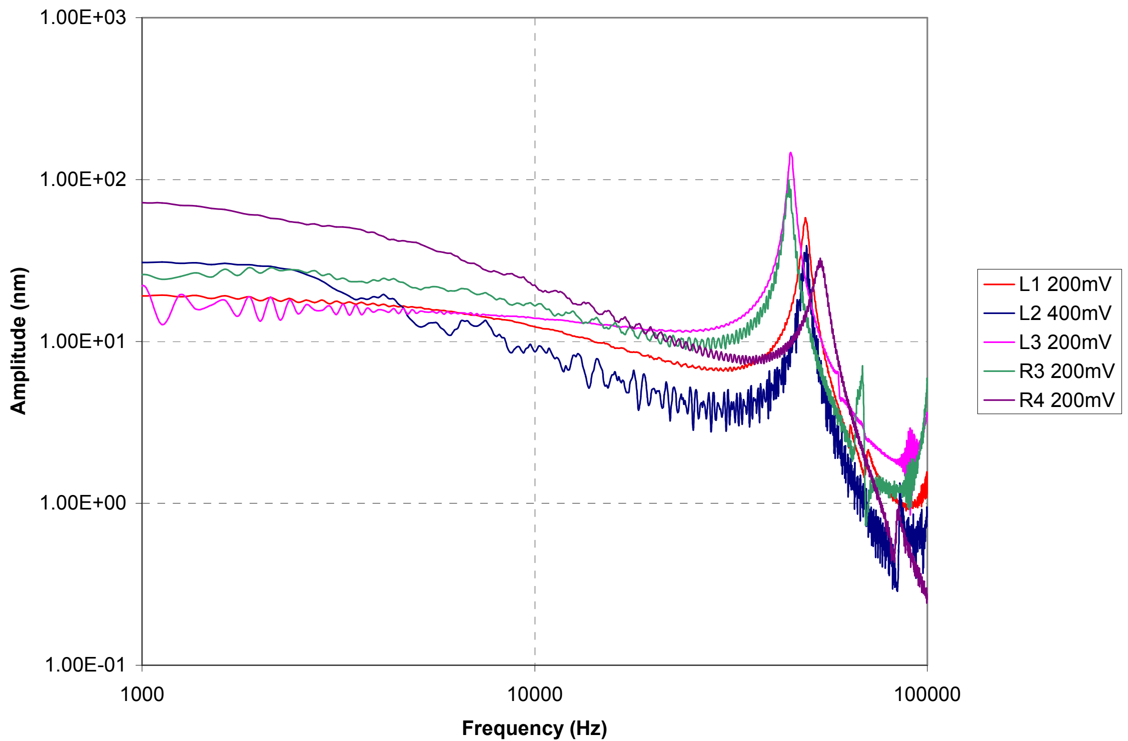

Figure 47 – Frequency response of multiple tunable gratings on a chip

Figure 47 shows the frequency responses of many devices on a chip. It can be seen that the gratings follow the same trend in terms of the resonance frequencies of the first mode. The gratings show different sensitivities to the voltage inputs which are due to the

different grating area factors (i.e. the ratio of finger width to the pitch of the gratings) and non-uniformities in the fabrication.

Note: The Y axes in Figure 46 and Figure 47 shows the amplitude of the vibrations in nm, which is obtained by multiplying the photo-detector signal by the corresponding gain. However, this is true only when the grating moves perpendicular to its plane (i.e. first resonance mode shape – bandwidth ~50 kHz). For higher frequencies the grating may not remain flat and perpendicular to the optical axis. Hence, the amplitude does not have any physical significance in the frequencies higher than the first resonance frequency. However, the resonant frequencies can be accurately captured by the optical method.

CHAPTER 4

OPTICAL SETUP FOR MICRO-SGI

The tunable gratings of the µSGI are miniaturized using MEMS technology and are batch fabricated to enable the array operation. The array implementation of the µSGI also requires the miniaturization of the optical assembly. This chapter explains in detail the design, simulation and implementation of the optical assembly.

4.1 Table-top optical setup

4.1.1 Single µSGI table-top optical setup

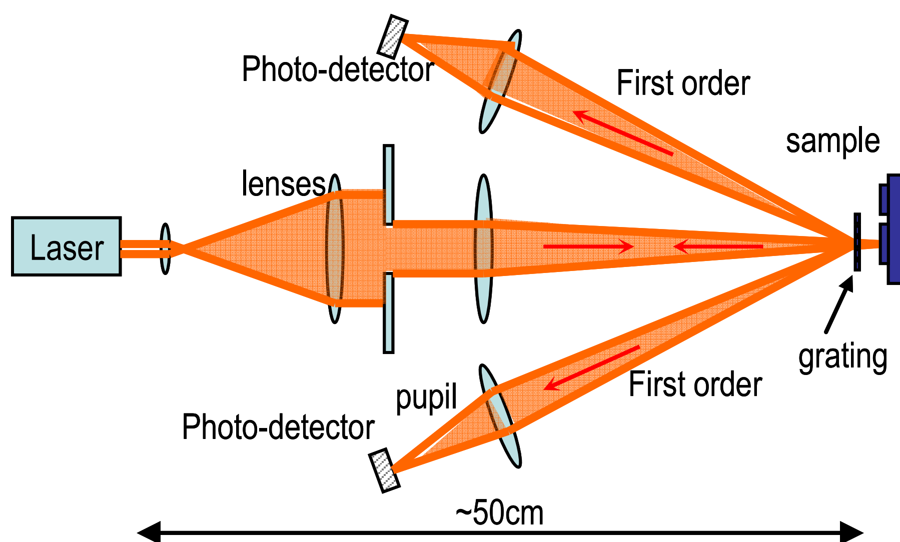

Figure 48 – Schematic of table-top optical setup for single µSGI operation

The initial tests of the µSGI were conducted on optical table. A Helium-Neon (He-Ne) laser with wavelength (λ) of 632.8nm and 2mW power was used as a source. For a single µSGI operation a setup as shown in Figure 48 was built on optical table. In Figure 48 the laser beam from the He-Ne laser source is expanded and collimated using a lens assembly. It is passed through a pupil or pinhole to reduce its size. The beam is then

focused on to the sample through the grating. The grating and the sample are placed close to each other (~1mm) to avoid significant size changes in the beam. The diffraction orders are focused on to photo-detectors using lenses.

4.1.2 Single µSGI table-top optical setup

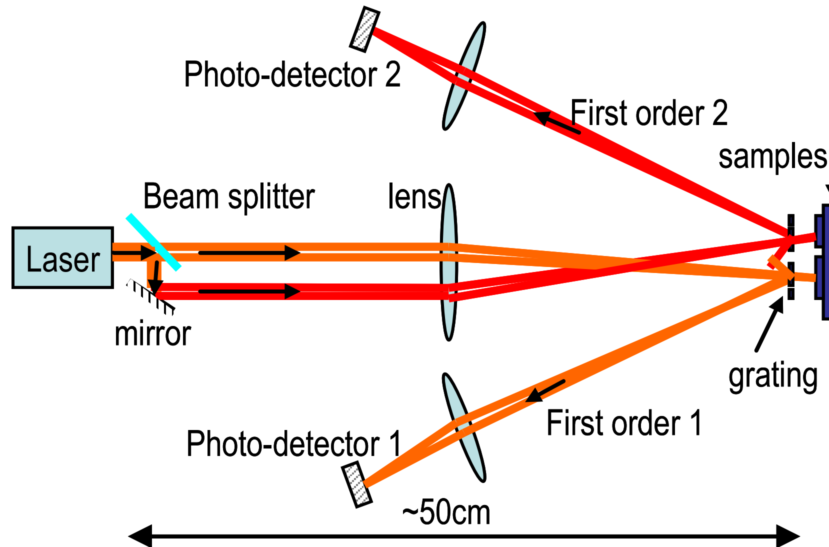

Figure 49 – Schematic of table-top optical setup for single µSGI operation

A 2x1 array of µSGIs can be illuminated using a setup as shown in Figure 49. The laser beam is split in to two beams and the beams are directed parallel to the original beam as shown. These beams are focused on to the sample at different spots. The location of the spots can be adjusted by changing the angle (tip or tilt) of the mirror. The beams are adjusted so that they illuminate two tunable gratings on a chip. The two tunable gratings generate two sets of diffraction orders. The respective first orders of diffraction are captured by two different photo-detectors. For easy detection of beams, the tunable gratings are chosen such that their grating periods are not identical to each other and the first orders are directed at different angles.

These optical setups were successfully implemented and some of the results obtained from these setups are demonstrated in CHAPTER 5. However from the perspective of

ease of operation and feasibility of array operation, these setups are not good. The table top setup is bulky (tens of centimeters in length). The array operation is achieved by beam-splitter mirror assembly which is not convenient for multitude of beams.

Another problem with the table top optical setup arises from the use of lenses to focus the beam on the sample through the grating. The distance between the grating and the sample introduces a mismatch between the curvatures of the interfering wavefronts as shown in Figure 50. This leads to circular fringes inside each order. This problem can also be solved by illuminating the grating with a collimated beam. This configuration is easy to implement using a fiber collimator assembly.

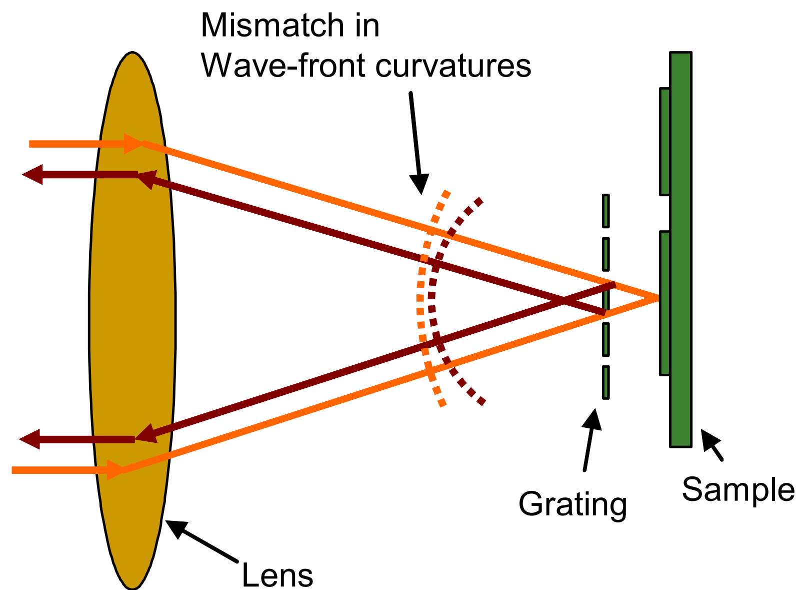

Figure 50 – Mismatching wavefronts interfere to generate circular fringes inside a fringe

4.2 Design of miniaturized optical assembly

To overcome these problems a miniaturize setup is developed. The schematic of the miniaturized optics setup is shown in Figure 51. The laser is carried to the system using optical fibers. Each fiber has an inbuilt collimator at the end which illuminates a pupil (or

pinhole). The beam gets cropped by the pupil to the desired beam diameter. The cropped beam passes through the tunable grating as shown. An optional microlens can also be assembled to generate a smaller spot on the sample which gives better lateral resolution.

If a microlens is used then the distance from the lens to the sample is determined by the focal length of the microlens. However, if the lens is not used then the distance is limited by the efficiency of the optics. As the sample moves farther the beam diverges and smaller parts of the reflected beam comes back to the lens and grating. Hence, the sensitivity of the reading reduces with the distance between sample and the grating.

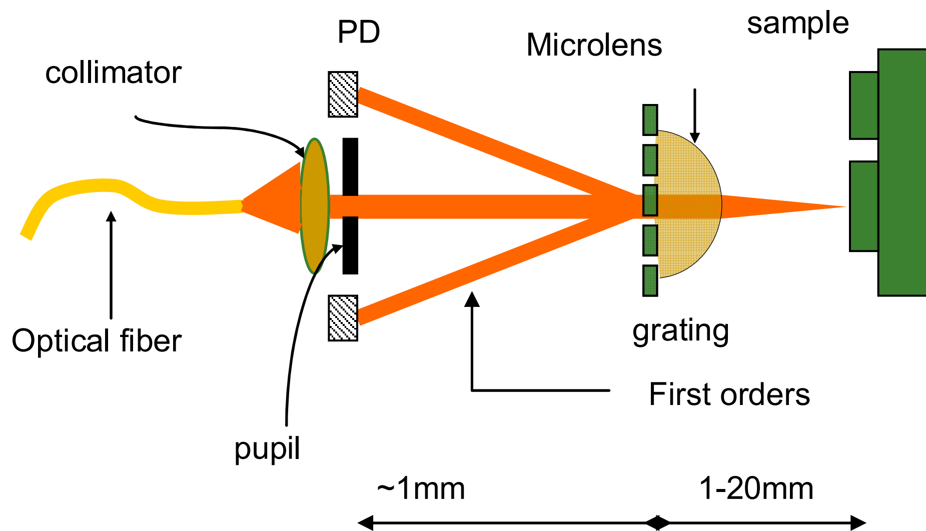

Figure 51 – Schematic of the micro optical system

4.3 Diffraction optics modeling and simulations

A diffraction optics based model is created in MATLAB to simulate the optical setup. The code computes the phase front by two methods – 1) Convolution method for short distances and 2) Fourier method for far field. This code has been modified from [68]. The

model can simulate both macro and micro setups. This code is used to design the micro optical system. The design parameters used are as follows $d_{pupil\text{-}grating}$=8mm; $d_{pupil\text{-}grating}$=8mm; pupil diameter=0.1mm.

The code is given in Appendix 7.2. The optical intensity profile at different planes is obtained during the simulation. The profiles for the chosen set of parameters are shown in Figure 52. A Gaussian beam (beam waist 280μm) is generated after collimation as shown in graph 1. The beam is then cropped by the pupil (graph 2). This beam travels to reach the grating to form Fraunhofer rings, a cross section intensity profile of which is shown in the graph 3. The beam then gets split into two due to the grating fingers. One part passes through the grating (graph 4) and the other is reflected back from the grating (graph 4B). The beam passing though the grating travels to reach the microlens where its profile becomes as shown in graph 5.

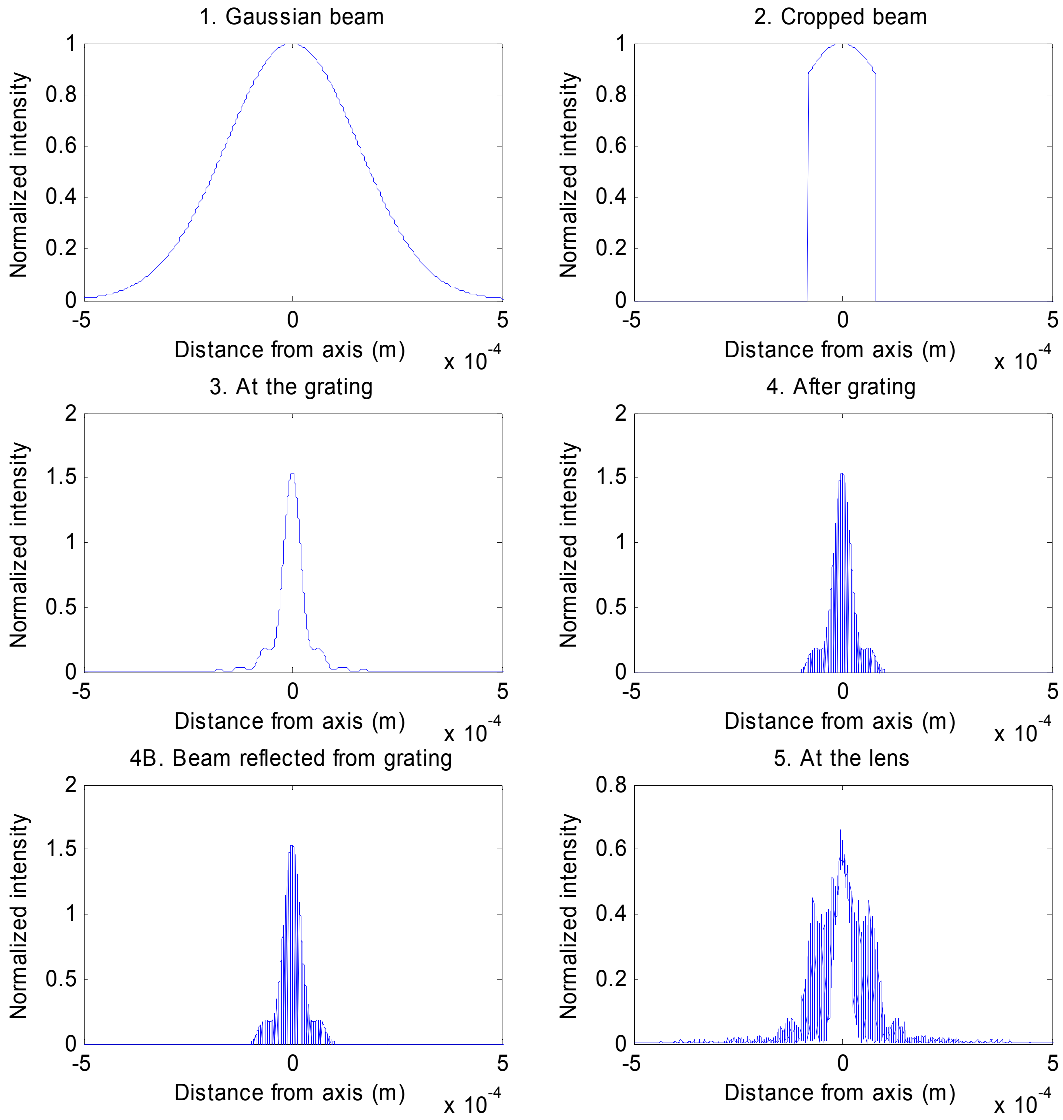

Figure 52 – Optical intensity profiles of the beam traveling from the collimator to the microlens (obtained from simulation)

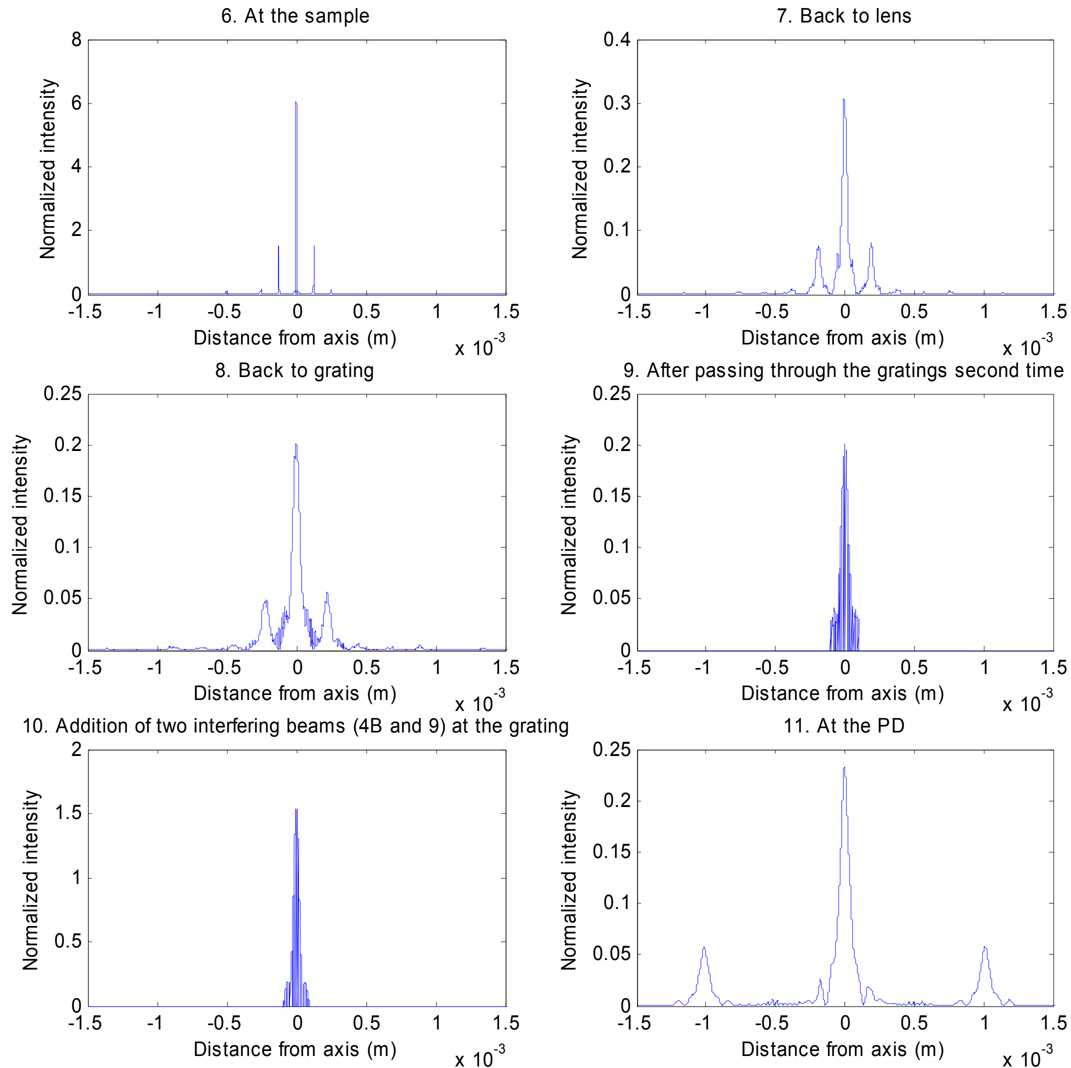

Figure 53 – Optical intensity profiles of the beam traveling from the microlens to the photo-detectors (obtained from simulation)

The microlens can be used if high lateral resolution is desired. Figure 53 shows the optical intensity profiles of the beam when a microlens is used. In Figure 53, the graph 6 shows the profile of the beam at the sample and the diffraction orders focused on the sample surface. The beam reflects back to the lens and the grating (graph 7 and graph 8). Only the zeroth order passes through the grating (graph 9). This beam interferes with the beam reflected from the grating fingers (Figure 52 graph 4B). The addition of the beam at the grating surface is shown in graph 10. The interfering beams travel to the

photo-detector plane where an order separation of 1mm is obtained. The intensity of the first diffraction order is measured at this plane.

When the microlens is not used, the beam profiles change mainly at the sample surface as shown in Figure 54 graph 6. The beam traveling back to the lens or grating plane (Figure 54 graph 7) assumes a shape similar to the earlier case where lens is used (Figure 53 graph 7).

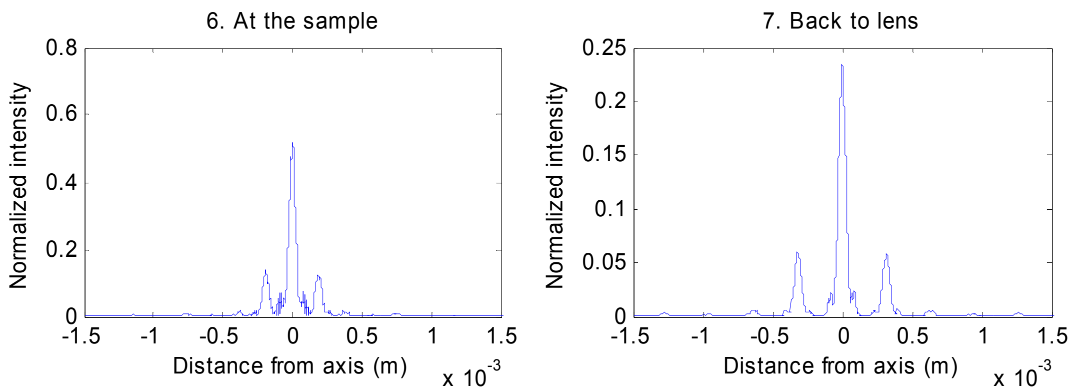

Figure 54 - Optical intensity profiles of the beam traveling from the grating to the photo-detectors when no lens is used (obtained from simulation)

The intensity of the first order is obtained by integrating the optical power over the first order. The optical curve can be obtained by changing the distance of the sample and can be plotted as shown in Figure 55. It can be seen that the valley of the optical curve does not reach zero intensity. This is because of the different intensities of the interfering beams. The intensity of the beam reflected from the grating (4B) depends on the reflectivity of the grating surface and the area factor of the grating. On the other hand, the intensity of the beam coming from sample (9) depends on the area factor of the grating, losses in the lens and the reflectivity of the sample. The lens-loss is neglected in these simulations and the reflectivities are assumed to be 1 for the case shown. The losses and lower reflectivity will result in reduced amplitude of the optical curve. One

sample optical curve obtained from the table-top optical setup is shown in Figure 56. For this curve, the sample is placed on a PZT and is actuated at 100Hz ~300nm amplitude.

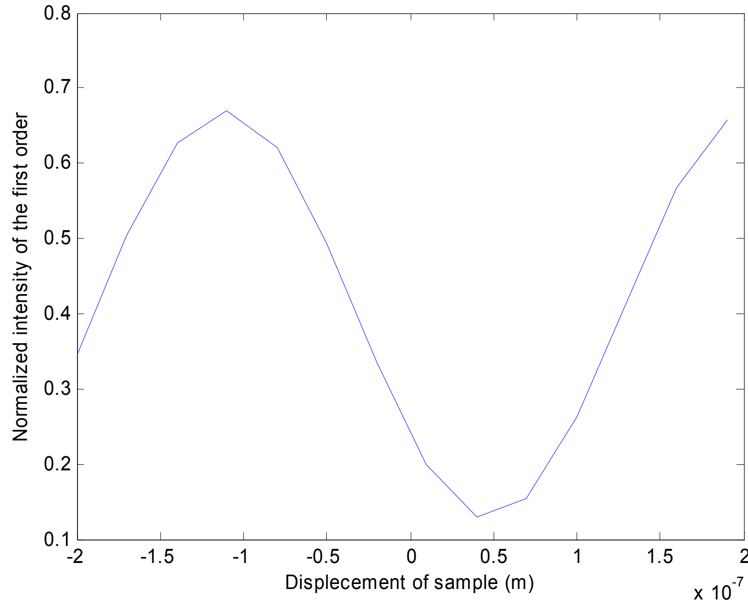

Figure 55 – Optical curve obtained from the simulations

As discussed earlier the table-top setup generates circular fringes inside each of the orders. This is verified by the simulations. One such first order is shown in Figure 57. The circular fringes behave as if they are diffraction orders. Hence, when the sample moves by half a wavelength distance, the bright circular fringe becomes dark and the dark fringe becomes bright. Hence, the overall intensity of the first diffraction order changes negligibly. This is avoided by the miniaturized setup where the collimated beam is passed through the grating. A zoomed in first order profile obtained from the miniaturized setup is shown in Figure 58; no fringes can be seen inside the order.

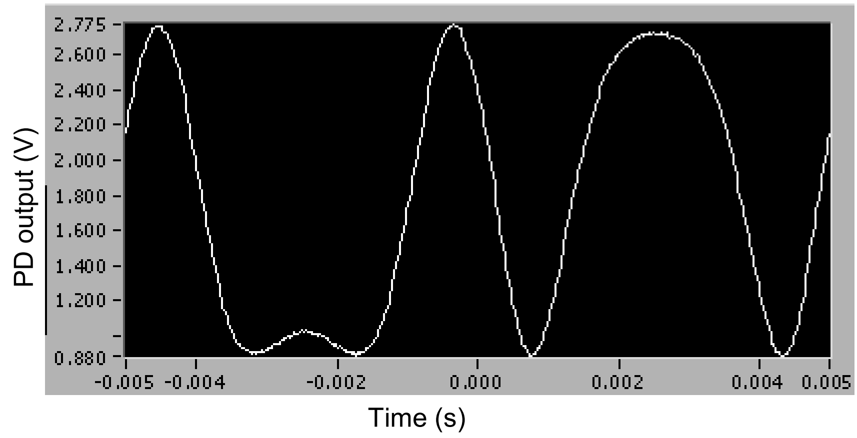

Figure 56 – Sample optical curve obtained from experiments

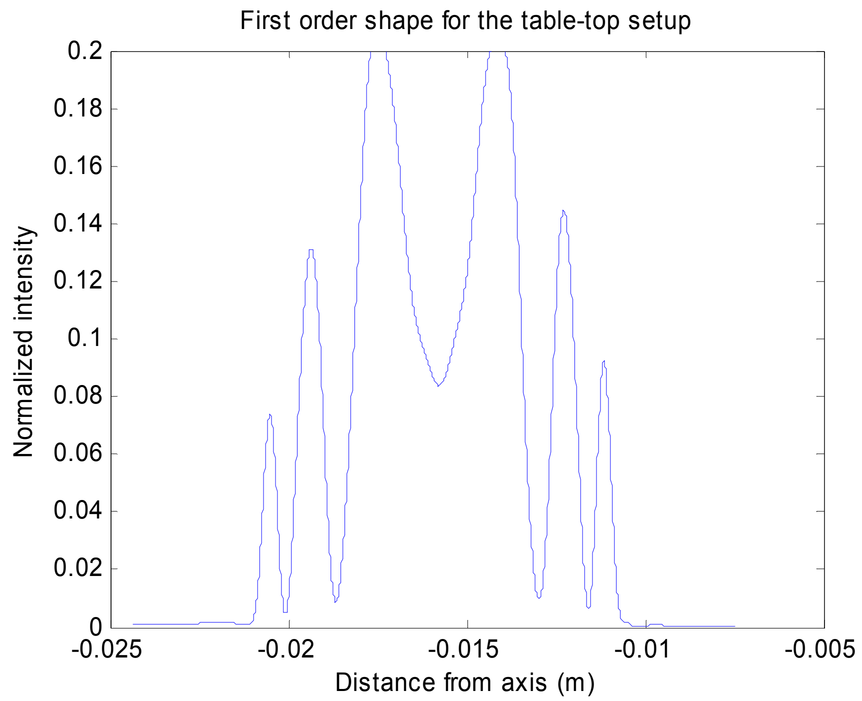

Figure 57 – Circular fringes generated by the table-top setup

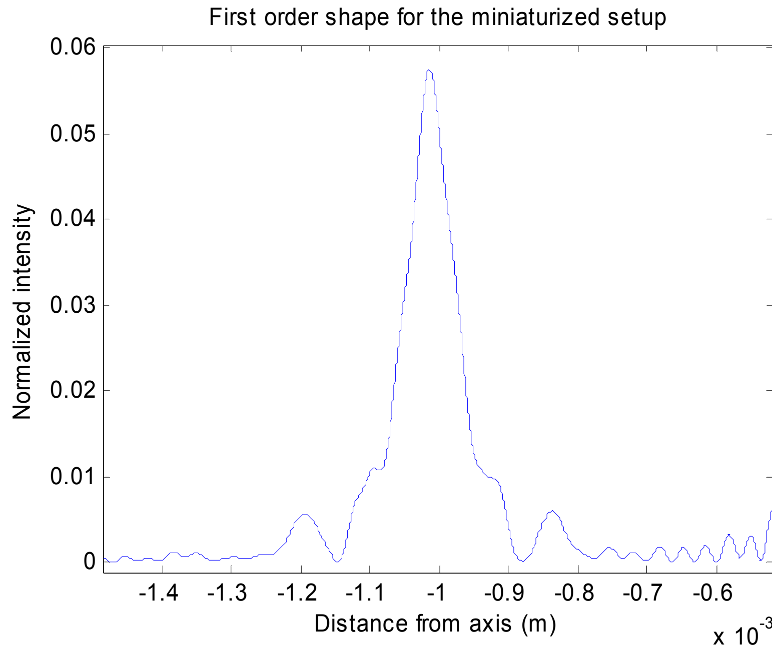

Figure 58 – No significant circular fringes are generated by the miniaturized assembly setup

4.4 Miniaturized optical setup

4.4.1 Design of optical assembly and fabrication using stereo-lithography

The miniaturized assembly contains the tunable grating chip, the fibers and collimators, the photo-detectors and electrical connections. All these are perfectly aligned to each other and fit in a small space. The alignment is critical for good optical performance of the µSGIs. As these parts are made independent of each other, some supporting structures are required for assembly. These supports or holder structures are designed such that the assembly process is simplified.

Stereolithography technique was chosen to fabricate the holder structures. Stereo-lithography enables fabrication of complicated three dimensional holders. The holders are designed using AUTOCAD 3D. A schematic of the assembly structure in its final form is shown in Figure 59.

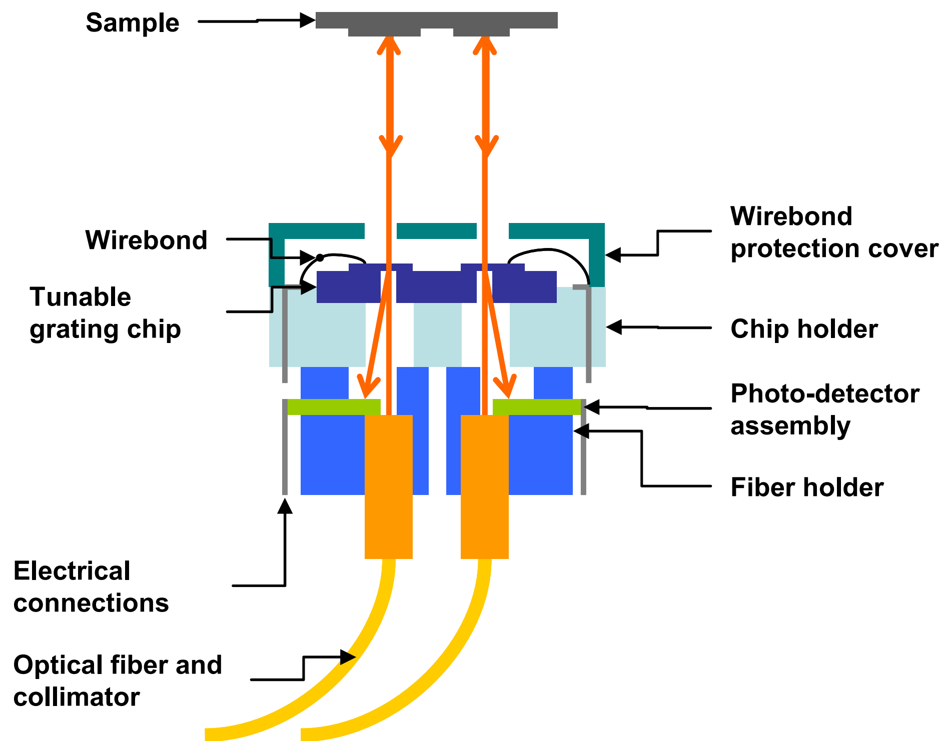

Figure 59 – Schematic of the miniaturized assembly

The assembly consists of a chip holder which supports the chip and provides an array of through holes to pass electrical connectors through. The chip holder also has two cavities inside so that laser can be passed though it and the first orders can be accessed from the backside without any hindrance from the holder. A wirebond protection cover is used to cover the wirebonds of the tunable grating chip. This surface of the μSGI gets exposed to the sample and can get damaged during sample handling. The wirebond protection cover can also be used for mounting the microlenses optionally.

Fiber and collimator are supported by a fiber bolder. The holder has a cavity which tapers towards its closed (upper) end. This allows an easy friction fit assembly of the collimator structure. The photo-detectors are placed in a small holder and are glued to electrical conductors by conductive epoxy. This assembly is also friction-fit in to the fiber

holder and it is also aligned to receive the first order beam. The three dimensional vies of these structures are shown in Figure 60.

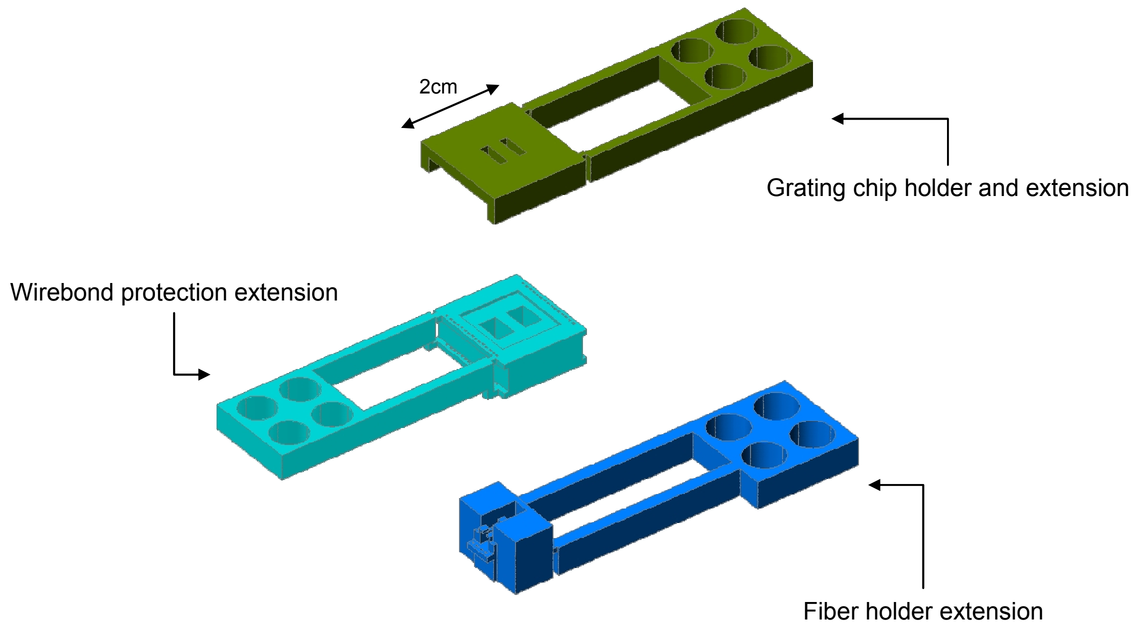

Figure 60 – 3D view of the holder structures and their extensions

These structures are designed to have extension structures for the ease of assembly. The dimension of any holder by itself is smaller that 2cm X 2cm X 1cm and it is difficult to handle these structures. The extensions allow easy handling. The extensions have small holes at the other ends and are used to mount the holders on three dimensional (XYZ) linear and rotational stages. The XYZ stages have high resolution and allow an easy way to align the micro-optical parts. The fabricated holders are shown in Figure 61.

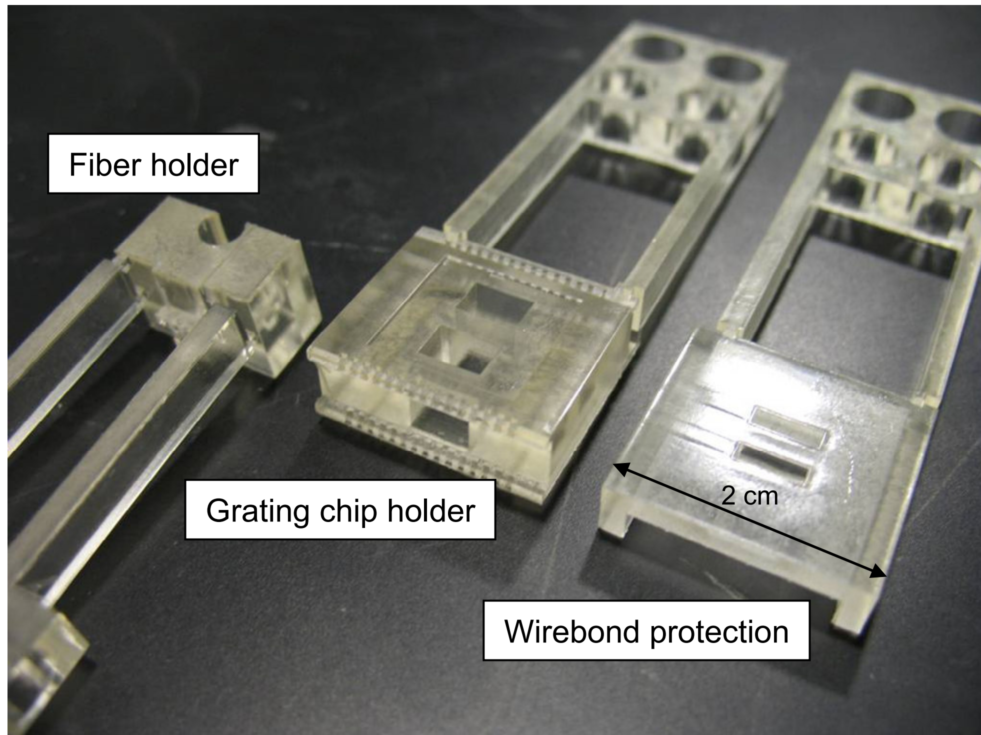

Figure 61 – Fabricated holders for miniaturized assembly

4.4.2 Miniaturized assembly process sequence

The assembly process begins with the fabrication of the holders using stereolithography. The chip holder is assembled first. (Figure 62) Gold coated rectangular cross section wires are passed though the array of holes on two sides of the chip holder. These wires are bent flat towards the chip on the front side. The wires are glued to the chip holder firmly using UV cured epoxy making sure that the top surfaces of the wires are not contacted by the epoxy. A fabricated chip is placed in the chip holder in the cavity made for the chip. The chip is then glued to the chip holder using ultra-violet (UV) cured epoxy. The chip holder assembly is then placed under the wirebonder to make wirebonds between the tunable grating electrodes and the gold coated wires as shown in Figure 62. Small dabs of epoxy are placed at the bonds to provide an addition support to the bonds. The chip holder is then mounted on a XYZ stage.

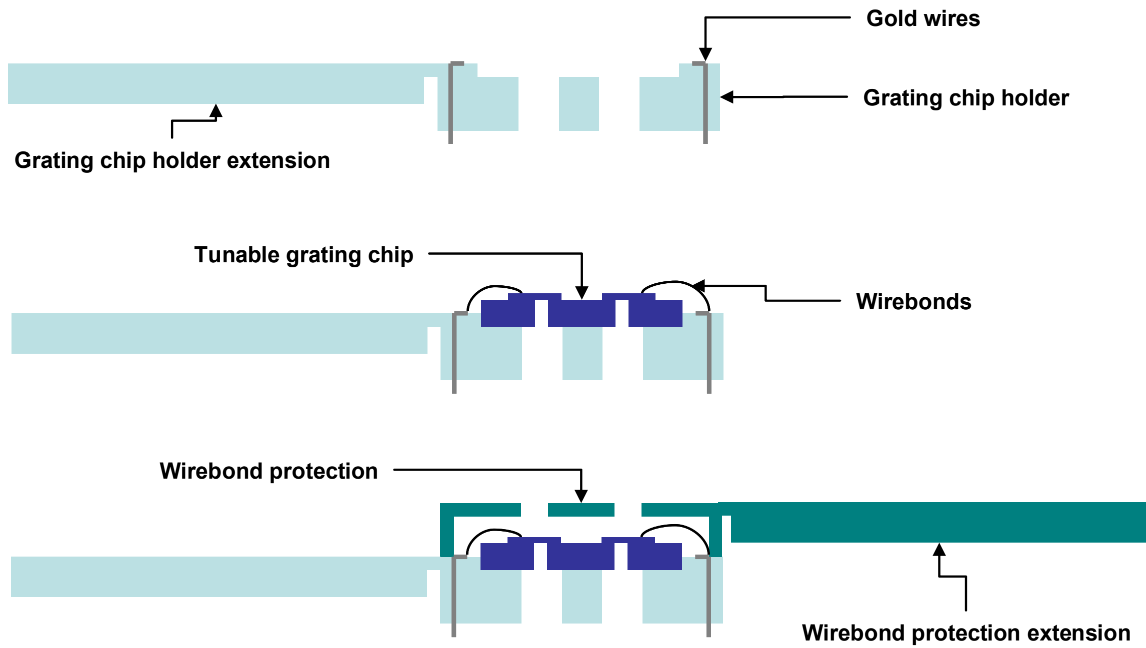

Figure 62 – Miniaturized assembly process sequence 1

The wirebond protection cover is mounted on another XYZ stage. The two are aligned and brought together and glued using superglue. The wirebonder protection extension is then cut off to leave the chip holder and wirebond protection cover assembly held on the chip holder extension.

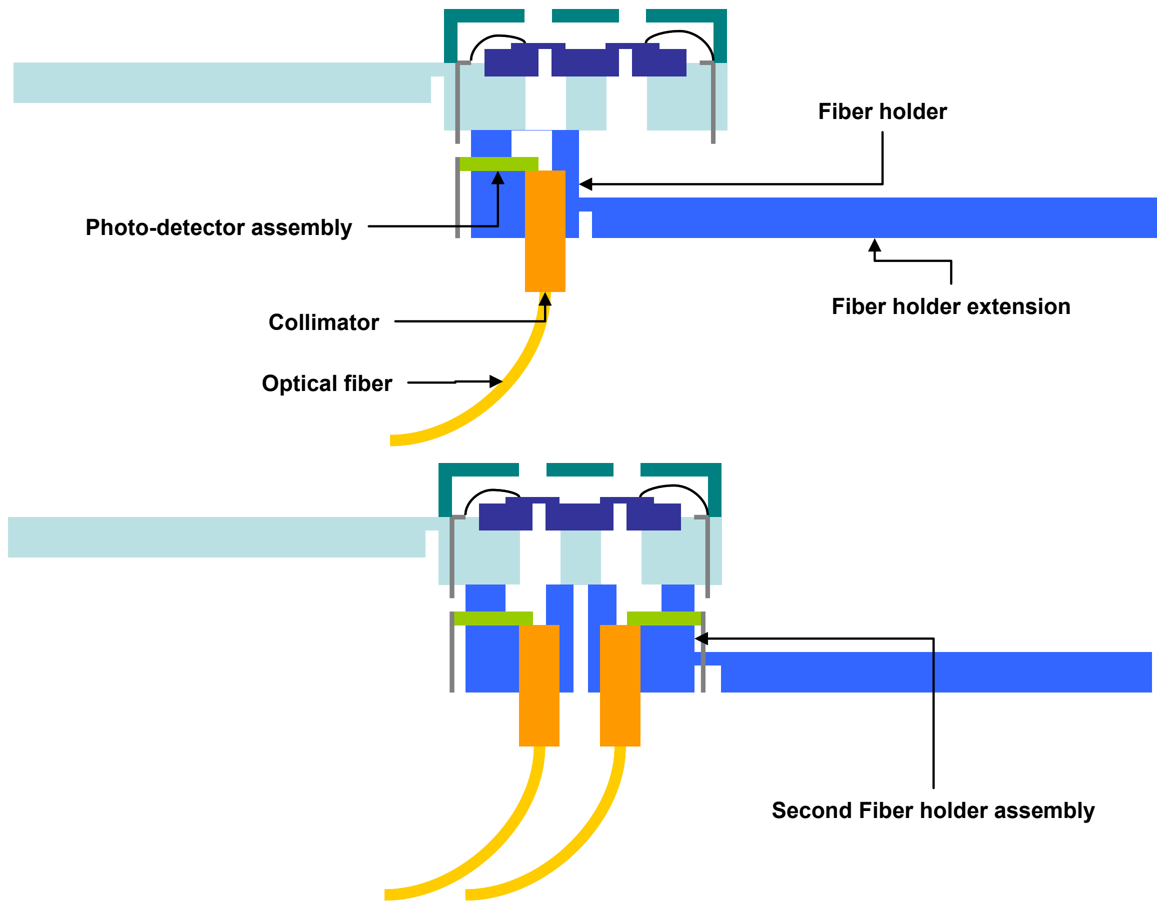

Figure 63 - Miniaturized assembly process sequence 2

In the next step the fiber holder assembly is built by friction-fitting the optical fiber and collimator. The parts are also glued using UV cured epoxy. This assembly is then mounted on the second XYZ stage. The laser is switched on and the fiber holder assembly is aligned with chip holder assembly. (Figure 63 and Figure 64) The diffraction orders coming out of the grating serves as a good feedback for the alignment process. When the alignment is nearly done, a flat sample is placed in front of the grating. Either the sample or the tunable grating is actuated and the photo-detector (PD) signal is observed. The alignment is fine tuned to maximize the optical output on the PDs. After the alignment is finalized the assemblies are glued using superglue. The process is repeated for more fiber assemblies.

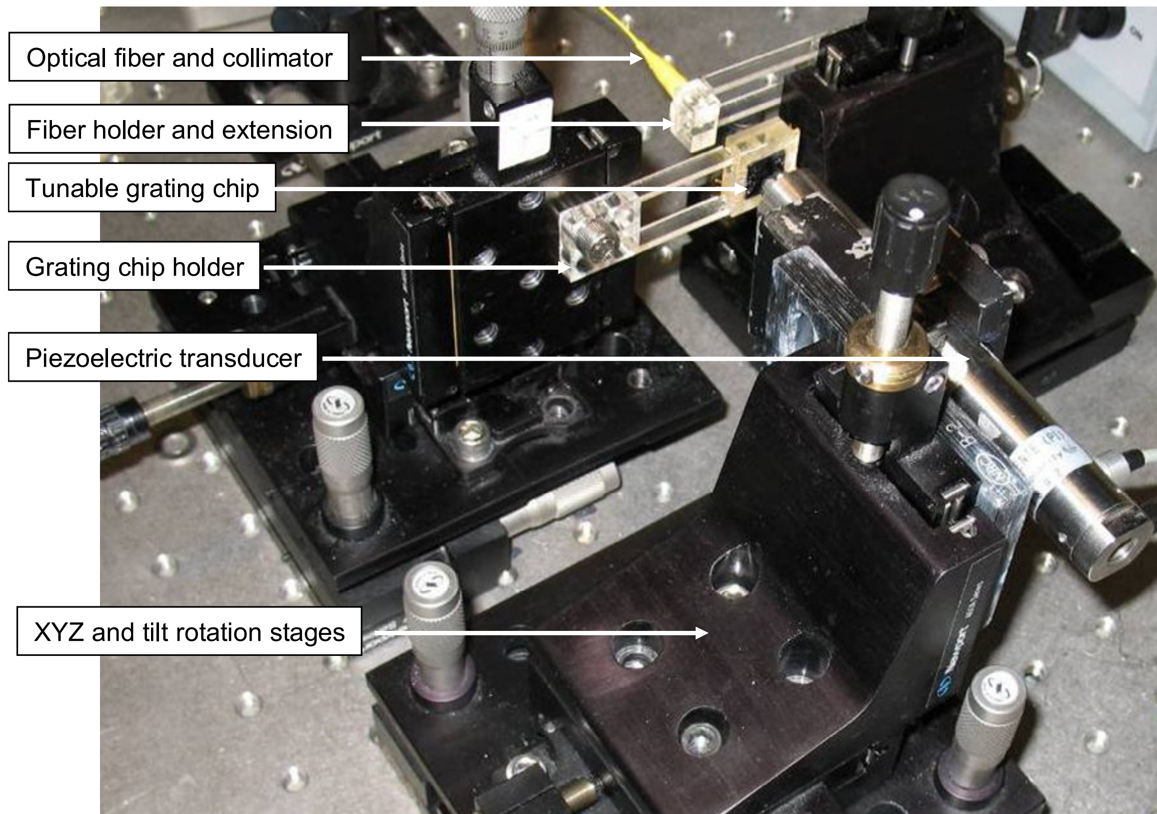

Figure 64 – Miniaturized assembly using XYZ stages and sample placed on actuator

At the end all the extensions are cut off. The assembly is placed in a shielded box with holes in the front and back for laser beam and fibers to pass through. One such assembly is shown in Figure 65 and Figure 66. SMA connectors are used to provide electrical connections to the photo-detectors and tunable gratings.

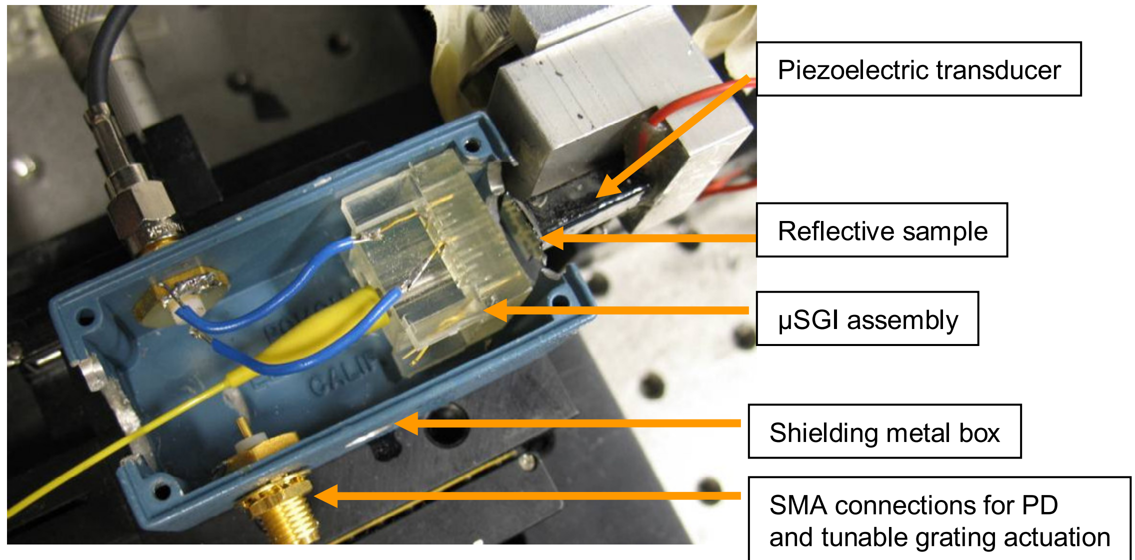

Figure 65 – Miniaturized assembly placed inside a shielded box

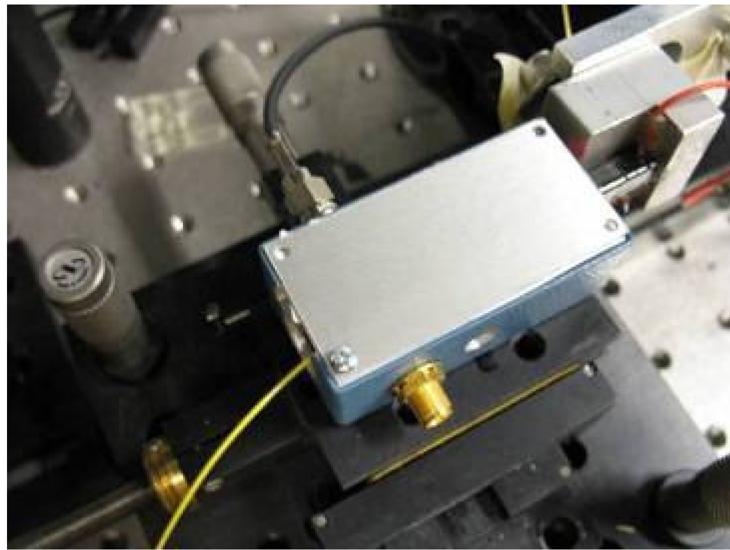

Figure 66 – Miniaturized µSGI package mounted on a XYZ stage for alignment

4.5 Spot size measurement

The spot size of the laser on the sample determines the lateral resolution of the measurement. A quartz based sample with 40µm metal line (Figure 67 is placed on a PZT actuated stage and the stage is mounted on XY automatic linear stages. To detect

the spot size conventionally a sample with well defined edge is scanned. The distance travelled to saturate the edge effect gives the spot size.

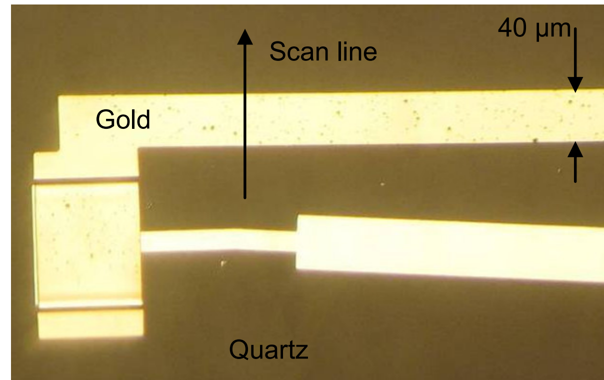

Figure 67 – Spot size measurement sample

In the case of μSGI, the PD output not only depends on the sample reflectivity but also is a function of the distance between the grating and the sample. The ambient vibrations tend to change this distance a lot which can affect the edge measurement. Instead, the reflectivity of the sample itself is used as a measure for the spot size.

The sample is placed on a PZT (Z direction) and automatic linear stages (XY direction). Hence it can be simultaneously actuated in the Z direction and moved at a steady velocity in the X or Y direction. If the amplitude of the Z vibration is greater than a half-wavelength, irrespective of the distance between the grating and the PD output scans the whole optical curve. The envelope of the PD readings give us a measure for the reflectivity of the surface and hence the spot size.

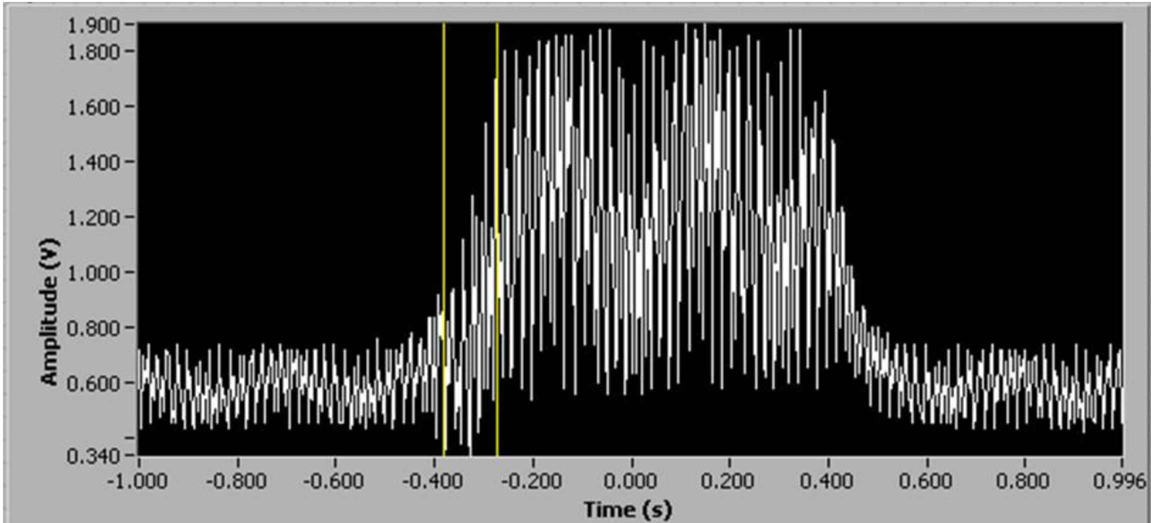

Figure 68 – Spot size measurement with lens integration – raw data

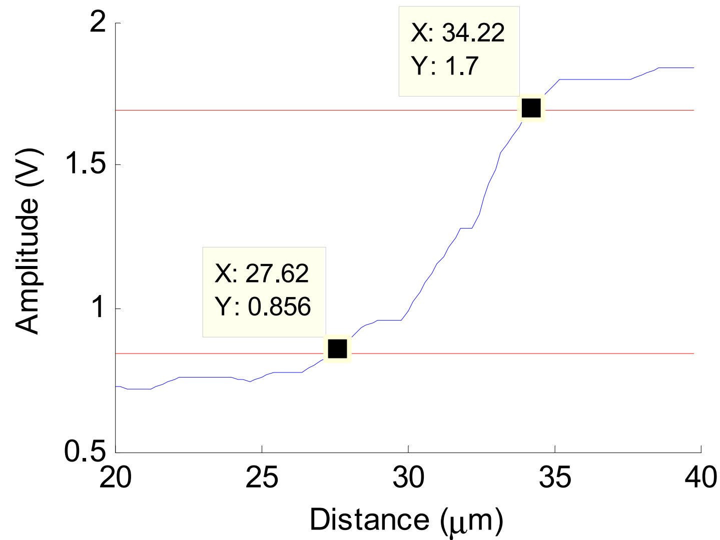

Figure 69 – Spot size measurement amplitude envelope

The FIRAT sample was moved at a constant velocity of 50μm/s to scan an electrode line (~40μm wide). The sample was actuated by the PZT stage at 100Hz ~600nm peak to peak amplitude. The optical intensity measured by the photo-detectors is acquired and visualized by using oscilloscope. The optical response obtained is shown in Figure 68. The amplitude envelope of the date is shown in Figure 69 which shows that the intensity

changes from 10% to 90% in 6.6 µm. Hence, the spot size or the lateral resolution of the µSGI is 6.6 µm.

4.6 Vertical resolution of the µSGI

The vertical displacement is measured in the form of photo-detector signal and it needs to be converted to displacements to understand the vertical resolution of the µSGI. The optical curve (Figure 56) can be used to calculate the sensitivity of the readings. The peak to peak amplitude (V_{pp}) of the optical curve, which is proportional to the reflectivity, can be used to determine the sensitivities of the measurement at the given point. The sensitivity at the highest sensitive point on the optical curve is given by

$$Sensitivity = \frac{\lambda}{2\pi V_{pp}} \qquad \textbf{(4.1)}$$

E.g. the optical curve shown in Figure 56 shows a sensitivity of 53nm/V.

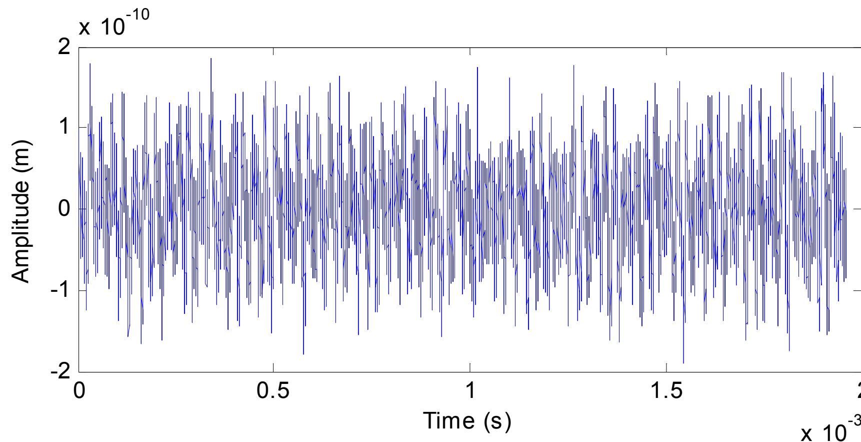

Figure 70 – Vertical displacement resolution from noise measurements

The measurement noise can be converted to displacements using the sensitivity value which gives us the displacement measurement noise. This experiment is performed at 100 MS/s and 0.2M sample points are collected over 2ms. The time series of data is

shown in Figure 70. This data gives a root mean square (RMS) value of 0.78mV which corresponds to 0.052 nm RMS vertical resolution. The bandwidth of the photo-detector used is 875 kHz. Hence, the root mean square noise of the μSGI over 875 kHz bandwidth is 5.93×10^{-5} $nm_{rms}/\sqrt{Hz}$.

CHAPTER 5

LOW NOISE CONTROLLER FOR INTERFEROMETERS

As mentioned earlier, initial positioning, vibration and acoustic noise can cause a significant change in the sensitivity of the measurements as well as introduce errors in the readings. The tunable grating of µSGI is designed to reduce this effect by implementing an active control. The mechanical vibration noise mostly occurs below 1 kHz. To operate an array of scanning grating interferometers, each interferometer requires a different actuator for noise cancellation. This is due to the topographic variation of the samples under observation and the different magnitudes of vibrations that might be present at different points over it. The independent actuation capability enables an array of µSGIs to be used simultaneously with high sensitivity and reduced noise.

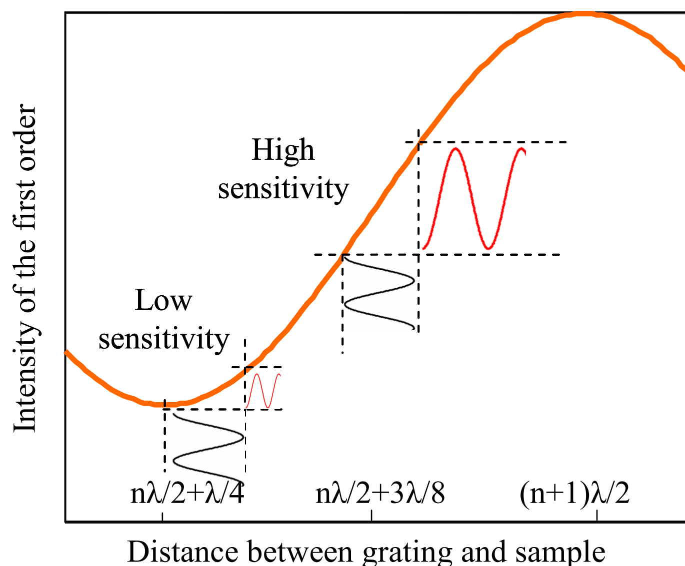

Figure 71 - Schematic of the optical intensity curve

As discussed in the introduction of the interferometry in the section 2.3 the optical curve for the interferometers is a non-linear curve as shown in Figure 71. It is a squared

sinusoidal curve with λ/2 periodicity. The optical curve has high sensitivity at the inflection point, which is the desired point of operation for very high resolution measurements. The active path stabilization method is implemented to actively move the grating to the desired point of operation. This chapter details the active path stabilization, the conventional methods to implement it and the novel recurrent calibration method and its implementation on μSGIs.

5.1 Design of active path stabilization

The schematic of the active control of the tunable grating interferometer is shown in Figure 72. The signal being measured is high frequency low amplitude vibration and the low frequency vibration noise comes from the ambient or acoustic vibrations and positioning errors. The total displacement signal is then converted to electric signal by photo-detector sensors (F(s)). This electric signal can be acquired by data acquisition systems or it can be observed real-time on scopes. This signal is used as a feedback for the closed loop control. The controller (C(s)) uses a low pass filter to separate the low frequency vibration noise from the signal. This noise is then processed as an error signal and a signal is generated to reduce the noise. The signal is fed to the tunable grating actuator (A(s)). The tunable grating is actuated by electrostatic voltage in one direction and is pulled back by the spring force in the other direction. The tunable grating moves in order to cancel the vibration noise and maintain the operation at the desired point of operation.

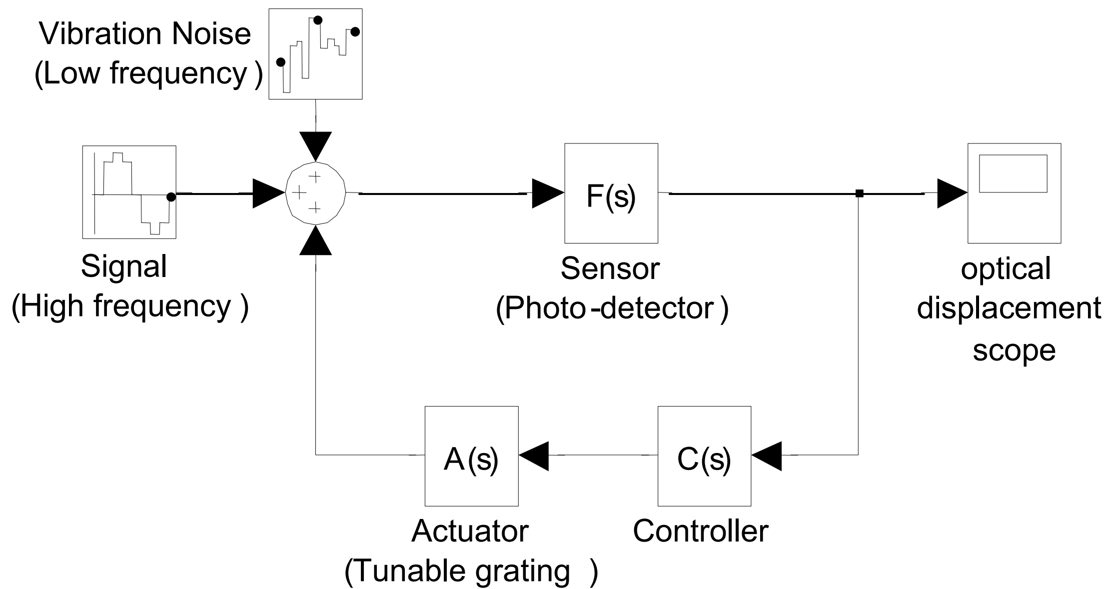

Figure 72 – μSGI active noise control system – block diagram

Figure 73 shows an optical curve over one λ (632 nm for He-Ne laser). It can be seen that the desired points of operation occur at every λ/4 distance. However, it is important to note that the slope of the optical curve at every consecutive desired point of operation has opposite signs; hence the stable controller gain (I for an integral controller) also needs to have different polarities accordingly. The phase of the measured signal also changes by 180° if the slope of the curve changes.

Different methods of active path stabilization exist as discussed in the next section. If the method requires characterization of the optical curve then the grating must at least be able to move by λ/2 (316 nm). This displacement is denoted by the required range of motion and it is sufficient to characterize the optical curve for a laser with λ=632 nm or less.

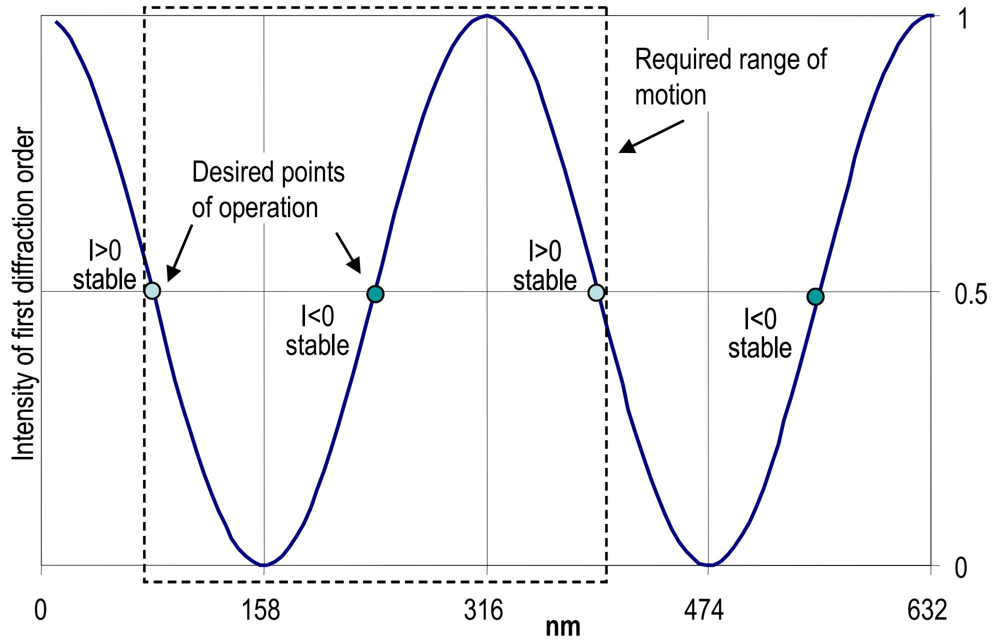

Figure 73 – Normalized optical intensity curve for the first diffraction order

5.1.1 Methods for path stabilization

Several methods have been implemented to reduce the sensitivity errors and vibration noise in different interferometric metrology systems. These include detecting the harmonic distortions by modulating the length of optical fiber or modulating the Fabry-Perot cavity [58], modulating the reference position [59]. Other phase-locking methods like optical intensity feedback [60] and optical feedback [61] actively tune the frequency of the laser to achieve highest sensitivity and vibration reduction. Fringe motion has also been used for phase-locking [62]. Fourier analysis techniques to separate low frequency error has also been demonstrated [63].

The harmonic distortion based method is advantageous in interferometric metrology systems, where the phase of the reference beam in the interference system can be easily modulated by modulating the reference mirror. It does not need initial characterization of the optical properties of sample. Graebner et al. demonstrated that a scanning laser interferometer with active noise control can reduce the effect of low

frequency vibrations successfully using harmonic distortion based method [53]. A resolution of $3x10^{-4}$ nm/√Hz and a bandwidth of 6 GHz was demonstrated using this technique [12]. Harmonic distortion based method is also implemented on grating interferometers (µSGIs) [66]. For high accuracy and flexible parallel operation, the harmonic distortion detection can be implemented with a discrete Fourier transform (DFT) based method in digital domain using field-programmable gate array (FPGA) [69].

Conventional control methods are also limited by low bandwidth actuators. The electrostatic actuation of tunable gratings has shown a higher (50 kHz) bandwidth of operation, which gives more flexibility for designing efficient control algorithm, which can also be used to control an array of interferometers simultaneously.

5.1.2 Harmonic distortion based path stabilization

The harmonic distortion based method is commonly used for active path stabilization of interferometers. The main advantage of this method is that it does not require pre-calibration of the optical curve. The method also determines the non-linearity of a curve over a small region. In active path stabilization, the desired point of operation falls in to a linear region. Hence, using the harmonic distortion based method this point can be tracked. Figure 74 shows the schematic of the harmonic distortion based method implemented on quartz based µSGI. It used a phase sensitive detector (lock-in amplifier) to obtain the second harmonic component of the signal. The amplitude of the second harmonic signal is proportional to the second derivative of the optical curve at the point of operation. The following paragraphs explain the harmonic distortion based method in detail and explains its shortcomings from the µSGI point of view.

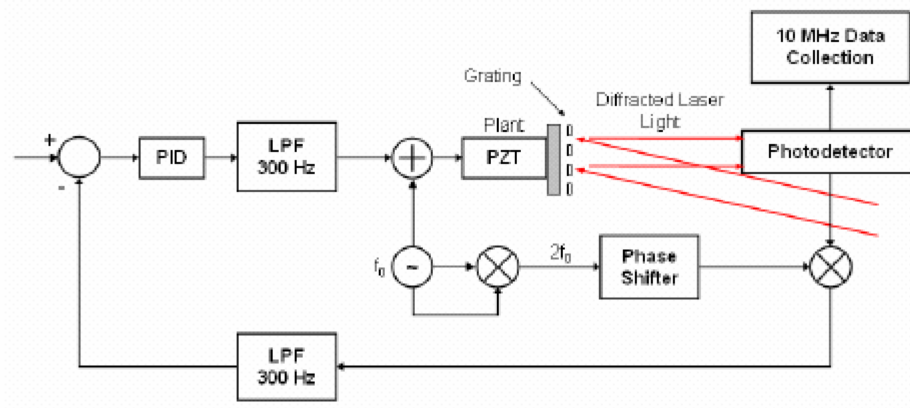

Figure 74 – Schematic of the harmonic distortion based active path stabilization implemented by Kim and Schmittdiel [70]

5.1.2.1 Harmonic distortion based method - concept

In harmonic distortion based error detection method typically the phase of reference signal is oscillated sinusoidally by small amplitude ψ_d using an actuator, typically piezo-electric transducer (PZT). The frequency of oscillations Ω is approximately an order of magnitude higher than the noise bandwidth of interest. If the phase difference between the two interfering beams is ψ, the overall irradiance of the coherent addition of beams I_R and I_S is represented by

$$I = I_R + I_S + 2\sqrt{I_R I_S}\cos\phi \quad \textbf{(5.1)}$$

Where, $\phi = \psi + \psi_d \sin(\Omega t)$ is the phase between the wave fronts of the two beams. ψ_d is typically smaller than the desired range of ψ. Hence,

$$I \cong I_R + I_S + 2\sqrt{I_R I_S}\cos\psi \quad \textbf{(5.2)}$$

It can be seen that this function is most sensitive and linear when $\psi = n\pi + \pi/2$, these are the desired points of operation.

The amplitude of second harmonic can be given by

$$I^{2\Omega} = 4J_2(\psi_d)\sqrt{I_R I_S}\cos\psi\cos(2\Omega t + \varepsilon) \quad \textbf{(5.3)}$$

Where, ε is the phase delay introduced by opto-electronic circuitry and mechanical behavior of the actuator. It can be noted that at the desired point of operation i.e. $\psi = n\pi + \pi/2$, the amplitude of second harmonic, $I^{2\Omega}$ becomes zero and it changes polarity on either sides of the desired point of operation. Hence, $I^{2\Omega}$ can be used to measure the error in ψ, and can be used as error feedback in the control loop.

The main advantage of the harmonic distortion algorithm is that it does not need beforehand optical calibration of the sample for its operation. However, several drawbacks of this method were observed, which are explained in the following paragraphs.

In the harmonic distortion method the reference beam needs to be continuously modulated. This modulation amplitude ψ_d needs to be much smaller than π/2 so that its contribution towards noise is negligible. However, the maximum amplitude of this second harmonic signal $4J_2(\psi_d)\sqrt{I_R I_S}$, being proportional to ψ_d, becomes much smaller than I_S or I_R. This is undesirable because it reduces the signal to noise ratio (SNR) for noise reduction.

The amplitude of the second harmonic is obtained experimentally by phase locking circuitry. However, phase locking gives real and imaginary components of the desired harmonic separately. Some post-processing of the error data is required to obtain the amplitude of the second harmonic. However, if the phase of the phase locking circuitry can be tuned such that it locks to $\cos(2\Omega t + \varepsilon)$, it eliminates one component of the

harmonic. Phase delay ε can be obtained by comparing the first and second harmonics as they are $90°$ phase shifted. This method has been shown to work [53, 59, 66].

The actuators in all these experiments are piezo-electric actuators which were used to modulate and tune either the sample or reference mirror. This vibration is used to generate the required phase modulation for harmonic distortion method to work. However, actuation of sample or the reference mirror may introduce extra noise in the system. From array operation point of view, each of the reference mirrors (or gratings in the case of grating interferometers) needs to be actuated independently. The µSGIs are equipped with tunable gratings for this purpose. The tunable gratings can also be used for modulating the phase of the reference beam [66]. If the tunable gratings are used for phase modulation, there are two problems with this method – 1. Due to non-linearity of the electrostatic actuation, ψ_d varies with changing the bias on the grating membrane. 2. Electrostatic softening of the membrane at higher bias voltages may change the dynamic response of the membrane, which in turn alters the phase delay ε. These problems of non-linearity and changing delay can be solved by calibrating the grating membrane and correcting the actuation signal to compensate non-linearities. However, it is not desired because of it further adds to the complexity of the phase locking method.

Apart from the phase difference ψ, the dynamics of the sample or reference mirror also contribute to the second harmonic signal. Though the ambient vibration noise has a small bandwidth in general, high amplitude low frequency vibrations or drifts give rise to significant higher frequency components. This is caused due to aliasing i.e. if the waveform length used for the phase locking is not long enough to capture a complete wavelength. However, the waveform length also corresponds to the delay in calculating the error signal, which needs to be minimized. This problem can be solved by windowing the sample, however it further adds to the complexity of the system.

5.1.2.2 Digital implementation of the harmonic distortion based method

For better accuracy and flexibility of implementation, this method was implemented digitally using field programmable gate array (FPGA) as shown in Figure 75. To obtain the second harmonic a minimum of 6 point Discrete Fourier Transform (6 pt DFT) needs to be computed. This implementation was shown using an FPGA at low phase modulation frequencies $\Omega \approx 650Hz$ [71]. The 6 pt DFT gives the 1st and 2nd harmonics - of which the 1st harmonic is proportional to the slope of the optical curve (1st derivative) which in turn is proportional to the reflectivity of the sample. The second harmonic is proportional to the error which can be fed to a PID controller to control the position of the tunable grating.

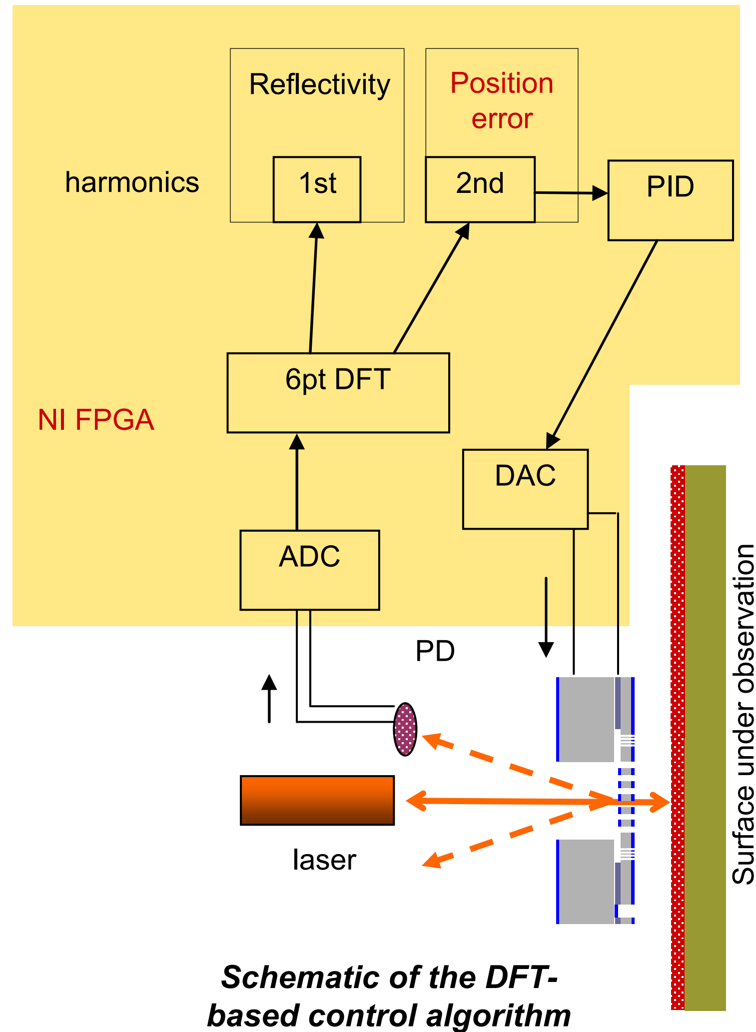

Figure 75 – A 6 point DFT method implementing harmonic distortion based noise reduction algorithm

The results of this implementation are shown in Figure 76. It can be seen that when the controller is off the sensitivity of the controller and the error can be observed as first two harmonic peaks shown by f_1 and f_2. When the controller is on, it can be observed that the sensitivity improves by 12.5dB and the error signal reduces by 35.5dB, hence improving the SNR by up to 48dB. It can also be seen that the first harmonic shows a noise shoulder, when the controller is off, which results from the low frequency noise. When the controller is off the noise shoulder also reduces.

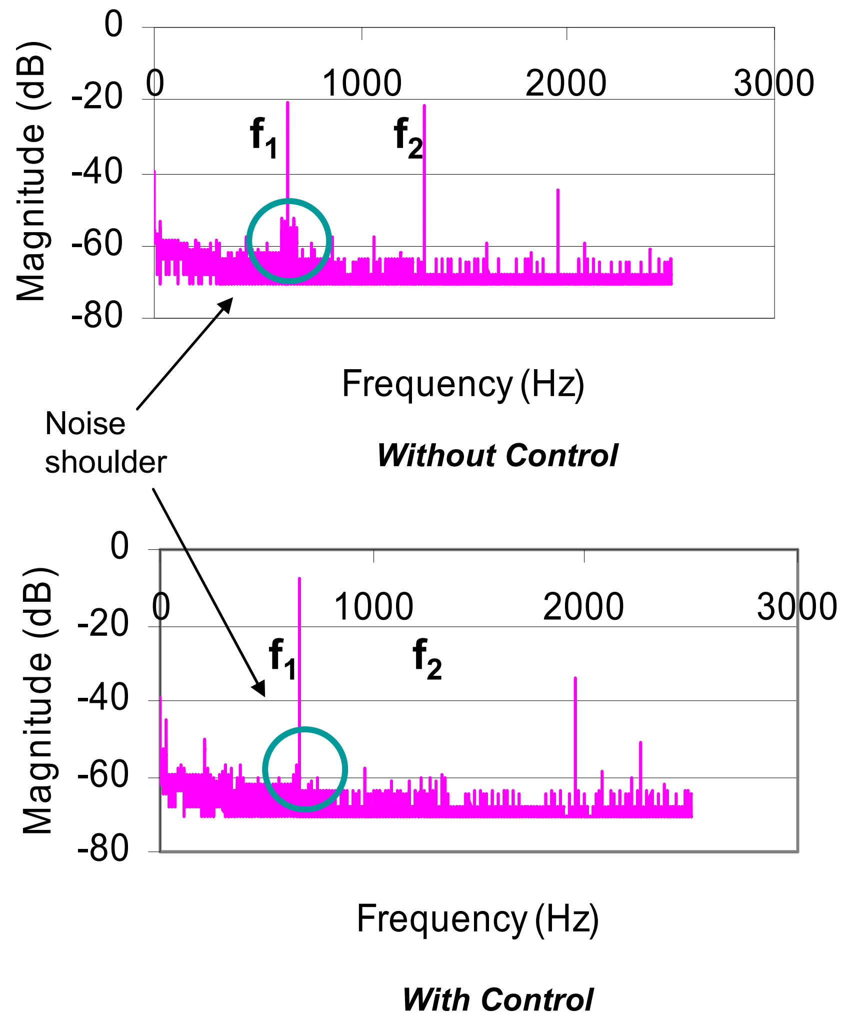

Figure 76 – Reduction of noise using a 6 point DFT algorithm. The second harmonic shown by f_2 is reduced by the controller and the first harmonic f_1 which is proportional to the sensitivity is increased

The frequency of operation for the 6 pt DFT method was very low for reducing ambient vibrations. The reason for the slow operation was found to be the computational intensity of the algorithm. A 6 pt DFT involves the least number of calculations; it has the following multiplication constants for obtaining the second harmonic imaginary (or real) component - sin(0), sin(2pi/3), sin(4pi/3),…, sin(10pi/3) (or cosines of these). The real components involve irrational numbers and some accuracy is sacrificed because of the

fixed point mathematics in FPGA. The multiplication operations make the process computationally intense and it was seen to fail above 1 kHz loop rate. Another limitation was realized with the sine generation signal. Sine look-up table was used to generate sine wave which can not be synchronized beyond 13kHz, because of the tick-times for the sine generation loop and data acquisition need to be integer multiple of each other. A ratio of 3:512 ticks is the minimum achievable ratio for a sine lookup table of 1024 discrete values.

The problem of low speed was resolved by converting the complex number to a real number. Taking advantage of constant phase, only cosine (real) or sine (imaginary) component of the second harmonic can be observed. For maximum sensitivity, the phase of the data acquisition is adjusted so that the other component becomes zero. Now, the magnitude becomes the value of the real or imaginary part and the phase becomes the sign of the number. This makes some of the operations for squaring the real and imaginary components unnecessary.

Another algorithm was developed to tackle this problem. An 8 pt DFT could be used to instead of a 6 pt DFT to reduce the complexities of the computations. A 8 pt DFT involves 8 operations with sin(0), sin(pi/2), sin(pi),…, sin (7pi/2) i.e. 0, 1, 0, -1, 0, 1, 0, -1; These are 4 zeros and 1s and -1s (Figure 77) Hence, it also has only 4 operations because of 4 zeros and there are no irrational multiplicands. The algorithm worked well at 40 kHz. (Here the grating vibrates at 40 kHz and data acquisition is done at 160 kHz. PID output is generated after every cycle i.e. at 40 kHz. This speed is faster than required for reducing noise below 1 kHz. Maximum rate of data acquisition for the FPGA is 200 kHz and synchronization requires the frequency to be 10 kHz multiplied/divided with some power of 2. Hence, 40 kHz is the maximum frequency of vibrations can be achieved with this method.

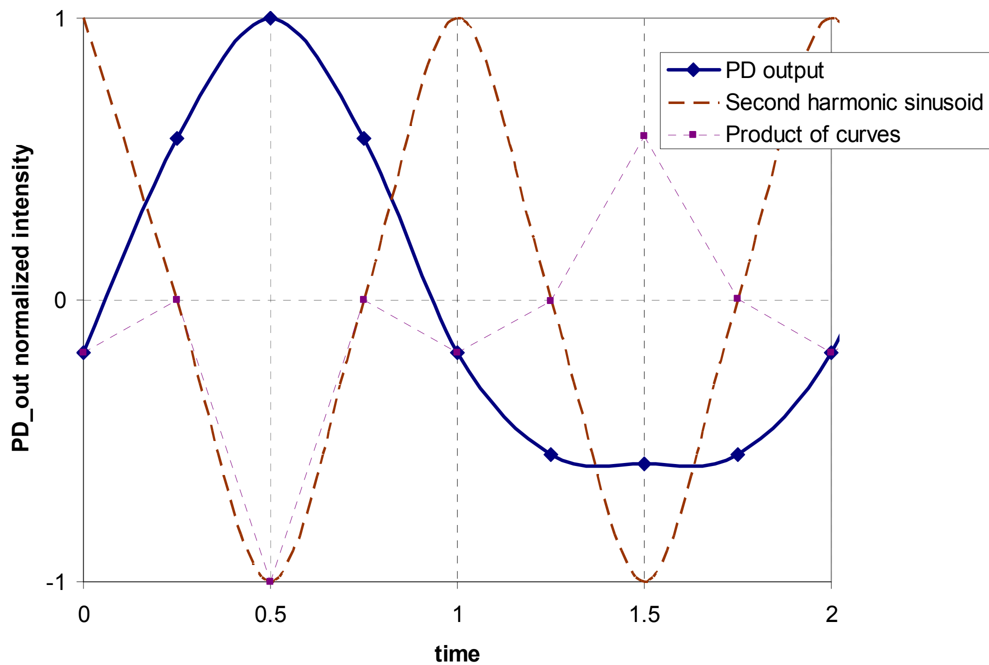

Figure 77 – 8 point DFT for second harmonic. The second harmonic sinusoid shows the multiplication constants. A sample PD output is used to demonstrate the calculation of the amplitude of the second harmonic

Calculating the first harmonic is also as simple as the second. Here we use the 4 pt DFT. The multiplicands become to 0, sin(pi/2),…, sin(3pi/4) i.e. 0, 1, 0, -1. (Figure 78). The points with nonzero multiplicands can be chosen to be the same ones which were used in the second harmonic calculation. Only difference is the signs of the multiplicands. Hence, now the data acquisition can be done at 2xF frequency.

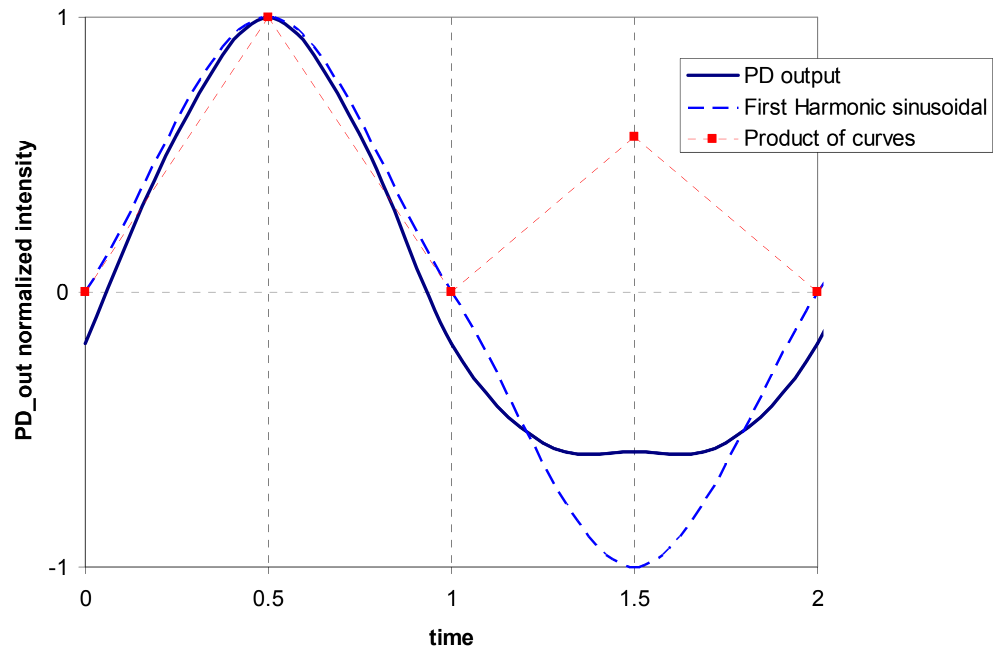

Figure 78 – A 4 pt DFT for the first harmonic. The first harmonic sinusoid shows the multiplication constants. A sample PD output is used to demonstrate the calculation of the amplitude of the first harmonic.

Thus, the harmonic distortion based method has many shortcomings. To overcome some of the problems, the novel recurrent calibration based control algorithm is designed. This algorithm splits the active tuning in 2 steps, in which the first step is used to characterize the optical curve and the second step uses the intensity of a diffraction order as feedback to tune the individual gratings to the respective desired points of operations. This algorithm overcomes the problems in harmonic distortion based methods at the cost of some dead time of frequent calibration steps when it does not take measurements. Next sections explain the recurrent calibration based control algorithm in detail.

5.2 Recurrent calibration based active control - modeling and experiments

5.2.1 μSGI system model

To analyze the behavior of the control system, a system model is built using MATLAB SIMULINK and SISO Tool. The detailed view of this model is shown in Figure 80. For analysis, the system is linearized about the desired point of operation. The input to the system is the high frequency signal and low frequency noise and the output is measured at the summation of inputs and actuator output from the feedback loop.

The photo-detector gain is obtained from the specifications. The controller transfer function (TF) is known from the control algorithm and the grating transfer function is obtained experimentally (see Figure 79). These transfer functions are as follows:

Photo detector: $F(z) = 0.0447$ **(5.4)**

Controller: $C(z) = \dfrac{gain}{z-1} . \dfrac{0.3188}{z-0.6812} . \dfrac{1}{z}$ **(5.5)**

Tunable grating: $A(z) = \dfrac{13.9z + 13.02}{z^2 + 0.314z + 0.84}$ **(5.6)**

(At sampling rate 180 kHz)

The frequency at which the FPGA control loop runs is 180 kHz (see Figure 80) which shows the bandwidth of 90 kHz using the Nyquist criterion). The actuator is linearized using a look-up table to a constant gain transfer function. The second term in the controller transfer function represents a low pass filter (LPF) with cutoff frequency of ~11 kHz. This filter separates the low frequency noise from the high frequency signal. It also serves as the anti-aliasing filter. The delay in the FPGA controller is found to be ~6 μs;

which is very close to 5.556 μs, the sampling time for the controller. This is expected because the control loop frequency is slower than the maximum input and output sampling rates (200 kHz and 1 MHz respectively) for the FPGA. The third term in the controller transfer function represents the delay which is rounded off to 1 sampling period in the FPGA.

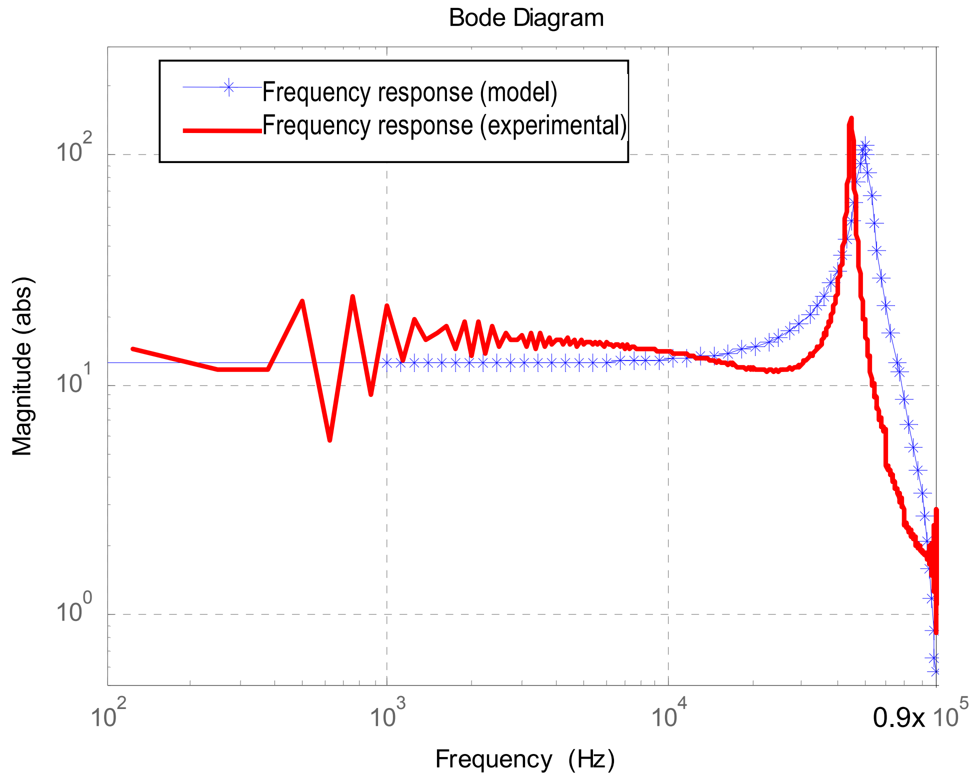

Figure 79 – Frequency response of the tunable grating obtained from the experiments and the second order approximation of the curve in discrete (z) domain at 180 kHz.

The root locus plot of the open loop system is shown in the Figure 81. It can be seen that the closed loop response consists of a high frequency component which is on the root locus starting from the poles due to the low damping resonance of the grating membrane, and a low frequency component which is on the root locus starting from the low pass filter pole. The cutoff frequency of the controller is determined by this low frequency response and can be estimated to be ~6 kHz.

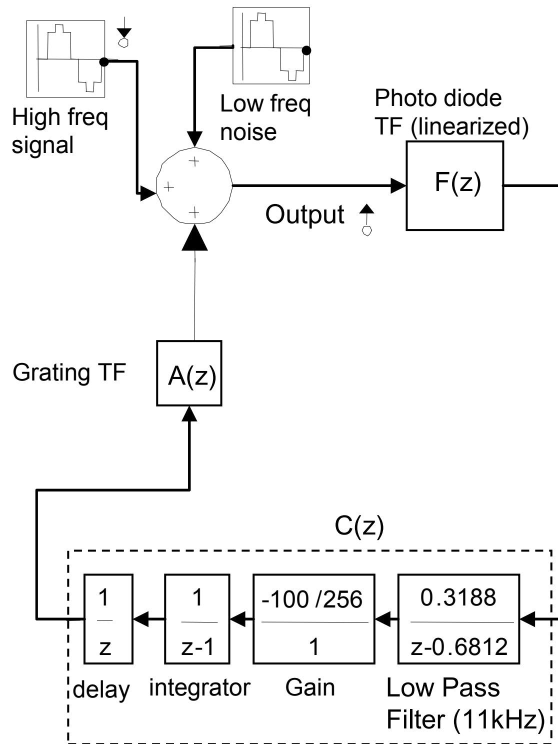

Figure 80: Schematic of the active control of tunable grating system

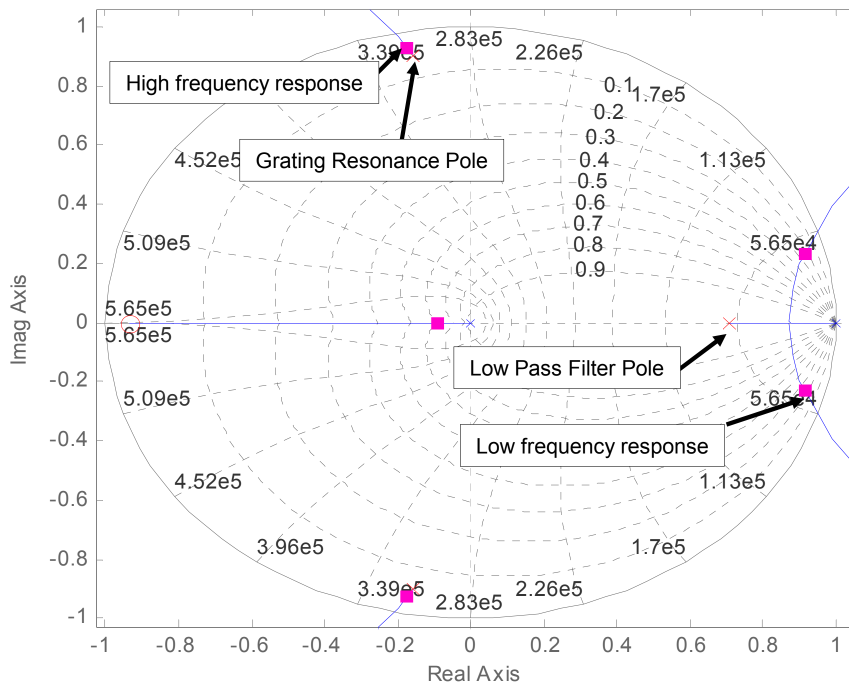

Figure 81: Root-locus plot of the open loop control

The Bode diagram of the controller (see Figure 82) shows the expected noise reduction. It can be seen that the cutoff frequency is around 6.5 kHz which gives about 100 times noise reduction at 100 Hz. As seen in the root locus diagram (Figure 81), the low frequency response shows a peak at the corner frequency (~6.5 kHz) as predicted. There is a trade-off between the corner frequency and the amplitude of this peak. As the controller gain increases the noise reduction cut-off frequency improves, which means better noise reduction at lower frequencies, which is desirable. However, at the same time the lower frequency poles on the root locus go farther from the real axis. This implies a higher amplitude peak at the low frequency as shown in the bode diagram.

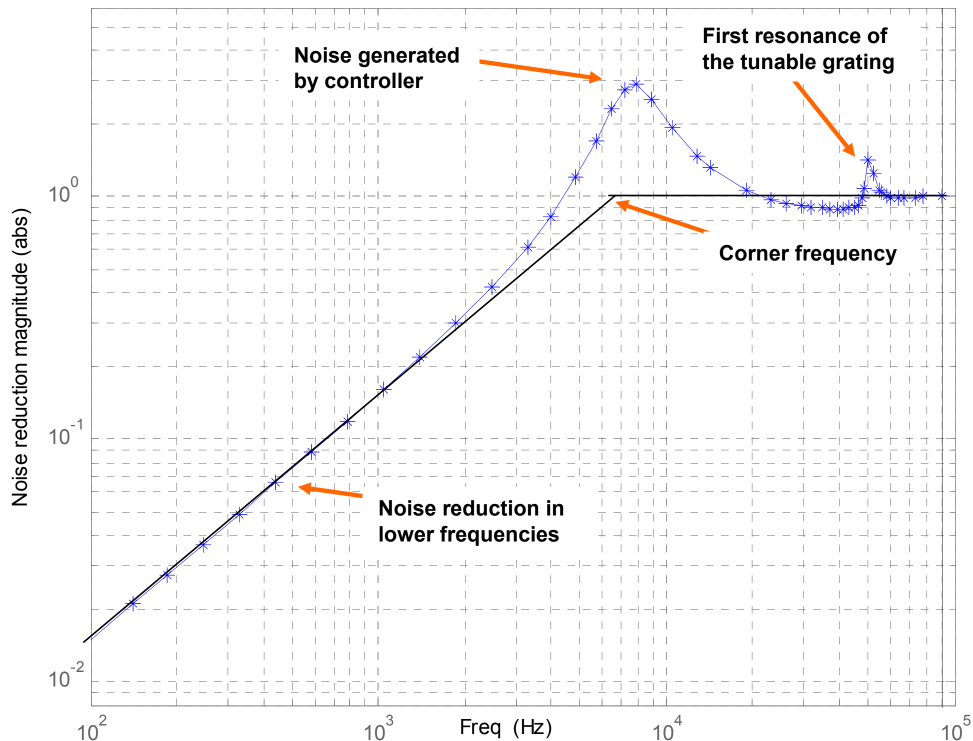

Figure 82 – Bode diagram of the closed loop controller

5.2.2 Experimental setup

To demonstrate the active control and verify the model, a μSGI based parallel interferometry setup shown in Figure 87 was implemented. The setup contains 2 sets of

measurement systems which are used to demonstrate parallel operation. Two samples are placed in front of two μSGIs. Laser light is focused on the gratings and the orders are collected by two different photo-detectors. The output of the photo-detector is used to measure the displacement of the samples and the same output is fed to the FPGA after low pass filtering. National Instruments' NI PXI 7831R FPGA system [72] is used for implementing active control. It provides 8 analog input output channels for parallel implementation and has a 1M gate reconfigurable FPGA board which can be easily programmed with LabVIEW FPGA GUI. This FPGA is used to run multiple parallel loops of control algorithm and generate analog output. The analog output actuates the respective tunable gratings. Two parallel loops of the control algorithm were run simultaneously on the FPGA at ~180 kHz.

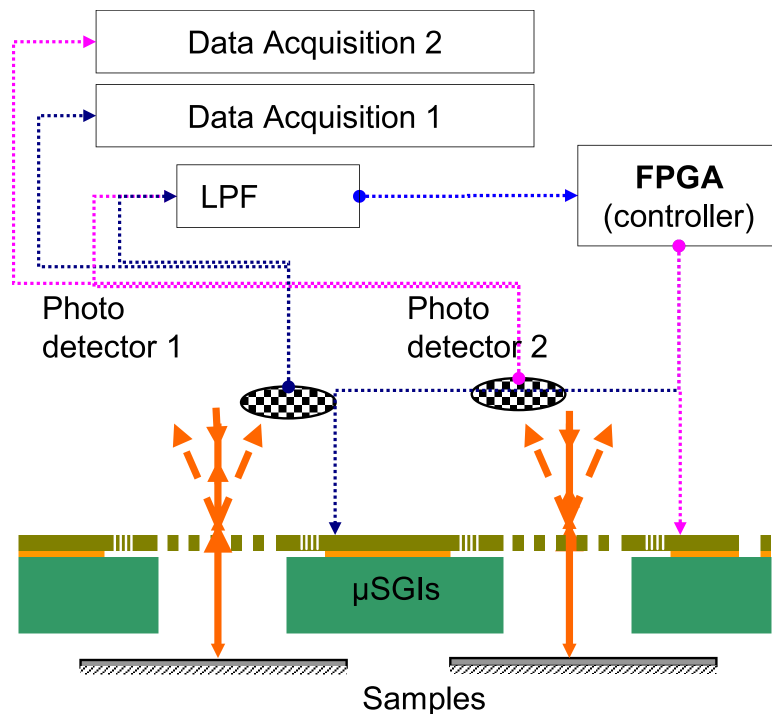

Figure 83 – Experimental setup used for demonstration of the active control scheme

5.3 Comparison of simulation and experimental results

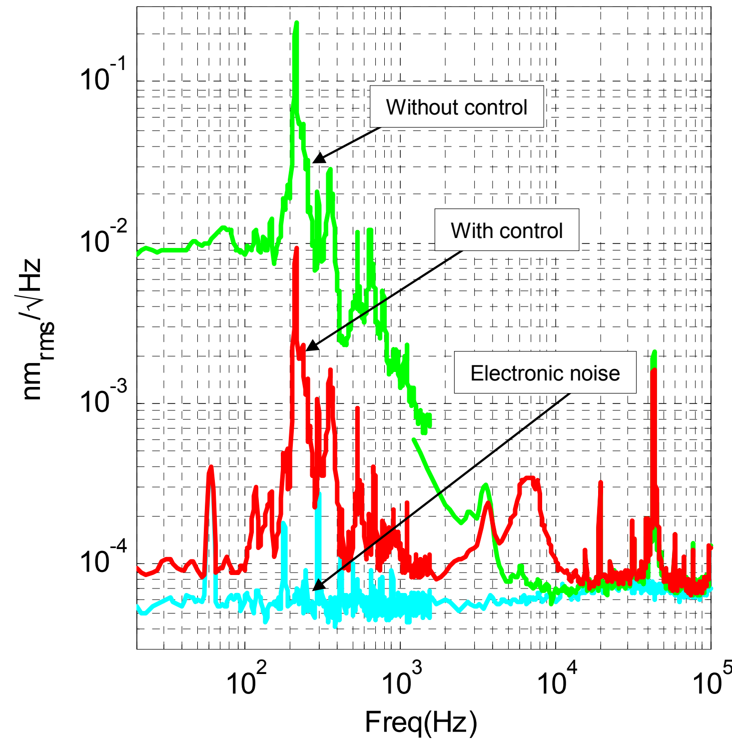

Figure 84 – Experimental results of the active noise reduction.

The performance of the active control of the tunable gratings is tested in ambient noise conditions. A Digital Signal Analyzer (DSA) was used to plot the noise density spectrum of the vibration noise in 100 kHz bandwidth. The voltage noise density spectrum converted to displacement noise is plotted in Figure 84. The electronic noise is observed at approximately $6 \times 10^{-5} nm_{rms}/\sqrt{Hz}$. The noise without active control is observed at frequencies lower than 8 kHz with dominant peaks at in 1 kHz bandwidth. The maximum noise is observed at approximately 215Hz with 0.2 $nm_{rms}/\sqrt{Hz}$. The noise data is acquired multiple times over different bandwidths for better accuracy and plotted on the same graph. The noise data is also acquired when the active control is active and is plotted on the same graph. It shows almost 2 orders of improvement in noise level at 20 Hz. An increase in the noise with active noise control is also observed at 6.5 kHz as predicted by the system model. This noise peak is introduced by the controller as a

result of high control gain. The peak value can be reduced by lowering the control gain which results in lower cut-off frequency. A trade-off between the gain and cut-off frequency is made by limiting the peak to less than 6dB. A base noise level of $1x10^{-4}$ $nm_{rms}/\sqrt{Hz}$ is achieved by the active noise control. The peak at 50 kHz corresponds to the resonance frequency of the tunable grating. A small peak at 60Hz results from the coupling between AC electric source and system circuitry. Other smaller peaks at higher frequencies result from the electronic noise.

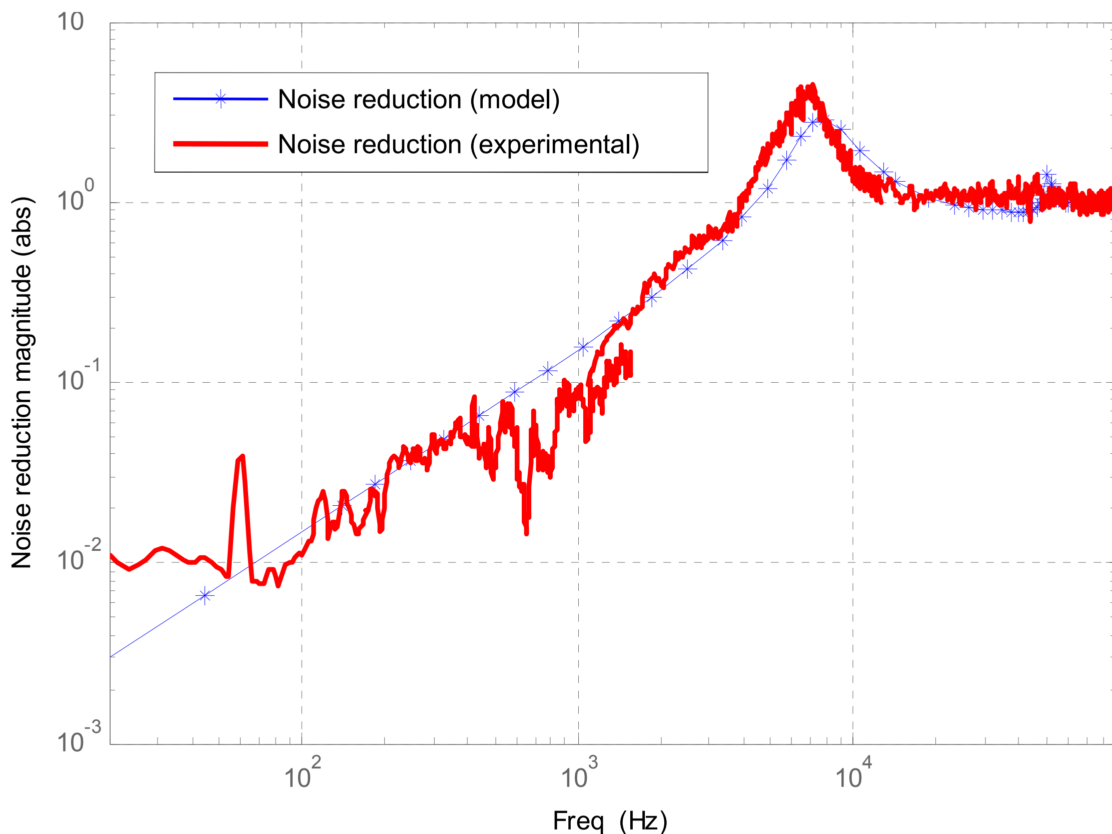

Figure 85 – Noise reduction performance – comparison of simulation and experimental results

Figure 85 compares the active control performance of the FPGA and the model. The simulated noise performance curve shows the bode plot of the closed loop control system. The experimental curve shows the observed noise reduction (ratio of noise without control and with control in Figure 84). The two curves show good agreement.

The cutoff frequency for the active control is observed around 6.5 kHz. Noise reduction performance at frequencies lower than 50Hz becomes constant because of the analog to digital (A/D) conversion resolution of the FPGA i.e. if the noise amplitude is very small and resolution of the controller is not good enough, then the controller cannot see it. For the same reason, the controller performs better than predicted by the model in the noise prone bandwidth (200 Hz to 1 kHz). The peak at 50 Hz corresponds to the AC coupling and could not be manipulated by the controller. With the help of a FPGA, parallel processing of multiple control loops is possible. To demonstrate the parallel implementation of this algorithm a setup as shown in Figure 87 is built. Two flat samples are mounted on two piezoelectric actuators which generate artificial low frequency vibrations. The algorithm is successfully used to actively control both tunable gratings simultaneously. This result has been demonstrated in [71, 73, 74].

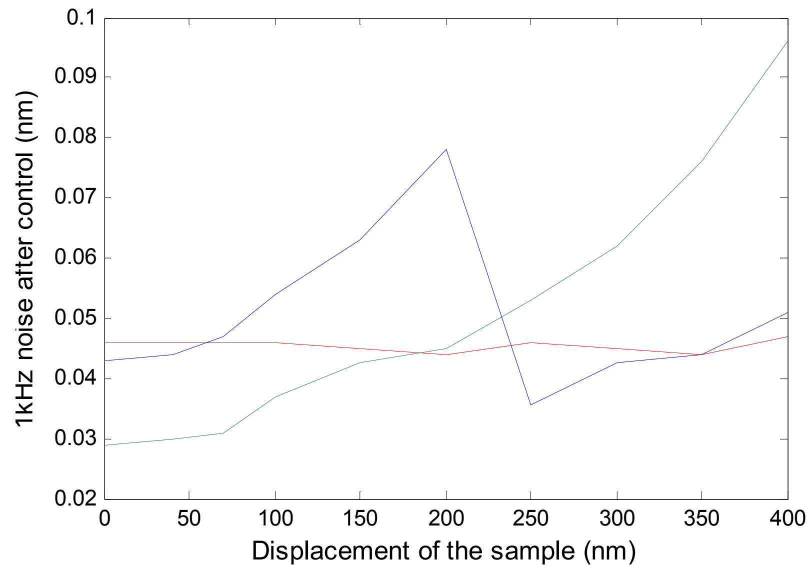

Figure 86 – (A) Blue – without lookup positive gain (B) Green – without lookup negative gain (C) Red – with lookup positive or negative gain.

The simulated effect of look-up table is shown in Figure 86. It can be seen that without the look-up table the noise reduction changes with the grating position; however, the look-up table stabilizes the noise reduction over the complete range of motion.

CHAPTER 6

APPLICATION ORIENTED CONTROLLER DEVELOPMENT AND DEMONSTRATIONS

The µSGI is a miniaturized metrology tool which has vibration noise reduction capability. This enables various different applications ranging from vibration measurement, reflectivity measurement, and frequency response measurement. Additional ability of array operation makes the metrology faster. Scanning of sample surfaces enables mapping their dynamic amplitude and profiles. The control algorithm being a digital algorithm provides easy way for development to achieve different capabilities like long range measurement.

Traditionally many of these tasks would require a different metrology tool; however µSGI offers all the capabilities in a single miniaturized tool. This chapter discusses and demonstrates the development in the control algorithm to achieve several capabilities.

6.1 Parallel operation of µSGI

The µSGI is developed to enable parallel operation of multiple metrology tools to scan a large sample area. The miniaturization of the grating interferometer and optical components enable the parallel operation physically. From active noise control point of view, the digital implementation on the FPGA (Field Programmable Gate Array) proves beneficial. The FPGA enables multiple parallel loops running in parallel, independent of each other. The FPGA used National Instruments (NI) PXI 7831R provides 8 analog input and 8 analog output ports.

6.1.1 Experimental setup

To demonstrate the parallel operation, a 2x1 array of μSGIs is chosen. Two parallel control loops are run on a single FPGA. To acquire data two ports of an oscilloscope are used. The experimental setup, similar to the one shown in Figure 43, is built as shown in Figure 87. Two reflectors are mounted on two different PZTs. These reflectors serve as the surfaces under observation and hence can be used to show the parallel operation of μSGIs. Focused laser beams are passed through the gratings of the μSGIs. For both μSGIs, one of the first orders of interference is captured by the corresponding PDs. The PD outputs are filtered using a low pass filter before it is fed to the FPGA.

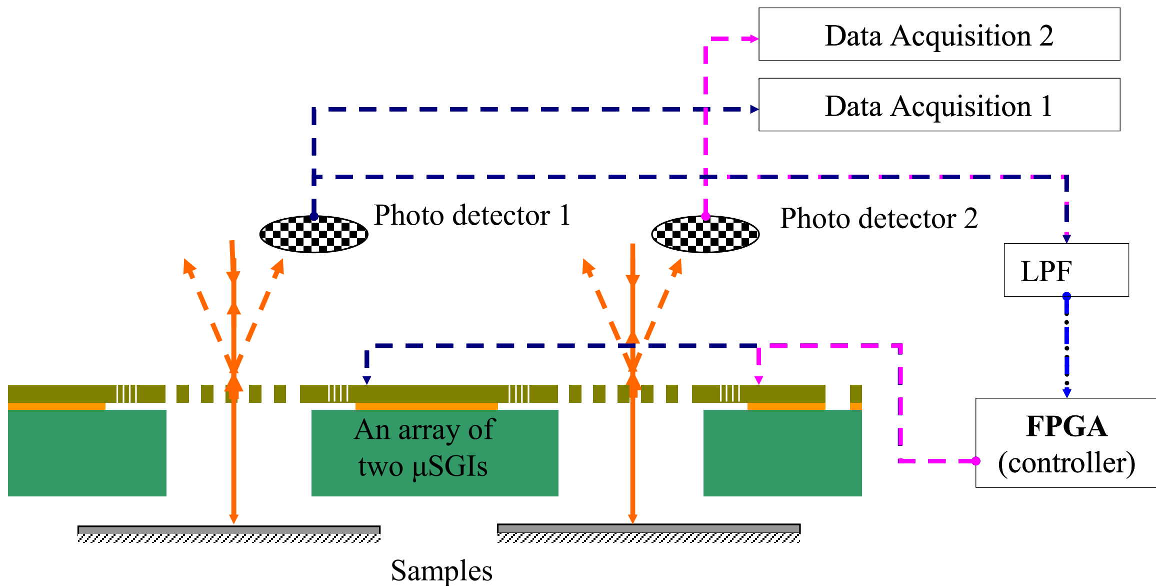

Figure 87 – Experimental setup used for demonstration of the active control scheme

6.1.2 Demonstration of parallel operation

The PZTs are actuated with a low frequency signal (~200Hz,~300Hz which emulates vibration noise) and high frequency signal (~10kHz which emulates the sample motion). The two corresponding gratings are controlled using a multi-channel FPGA. The PD output voltage waveform is acquired using an oscilloscope and is converted in to

displacement using the sensitivity obtained from the control algorithm. The controllers are switched on and off one by one to demonstrate parallel operation. The displacement waveforms are plotted in Figure 88. It can be seen that without the controller the waveforms are not at the highest sensitivity positions and the oscillations due to the low frequency noise are very high. The controller reduces the lower frequency signal by approximately 2 orders of magnitude. Two controllers can be seen operating independent of each other which demonstrates the parallel operation.

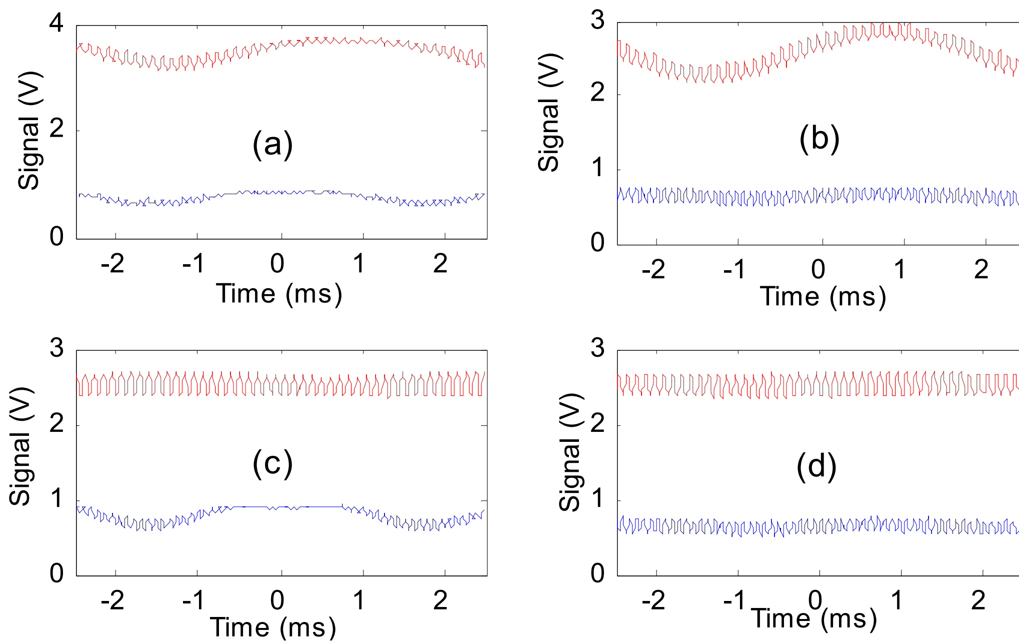

Figure 88 - Parallel active noise reduction using two μSGIs on the same chip. (μSGI 1 - blue, μSGI 2 – pink) (a) Both controllers off (b) Controller 1 on, controller 2 off (c) Controller 1 off, controller 2 on (d) Both controllers on.

The signal is obtained by filtering the data with a high pass filter (HPF). This filtered data is converted in to displacements and the dataset for sample 1 is shown in Figure 89. It can be seen that without controller the high frequency vibration amplitude gets affected by the low frequency noise. However, with the active control the amplitude of high frequency vibrations signal remains constant. This demonstration shows nm-scale

dynamic measurement capability of the μSGIs with active noise reduction. (These results are published in [75].)

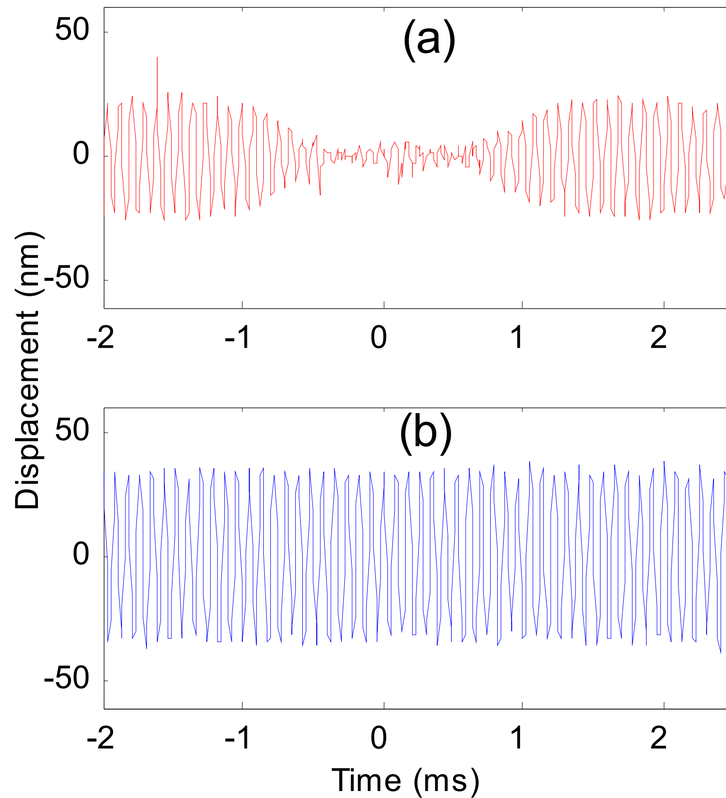

Figure 89 – High-pass filtered data. (a) PD1 output with controller off (b) PD1 output with controller 1 on.

6.2 Long range measurement implementation

Laser interferometric metrology has been well known for its non-contact, high resolution, high bandwidth measurements. In its simplest form, a phase sensitive interferometer offers nm-level resolution over half a wavelength (316nm for He-Ne laser) of unambiguous range. With growing quality control and efforts towards miniaturization, this resolution and range does not satisfy the needs of many different applications like precision machining, Atomic Force Microscopy, biomedical applications and MEMS like

micromirrors, which require not only very high precision but also a longer range of operation.

6.2.1 Methods for multi-wavelength displacement measurements

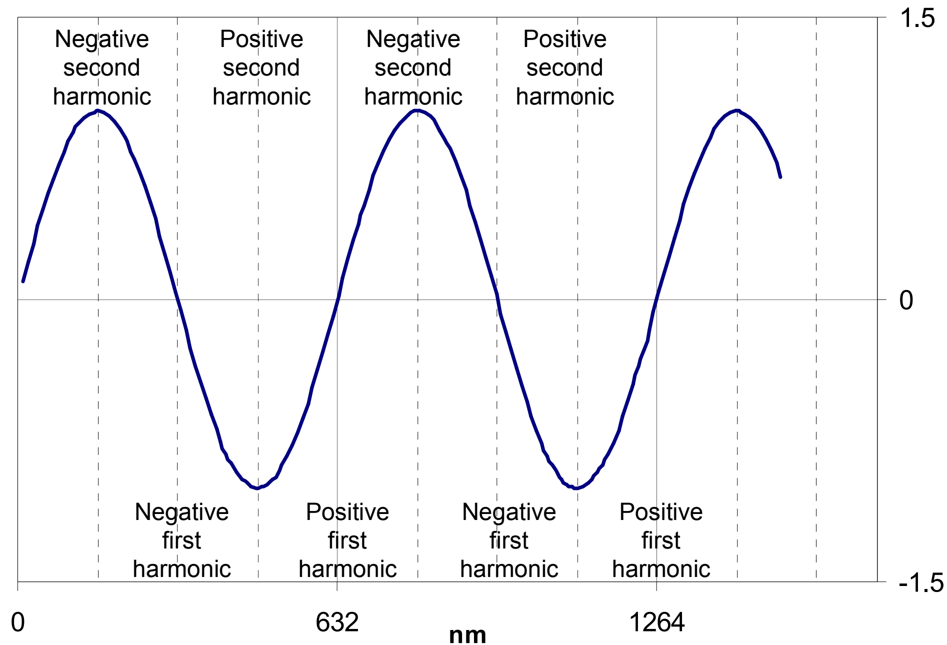

Figure 90 – The quadrature output using harmonic distortion method

The limitation of the range arises from the periodic nature of the response curve. One measurement reading corresponds to several periodic distances; which is ambiguous. Several methods are also implemented to increase the range of operation of the laser interferometers. These include using heterodyne interferometers which use multiple-wavelength source to eliminate the ambiguity, which extend the range to the synthetic wavelength of the wavelengths. This range is extended further by using the optical phase information [76]. Another method uses tunable laser in heterodyne interferometry for absolute distance measurement [77]. In single wavelength laser interferometers, the ambiguity can be reduced by using the effect of coherence length of the laser [78]. Several methods implement different techniques to generate a quadrature signal from the interferometric response [79, 80]. Figure 90 shows a way to obtain quadrature output

using the harmonic distortion based method. Another method obtains a quadrature signal using phase-shifted double grating [81]. However, it is challenging to obtain a very high resolution and an extended range simultaneously.

6.2.2 Long range recurrent calibration based algorithm

The recurrent calibration based control enables operation at the most sensitive point on the optical curve. This enables high precision (sub-pm resolution) measurement of high frequency (>10 kHz) low amplitude (<10nm) vibrations simultaneously. This algorithm is modified as shown in Figure 91. The displacement measurement is obtained with three different ranges of motions

1) First of these measurements is the high precision high frequency dynamic motion obtained directly from filtering the photo-detector signal through a high pass filter (HPF). The filtered signal is converted to displacements using the sensitivity of the interferometric measurement at the desired point of operation. This is the default measurement from the recurrent calibration method.

2) The tunable grating follows the sample motion in lower bandwidth. Hence, the tunable grating motion gives a parameter to measure the sample motion. The grating motion is governed by the controller output and it can be used for measurement for a pre-calibrated tunable grating. The controller output before look-up table is linear and is proportional to the grating displacement; hence it is used for easy conversion to distances.

3) When the tunable grating reaches one of its range-limits, the gain reversal algorithm moves it backwards to the next feasible desired point of operation. The consecutive desired points of operation are quarter wavelength (λ/4 or half a fringe) apart. These

jumps are counted by keeping track of the gain reversal events with their direction. Each jump being λ/4 distance, gives the third set of measurements.

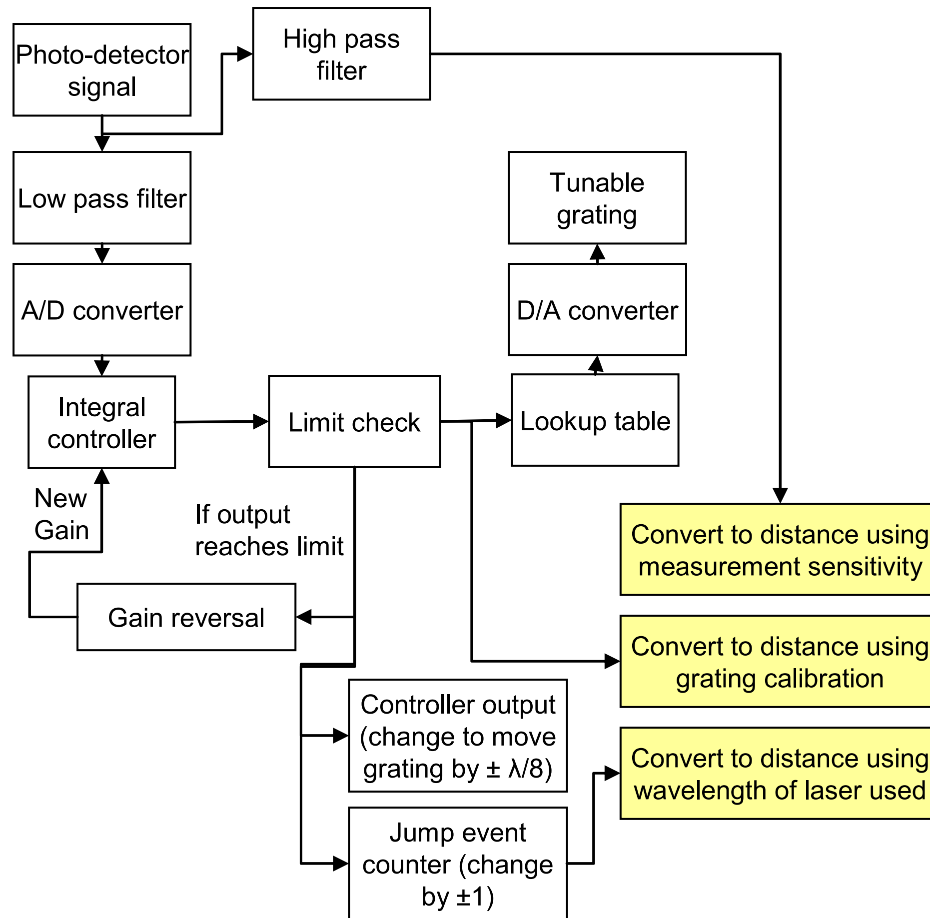

Figure 91 – Long range detection algorithm – The displacement measurement is done at three different resolutions 1) High frequency (>6.5kHz) high resolution (<0.1 pm/√Hz) data acquisition using path stabilized μSGI 2) Low frequency (<6.5kHz) low resolution (nm level) data acquisition using grating motion, has limited range (λ/4) 3) Low frequency (<6.5kHz) low resolution (λ/4) data acquisition using grating jump count

The total sample displacement is the sum of these three displacements. The high and low pass filters (LPF) are designed to have same cut-off frequencies and same order to make sure that no motion measurement is lost. This ensures that the signal which does

not pass the HPF is measured by the controller and vice versa. At the gain reversal event the grating is forced to move by a λ/4 distance to minimize the time of jump.

6.2.3 Experimental setup

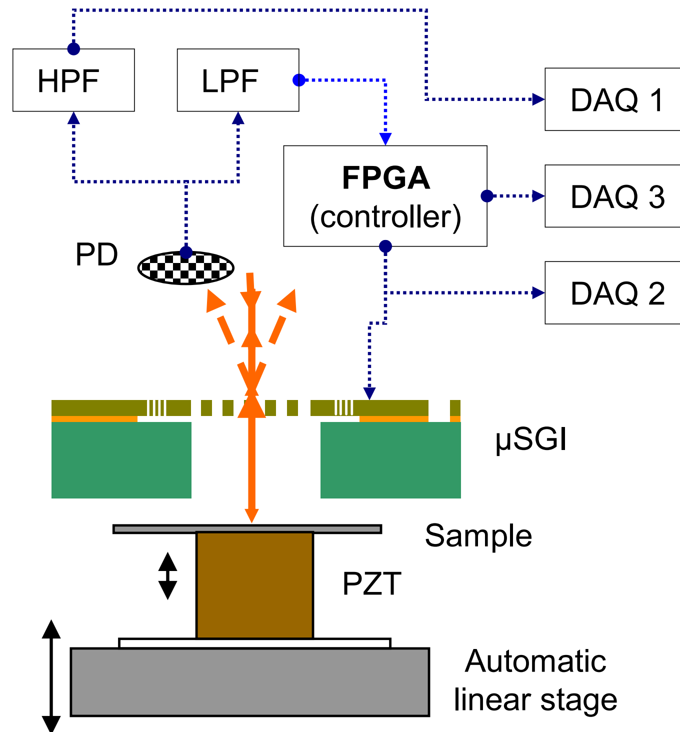

Figure 92 – Experimental setup to show long range high resolution operation of μSGI

To verify the extended range recurrent calibration algorithm an experimental setup is built as shown in Figure 92. The sample is placed on a piezo-electric transducer (PZT), which in turn is placed on a motorized linear stage. The photo-detector output is passed through filters and is fed to the controller and data acquisition systems (DAQ) as explained in the algorithm. The PZT generates a motion which is superposition of two sinusoidal motions – 1) 100Hz, 100nm; 2) 18 kHz, 1.25nm. The motorized stage moves the sample by longer distances with a constant velocity 2μm/s.

6.2.4 Demonstration of long range measurement operation

The high frequency high resolution data acquisition is used to measure the high frequency signal applied to the PZT. Figure 93 shows the acquired data over a 0.5ms interval. A 2.5nm signal is well reconstructed by the data acquired from the µSGI.

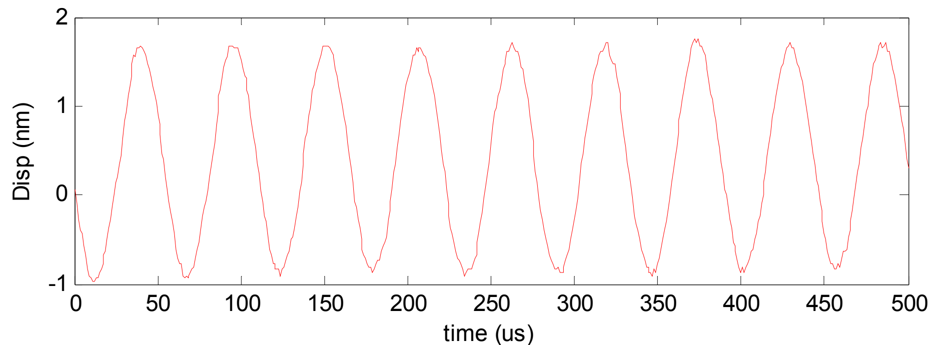

Figure 93 – High frequency low amplitude vibration obtained from high resolution data acquisition

Figure 94 shows the low frequency vibrations of the sample tracked by recording the grating motion over time. It can be seen that the grating follows the sinusoidal motion and the linear motion. Whenever the grating reaches its limits a jump event can be observed. Each jump event brings the grating to the next desired point of operation which is at a λ/4 distance.

Figure 95 shows the displacement output corresponding to the jump events. Each jump event corresponds to a λ/4 displacement in the direction of the jump. It can be seen that the jump events roughly follow the low frequency vibrations of the sample and also the linear motion of the sample. Thus a sample motion over a long range can be measured.

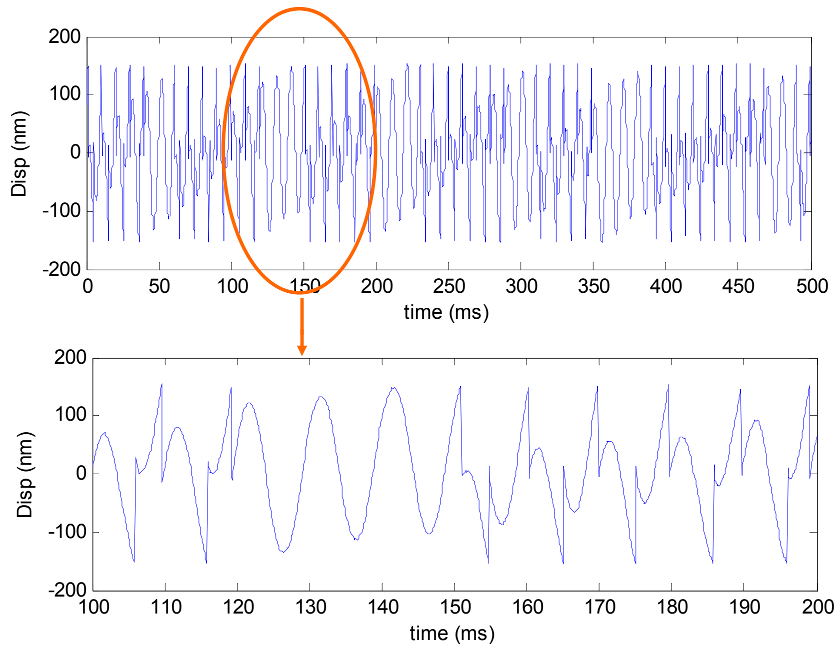

Figure 94 – Low frequency vibrations obtained from the surface tracking of the grating (over 500ms and zoomed in over 100ms)

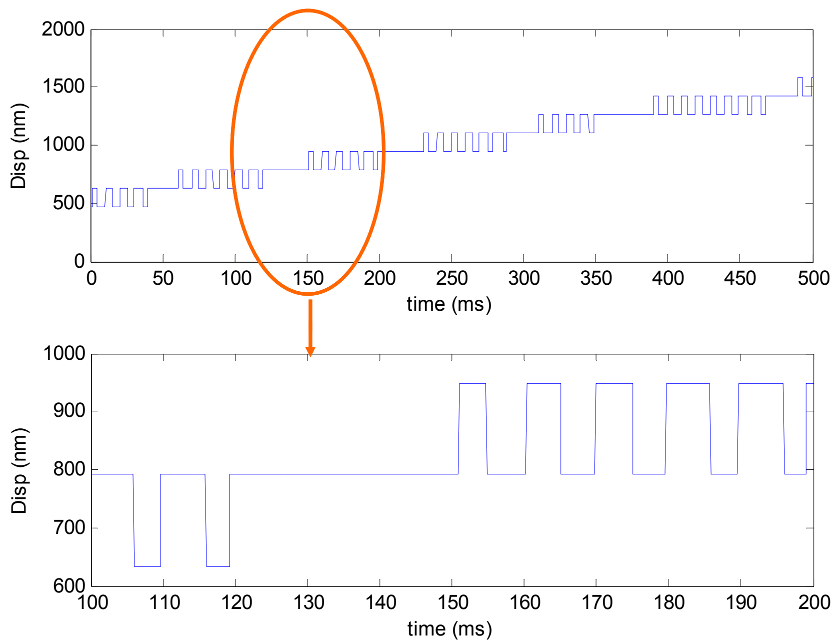

Figure 95 – Long range motion obtained from the grating jump counting (over 500ms and zoomed in over 100ms)

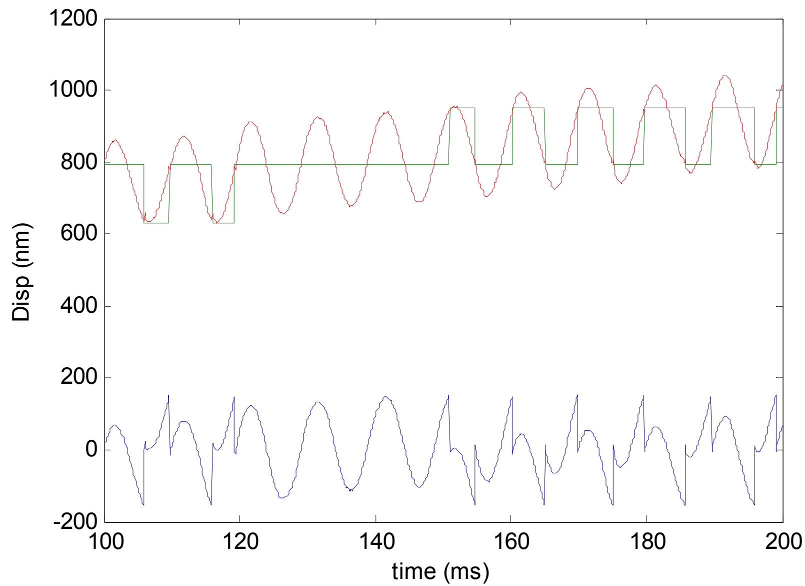

Figure 96 – Addition of low frequency vibration measurement (blue) and jump counting measurements (green) gives total displacement measurement (red)

The total displacement is the sum of all three displacements obtained from the three measurements. The low frequency measurements can be added to reconstruct the low frequency motion. Figure 96 shows the addition of the two measurements generating the total displacement. The total displacement observed over a 0.5s time is shown in Figure 97. It can be seen that the total displacement is well reconstructed over 1μm displacement.

During each jump event the tunable grating travels over a peak or valley of the optical curve and stabilizes at the next feasible desired point of operation. The tunable grating has a low damping ratio which allows fast operation however it also causes long settling time. During the grating motion between two desired points of operations and until it is stabilized at the next desired point of operation the μSGI can not be used for measuring high frequency high resolution displacement. This is the dead time corresponding to the jump. Figure 98 shows a high frequency high resolution data obtained during the jump

event. It can be seen that the grating takes approximately 250µs to stabilize. During this time the high frequency high resolution data gets corrupted by the displacement data generated by the tunable grating itself. Depending on the frequency of the jump events the percent data loss varies.

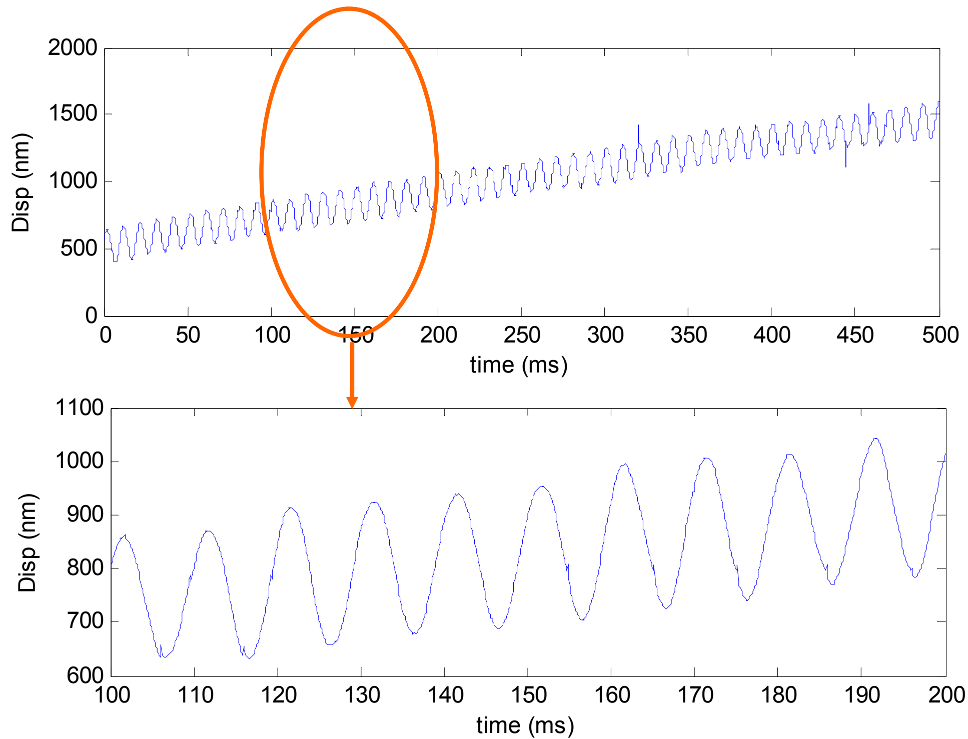

Figure 97 – Total displacement obtained from addition (over 500ms and zoomed in over 100ms)

In conclusion, the modified recurrent calibration based algorithm overcomes the range limitations in high resolution displacement metrology. The µSGI demonstrates its long range high resolution measurement capability by measuring the displacements at three different resolutions.

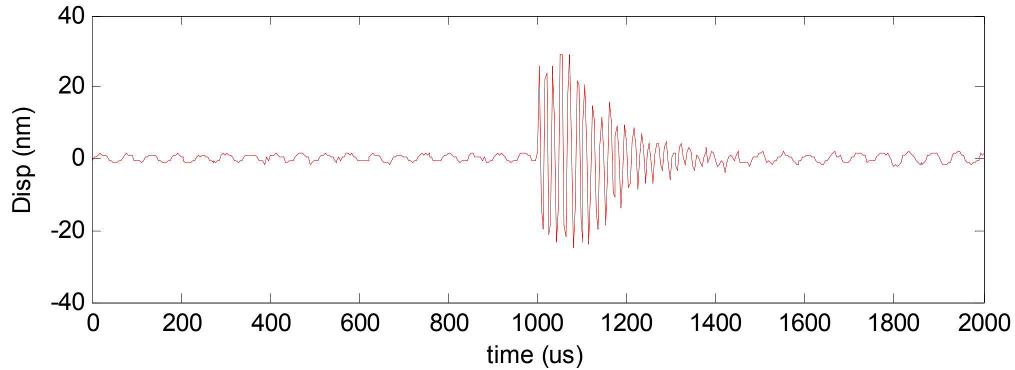

Figure 98 – Grating jump event stabilization time - during this time true high resolution measurement can not be obtained

6.3 Scanning interferometry with µSGI (Case studies)

6.3.1 Dynamic metrology of rectangular actuable membrane with µSGI

6.3.1.1 Rectangular actuable membrane

The sample membrane is an 80µm X 80µm gold membrane fabricated on a quartz substrate. This type of structure can be used as a high bandwidth actuator for many applications like Force Sensing Integrated Tip and Active Readout Structure (FIRAT) [82] or as a Radio frequency RF-switch. The membrane is shown in Figure 99 is fabricated for its use in a FIRAT structure, as a rectangular clamped-clamped beam.

The metal electrode and membrane structures have good reflectivity; however the quartz substrate is mostly transparent to the visible light. The µSGI also enables to map the reflectivity of the sample surface, which can be utilized to realize the static shape of the structures. The membrane is actuated by electrostatic forces at 57.4 kHz 7V peak to peak amplitude and 13.5V bias voltage. The dynamic vibration profile of the membrane is also obtained by scanning the membrane using µSGI. The following section demonstrates the scanning application.

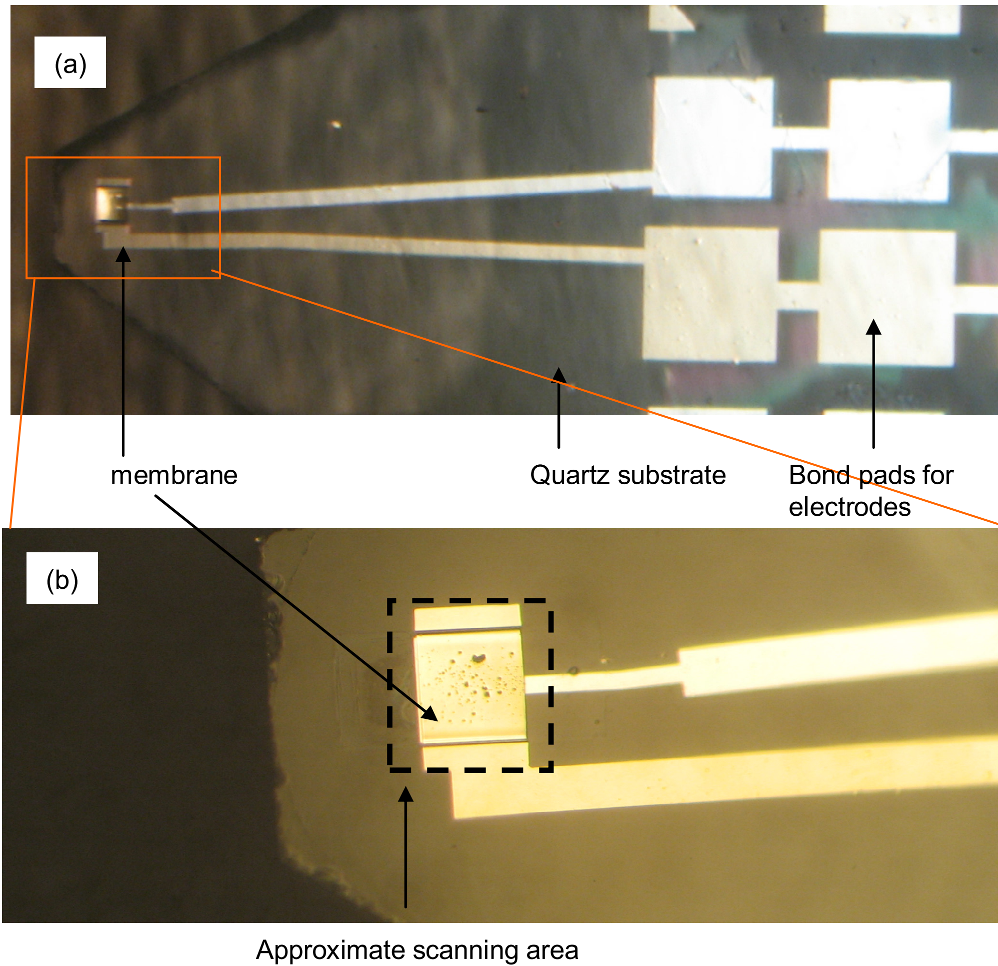

Figure 99 – Rectangular actuable membrane used as sample

6.3.1.2 Measured reflectivity map of the membrane structure

A raster scan of the membrane structure was performed as shown in Figure 100. 80 lines with 80 points per line were scanned with a total of 6400 pixels. Each pixel is 1.5µm X 1.5µm in size. The raster scan consists of lines in the Y direction as shown in Figure 100. Figure 100 shows a schematic scan on an image obtained by a microscope and it does not represent the image scanned exactly.

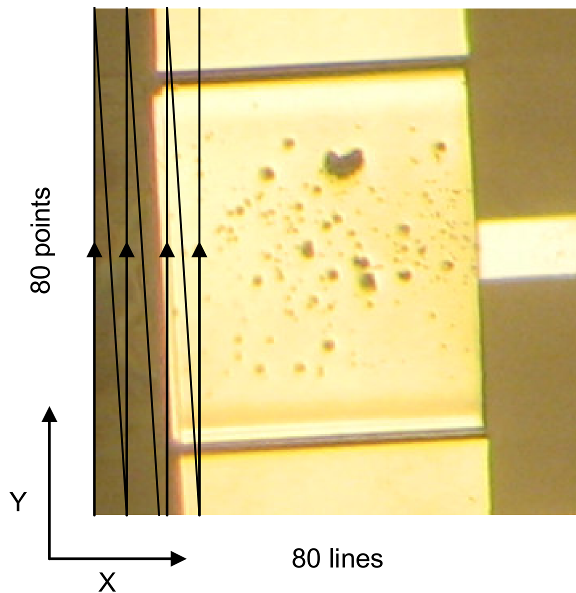

Figure 100 – Raster scan of the membrane structure

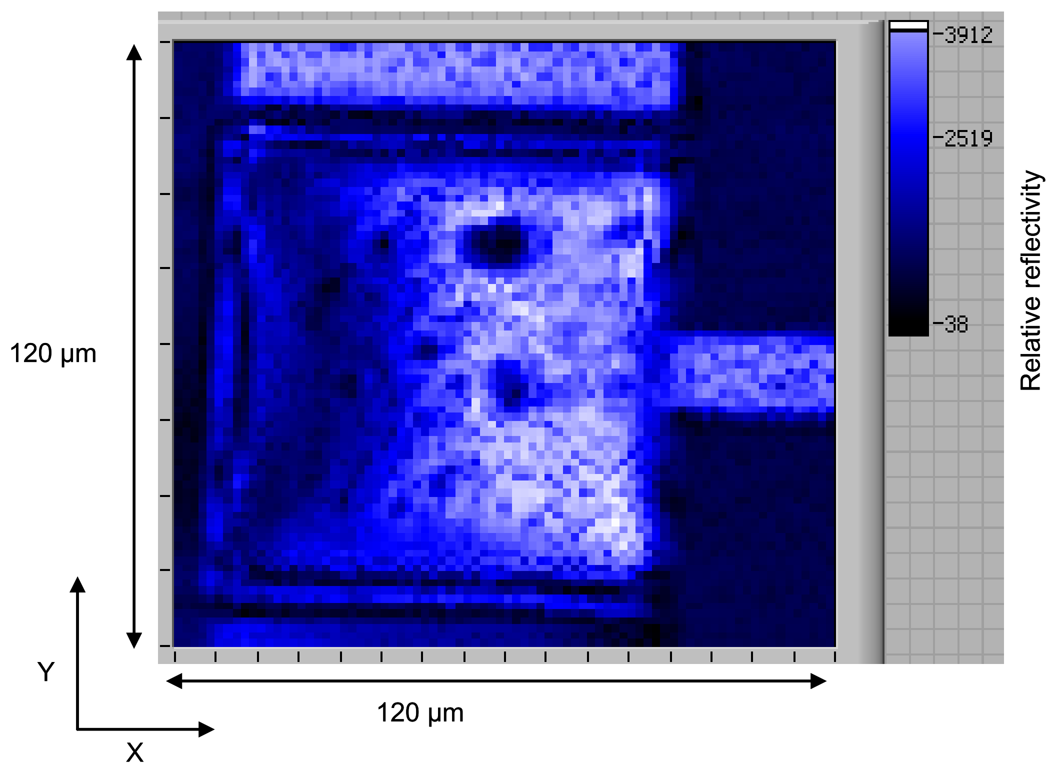

Figure 101 – A reflectivity profile of the sample obtained by µSGI

Figure 101 shows the reflectivity profile of the sample. The metal structures on the quartz substrate can be distinctly observed. The reflectivity of the membrane over varies

over its area with the area towards right being more reflective than the area towards left. This may be due fabrication related issues. The top clamped part of the membrane shows uniform reflectivity from right to left which confirms that the reflectivity change is not an outcome of the μSGI setup.

6.3.1.3 Vibration profile measurement

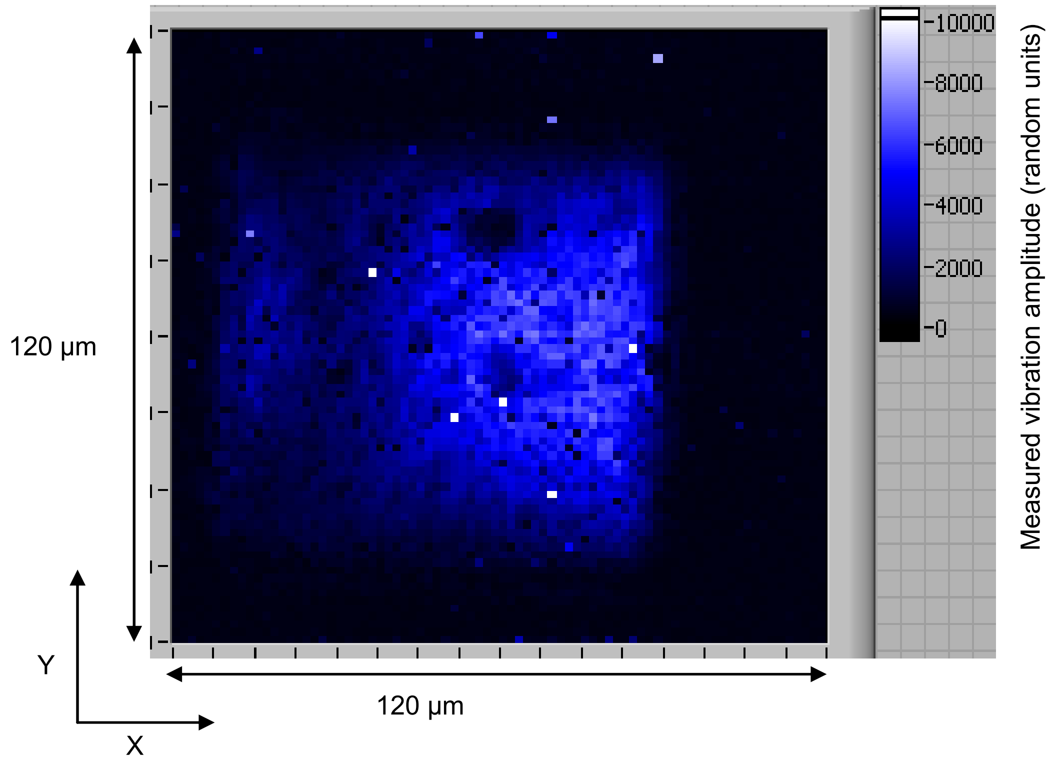

Figure 102 – Vibration amplitude map directly measured from photo-detector signal

The amplitude of the optical signal measured at each pixel is also mapped and is shown in Figure 102. It can be seen that only the actuable membrane portion of the sample surface shows vibrations. The amplitude also seems to be proportional to the reflectivities at the corresponding pixels as shown in Figure 101. This is expected because the sensitivity of the optical signal is proportional to the reflectivity of the sample.

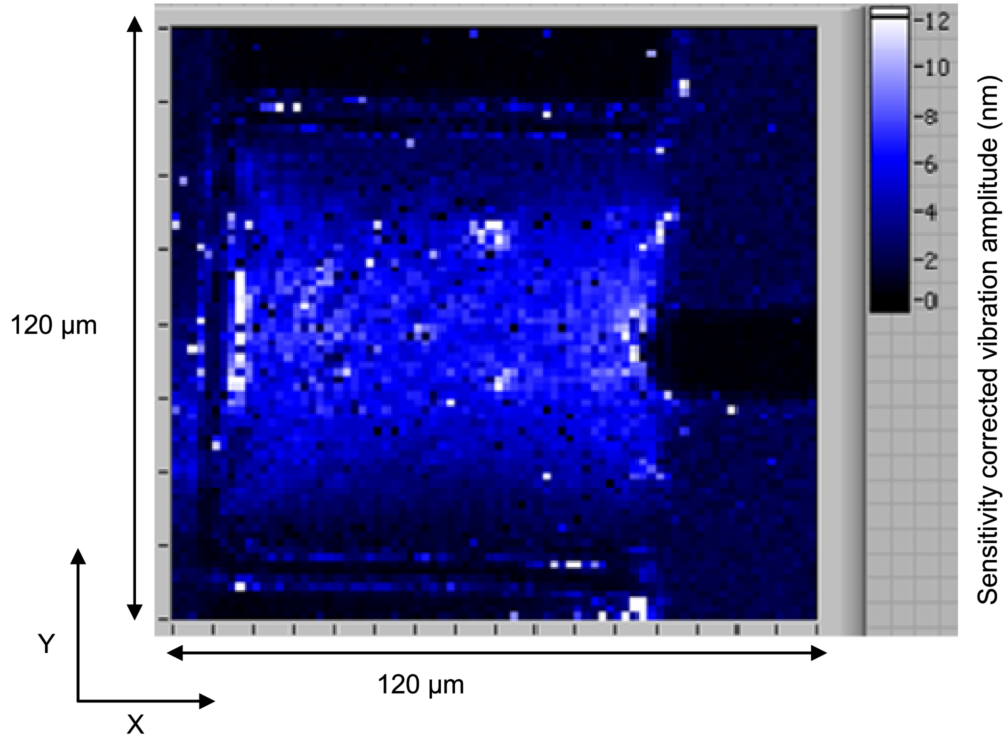

Figure 103 – Vibration amplitude map of the membrane

The peak to peak amplitude (V_{pp}) of the optical curve, which is proportional to the reflectivity, can be used to determine the sensitivities of the measurement at each point. The sensitivity can be given by

$$Sensitivity = \frac{\lambda}{2\pi V_{pp}} \quad \textbf{(6.1)}$$

Using the sensitivity the real vibration amplitudes can be found out by multiplying the sensitivity with the vibration signal obtained from photo-detector. The vibration amplitude map of the FIRAT is shown in Figure 103. It can be seen that the vibration amplitudes are more uniform and show the first mode of vibration. The first mode of vibration is identified by peak vibration amplitude at the center and it dies down to zero towards the clamped edges.

It can be seen that the fixed metal areas where reflectivity is high the vibration amplitude is zero. However, on the quartz substrate where the reflectivity is not so good, uniform low vibration amplitude is observed. This is due to the fact that the sensitivity has V_{pp} term in the denominator. Hence, low V_{pp} gives rise to high sensitivity which enhances the noise in the system. This noise can be filtered by filtering out data with low V_{pp}. However, the slight effect of reflectivity helps understand the orientation of the device better. Hence, such filtering is not done here. (Next case uses such filtering).

6.3.2 Dynamic metrology of cantilever probe

The FIRAT membrane tested is overly damped and does not show even first resonance peak. Second and higher modes are good to test the system better as the phase of vibrations change over the sample surface. Hence a cantilever probe used in Scanning Probe Microscopy is used. This particular probe is manufactured by Veeco Probes and it is classified as a Nitride probe (NP-20).

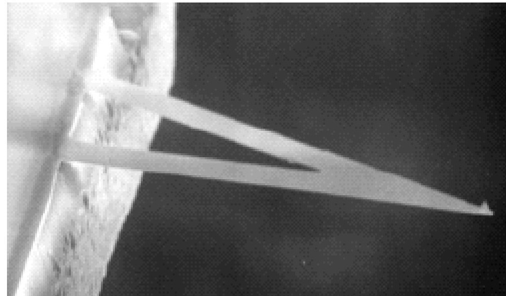

Figure 104 – Veeco NP-20 silicon nitride probe [83]

A picture of this probe is shown in Figure 104. It can be seen that the probe is triangular in shape with a pyramidal probe at its tip. This cantilever is made of silicon nitride and is coated with thin gold layer.

This cantilever is mounted on a piezoelectric transducer stage and the stage is vibrated to actuate the cantilever. The cantilever shows a resonance peak at 91.4 kHz and another peak at 244 kHz. The cantilever was scanned by the µSGI for both these cases. The reflectivity, vibration amplitudes and phase data is collected.

6.3.2.1 Resonance mode 2

The reflectivity image (Figure 105) shows uniform reflectivity over the cantilever and almost zero where there is no cantilever surface as expected.

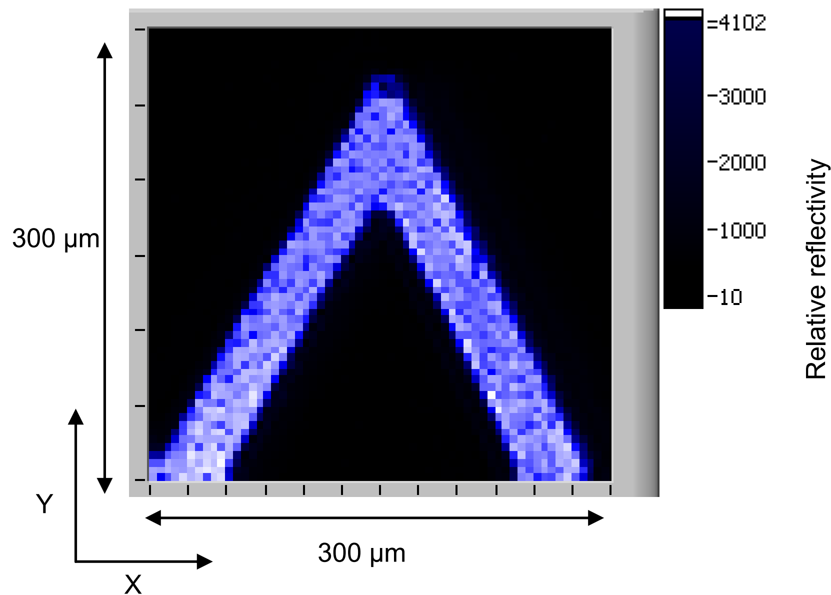

Figure 105 – Reflectivity image of the cantilever

The sensitivity corrected vibration amplitude image is shown in Figure 106 which clearly shows a region on the cantilever which has nearly zero amplitude. This implies that the cantilever is vibrating in its second resonance mode and the zero amplitude regions correspond to the node. (Note that the base of this cantilever is not fixed and it is moving with the PZT stage. Hence, the node locations are shifted from the ideal case)

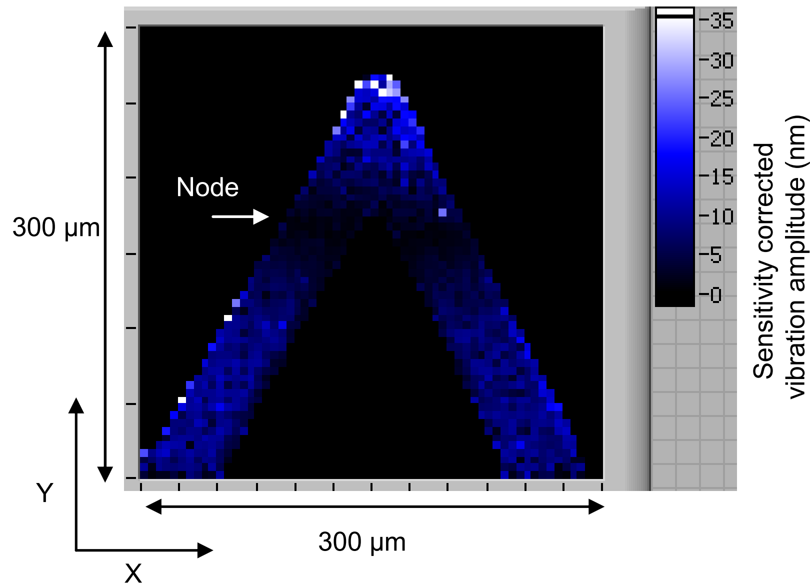

Figure 106 – Sensitivity corrected vibration amplitudes in second mode

The phase of vibration at the node is expected to undergo a change of 180°. The phase of the vibration is also obtained from the µSGI and is plotted in Figure 107. It can be seen that there is a distinct change in phase at the node location.

Obtaining phase information using µSGI is tricky because the gain reversal algorithm a phase change of 180°. Also, the regions where the reflectivity is zero (i.e. where there is no cantilever surface) generate some random phase information. These regions can not be easily filtered as the phase wrapping brings all phases inside the 0-360° range. Plotting phases is also tricky as 0° and 359° look like two extremes on the plot but they are almost equal. To solve these problems, the following steps are done. The generated phase data has two prominent phases which are 180° apart at the reflective regions. These phases are identified and are shifted to ~90° and ~-90° by adding some phase bias. Gain reversal correction is then applied to the phase data, changes the phase by 180°. The zero reflectivity phase data is filtered and is converted to zero. All the phase data is then wrapped with modulo 360°. The prominent phase values in the final data is

0° for non-reflective surface, 90° for in-phase surface and 270° for out-of-phase surface. This can be easily plotted.

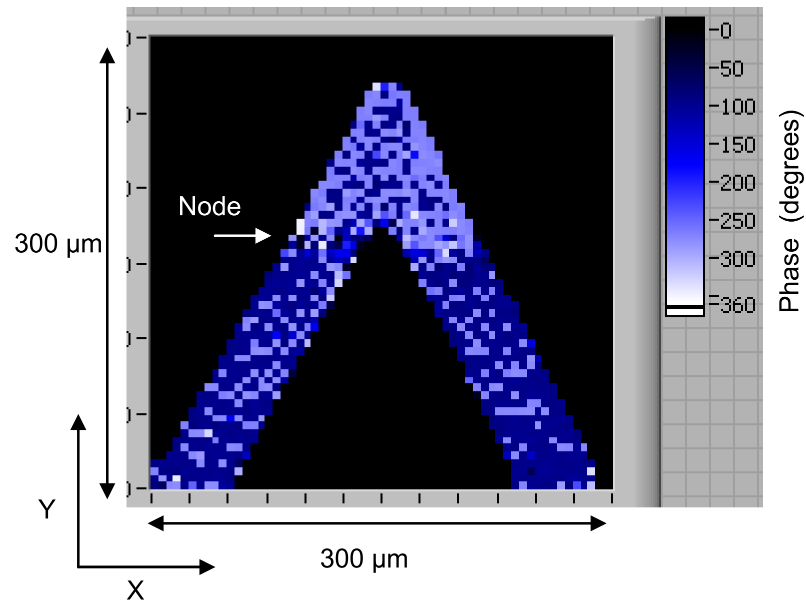

Figure 107 – Phase map of the cantilever showing phase change at node in second mode

6.3.2.2 Resonance mode 3

To verify the metrology operation the experiment is conducted again by actuating the cantilever at a higher resonance mode. The vibration amplitude image is shown in Figure 108. It clearly shows two resonance nodes where the amplitudes are almost zero.

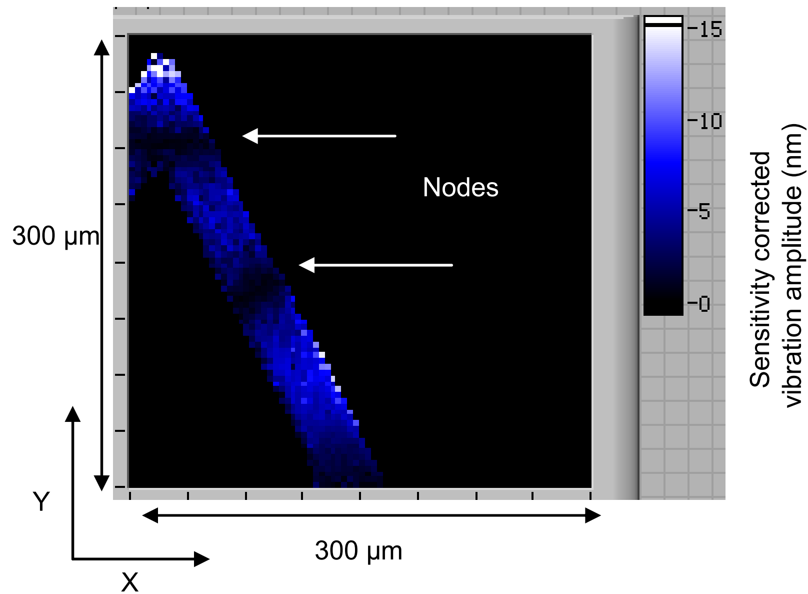

Figure 108 – Vibration amplitude image of the cantilever in its second resonance mode

The phase map is Figure 109 which shows the same two nodes and phase change at these two nodes. The data at the tip of the cantilever tends to be noisy because of the presence of the pyramidal sharp probe.

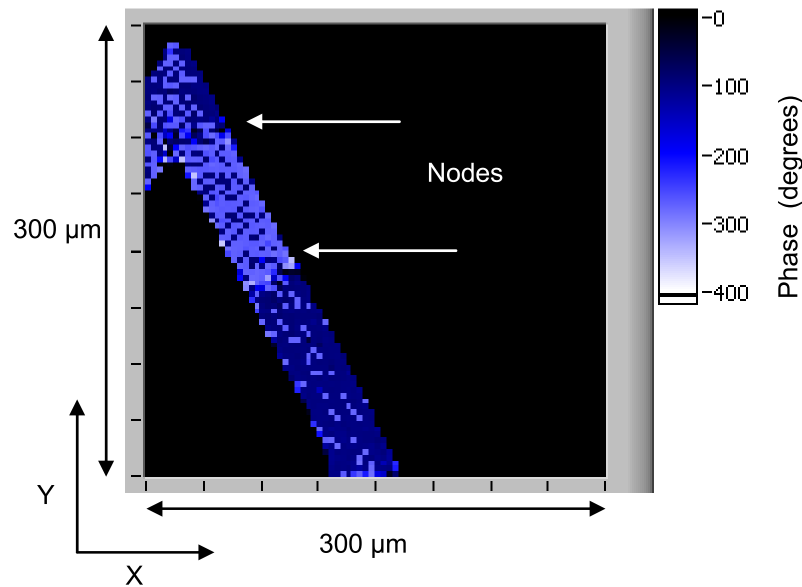

Figure 109 – Phase map of the cantilever in its second resonance mode

In conclusion, it is demonstrated that the µSGI has dynamic displacement measurement ability with phase information. It also maps the surface for its static surfaces based on the reflectivity of the surfaces.

6.4 Transient response measurements with µSGI

The µSGI enables dynamic measurement of the frequency response over large bandwidth in a short time. The measurement method is not limited to a particular frequency. To demonstrate the capability, the cantilever shown in Figure 104 is used. Data is collected at 25 MHz over 8ms. The data is plotted in Figure 110.

Fast Fourier Transform method is used to convert this data in to frequency domain. The Frequency response of the cantilever is shown in Figure 111. The first two resonance modes of the cantilever and the first resonance mode of the tunable grating can be distinctively observed in the response. Their frequency values match very well with the values used in the previous section.

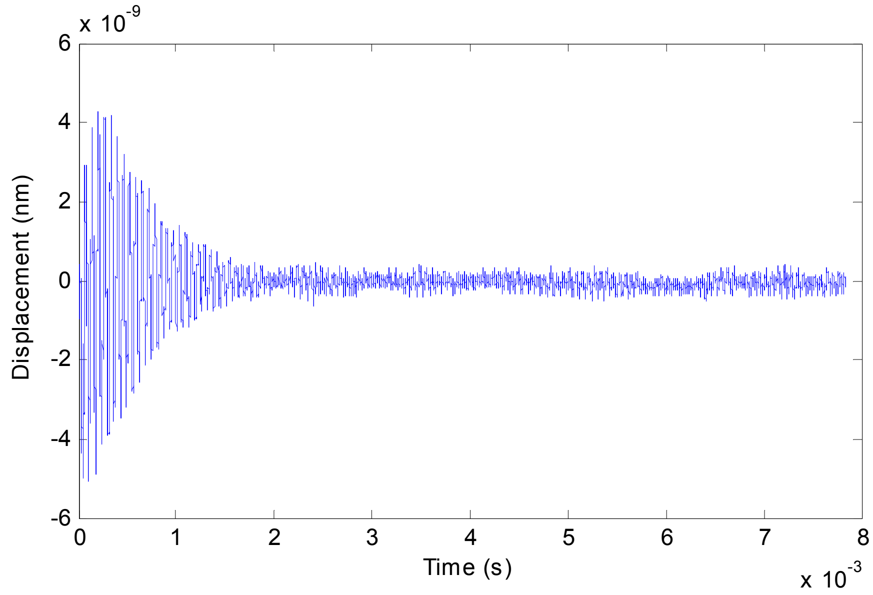

Figure 110 – Transient response of the cantilever to an impulse input, obtained using µSGI

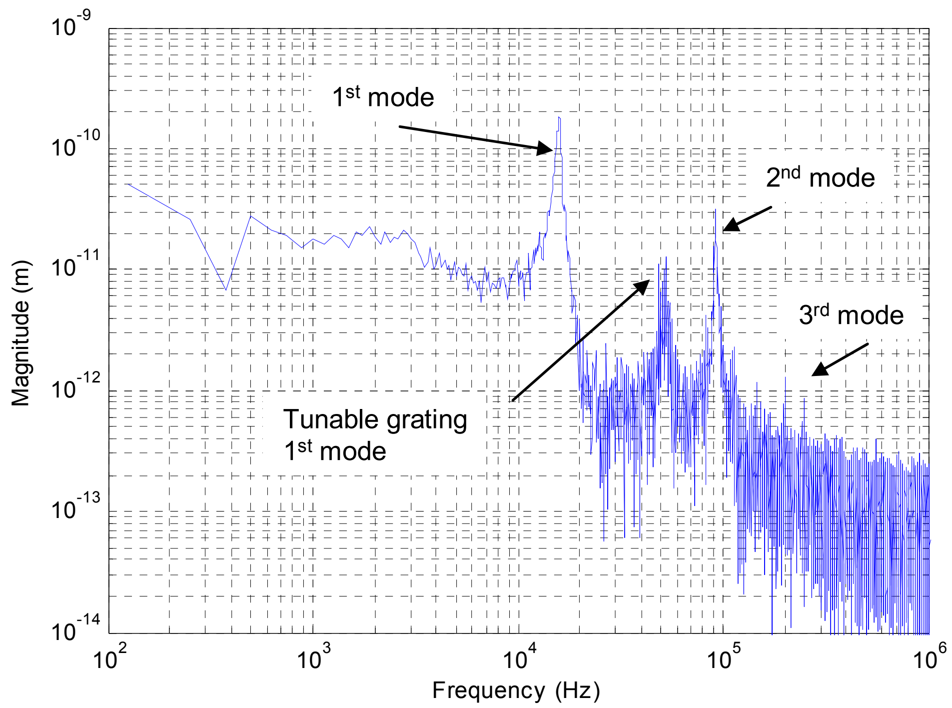

Figure 111 – The frequency response of the cantilever obtained from the transient response

CHAPTER 7

CONCLUSION

7.1 Conclusions and contributions

This project addresses the growing need of fast, high resolution, dynamic metrology methods. The technology developed in this project offers a miniaturized metrology tool which can also be operated in array fashion. It also offers interferometric resolution while the use of high bandwidth actuator reduces effect of ambient disturbances. It enables measurements over long range of distances without loss of resolution. The dynamic performance of a sample can be measured over a large bandwidth in a short time using such a tool. It can also be scanned over samples to observe the dynamic vibrations with phase information. This project develops the technology and demonstrates its capabilities using different experiments using μSGI as a demonstration tool.

This project also develops an SOI based tunable grating array for high bandwidth ambient disturbance reduction. These tunable gratings are designed and analyzed using the Finite Element method. The code used for the Finite Element modeling can be generalized to several similar membrane based devices. A MEMS based fabrication method is developed and implemented to fabricate such tunable membrane based devices. The fabrication method is easy to implement using two masks and achieves high yield. The tunable gratings show more than $\lambda/2$ (316nm) displacement in 30V actuation range and their first resonance around 50 kHz. A low squeezed film damping of 0.05 was achieved. The novel tunable grating membrane layout achieves a flat grating (<10nm maximum deformation) under the maximum actuation voltage. Stiction is also

avoided by the use of backside cavity. Thus this technology achieves several desired characters in a membrane based actuable device.

Optical setups are designed and analyzed using diffraction optics based simulations. Table top and miniaturized optical setups are designed and built. A lens has been integrated to achieve a lateral resolution of 6.6 μm. The lateral resolution can be improved with better optics. A vertical resolution of 0.052 nm over 875 kHz bandwidth has also been obtained, which is better than most of the existing techniques.

A novel low noise control algorithm is designed and analyzed using analytical models and simulations. The algorithm is implemented using FPGA at a loop rate of 180 kHz. Up to 40dB reduction of vibration noise is obtained in a bandwidth of 6.5 kHz which is sufficient to reduce the ambient disturbances. The model results are experimentally validated. A base noise level of $5.93 \times 10^{-5}\ nm_{rms}/\sqrt{Hz}$ is achieved. The novel control algorithm is modified to achieve parallel operation, where two parallel control loops are run independently on single FPGA, controlling two separate interferometric metrology tools. The range of measurement for such tools is extended by modifying the control algorithm, which is demonstrated by measuring a moving vibrating sample.

The scanning ability of the metrology tools is also demonstrated by scanning two MEMS based dynamic samples using two μSGIs on the same chip. Reflectivity, vibration amplitude and phase mapping are demonstrated by scanning the samples at their resonance modes. The transient response of the samples is also demonstrated using μSGI measuring the frequency response of the sample over a large bandwidth.

7.2 Potential applications

The new interferometric displacement measurement technology developed in this project is expected to have a broad impact. The current metrology techniques lack a high resolution, dynamic, long range and fast metrology technique. A metrology tool like µSGI array offers a solution to the problem. This study builds a platform technology which enables parallel, high resolution, long range, large bandwidth, fast, transient measurements of samples. Several such capabilities are made feasible by this technology may lead to several potential applications as discussed in the next section. The applications can be realized with the help of metrology tools like µSGI.

The on-line metrology in MEMS fabrication is a very good application. The parallel operation and dynamic measurement capabilities offer a fast characterization method. This may result in high yield fabrication of MEMS. Parallel measurements also enable simultaneous dynamic measurements of large areas which can be useful for testing of machines like automobiles.

High resolution dynamic displacement measurement has several applications in mechanical displacement based micro-sensors. Scanning probe microscopes uses the probe tip displacement measurement to measure the surface profile of the sample. Microphones use a deforming membrane to sense the pressure changes due to the sound. The technology developed in this project enables measurement of the membrane deformation with high resolution and high bandwidth. The parallel operation ability enables directionality measurements too. Similarly pressure sensors, accelerometers

The long range measurement using a miniaturized probe enables very precise displacement measurement over a long distance. This can be useful in precision

machining applications. The μSGI can be integrated with the machining tool or the sample and live-machining status can be observed with high precision.

The transient measuring capability is very useful in dynamic characterization of components. The transient response obtained from the μSGI gives a direct access to the frequency response of the sample without a need to sweep the frequencies. This is very time efficient from testing point of view.

The μSGIs are miniaturized metrology probes and can be placed and oriented in any configuration. This enables three-dimensional dynamic metrology of samples with phase information. This opens a new dimension for three-dimensional dynamic metrology.

7.3 Future work and recommendations

A few design changes are suggested to improve the current μSGI.

The backside mask could be modified to have etch lines avoid dicing step. Membrane size and the cavity size could be optimized to achieve more robust membranes before release.

After the device layer is etched the wafer has very large area where the Silicon oxide causes stress. Instead of removing device layer everywhere other than the μSGI area, it may be useful to etch only borders of the devices and keep the rest of the device layer un-etched.

Fiber collimator assembly needs further miniaturization so as that each μSGI on a chip can be illuminated.

The working distance of μSGI is 1.6mm which is low which may be improved for longer working distance.

Capabilities of μSGI can be tested different surfaces especially surfaces with transparent coatings.

The membrane dynamics can be altered by changing the etch hole size etc. A membrane with somewhat higher damping would give higher bandwidth of operation. It will also stabilize faster after the gain reversal jump resulting in less dead-time.

The control algorithm can be optimized by exploring the unused proportional and differential gains.

Digital signal processing (DSP) based dedicated hardware can be developed to further miniaturize the space requirement. Data acquisition system also needs to be more efficient to handle data from several μSGIs.

The current design of μSGI array for in-line metrology assumes that the μSGI array is custom built to be aligned over an array of sample devices. To enable easy customization of array operation, an automated method may be developed to move and place individual μSGI elements in an array to measured the required sample points.

REFERENCES

1. Peercy, P.S., *The drive to miniaturization.* Nature, 2000. **406**: p. 1023-1026.
2. Drexler, W., et al., *Submicrometer precision biometry of the anterior segment of the human eye.* Investigative Ophthalmology & Visual Science, 1997. **38**(7): p. 1304-1313.
3. Zielinski, M. and G. Ziller, *Noncontact vibration measurements on compressor rotor blades.* Measurement Science and Technology, 2000. **11**(7): p. 847-56.
4. Steinmetz, C.R., *Sub-Micron Position Measurement and Control on Precision Machine Tools With Laser Interferometry.* Precis. Eng., 1990. **12**(1): p. 12-24.
5. Loh, N.C., M.A. Schmidt, and S.R. Manalis, *Sub-10 cm 3 interferometric accelerometer with nano-gresolution.* Microelectromechanical Systems, Journal of, 2002. **11**(3): p. 182-187.
6. Onaran, A.G., et al., *A new atomic force microscope probe with force sensing integrated readout and active tip.* Review of Scientific Instruments, 2006. **77**: p. 023501.
7. Greywall, D.S., *Micromachined optical-interference microphone.* Sensors and Actuators A: Physical, 1999. **75**(3): p. 257-268.
8. Grbovic, D., et al., *Uncooled infrared imaging using bimaterial microcantilever arrays.* Applied Physics Letters, 2006. **89**: p. 073118.
9. Yao, J., *RF MEMS from a device perspective.* Journal of Micromechanics and Microengineering, 2000. **10**(4): p. 9-38.
10. Rebeiz, G.M., *RF MEMS*. 2003: Wiley-Interscience Hoboken, NJ.
11. Degertekin, F., R. Guldiken, and M. Karaman, *Annular-ring CMUT arrays for forward-looking IVUS: transducer characterization and imaging.* Ultrasonics, Ferroelectrics and Frequency Control, IEEE Transactions on, 2006. **53**(2): p. 474-482.
12. Graebner, J.E., et al., *Dynamic visualization of subangstrom high-frequency surface vibrations.* Applied Physics Letters, 2001. **78**: p. 159.
13. Panetta, K., Aluru, N., Bart, S., Blanton, S., Böhringer, K., Brown, R. *ITC 2000 Panel Discussion: Testing Challenges for MEMS*. in *Proceedings of ITC International Test Conference*. 2000.
14. Hall, N.A., et al., *Micromachined microphones with diffraction-based optical displacement detection.* The Journal of the Acoustical Society of America, 2005. **118**: p. 3000.
15. Kim, B., *Miniaturized Diffraction Based Interferometric Distance Measurement Sensor*. 2004.
16. Hitachi. *S-5500 In-Lens FE SEM*. 2008 [cited; Available from: http://www.hitachi-hta.com/pageloader~type~product~id~389~orgid~42.html.
17. Gilles, J.P., et al., *Scanning electron microscopy for vacuum quality factor measurement of small-size MEMS resonators.* Sensors & Actuators: A. Physical, 2008. **145**: p. 187-193.
18. Wong, C.L. and W.K. Wong, *In-plane motion characterization of MEMS resonators using stroboscopic scanning electron microscopy.* Sensors & Actuators: A. Physical, 2007. **138**(1): p. 167-178.

19. Storment, C.W., et al., *Flexible, dry-released process for aluminum electrostatic actuators.* Microelectromechanical Systems, Journal of, 1994. **3**(3): p. 90-96.

20. Opsal, J.L., et al., *Fundamental solutions for real-time optical CD metrology.* Proceedings of SPIE, 2002. **4689**: p. 163.

21. Lagerquist, M.D., W. Bither, and R. Brouillette, *Improving SEM linewidth metrology by two-dimensional scanning force microscopy.* Proceedings of SPIE, 1996. **2725**: p. 494.

22. Marchman, H.M. and N. Dunham, *AFM: a valid reference tool?* Proceedings of SPIE, 1998. **3332**: p. 2.

23. Svetkoff, D.J. and D.B. Kilgus, *Influence of object structure on the accuracy of 3-D systems for metrology.* Proceedings of SPIE, 1992. **1614**: p. 218.

24. Petitgrand, S. and A. Bosseboeuf, *Simultaneous mapping of out-of-plane and in-plane vibrations of MEMS with (sub) nanometer resolution.* JOURNAL OF MICROMECHANICS AND MICROENGINEERING, 2004. **14**(9): p. 97-101.

25. O Mahony, C., et al., *Characterization of micromechanical structures using white-light interferometry.* Measurement Science and Technology, 2003. **14**(10): p. 1807-1814.

26. de Groot, P.J. and L.L. Deck, *Surface profiling by frequency-domain analysis of white light interferograms.* Proceedings of SPIE, 1994. **2248**: p. 101.

27. Clair, L.E.S., A.R. Mirza, and P. Reynolds, *Metrology for MEMS Manufacturing.* Sensors Magazine, 2000. **17**(7).

28. Wyant, J.C., *White Light Interferometry.* Proceedings of SPIE-The International Society for Optical Engineering, 2002. **4737**: p. 98-107.

29. Veeco. *DMEMS NT3300*. 2008 [cited; Available from: http://www.veeco.com/pdfs.php/395.

30. Corle, T.R. and G.S. Kino, *Confocal Scanning Optical Microscopy and Related Imaging Systems*. 1996: Academic Press.

31. Shin, H., et al., *Fiber-optic confocal microscope using a MEMS scanner and miniature objective lens.* Optics Express, 2007. **15**(15): p. 9113-9122.

32. Binnig, G., C.F. Quate, and C. Gerber, *Atomic Force Microscope.* Physical Review Letters, 1986. **56**(9): p. 930-933.

33. Marchman, H.M., *Nanometer-scale dimensional metrology with noncontact atomic force microscopy.* Proceedings of SPIE, 1996. **2725**: p. 527.

34. Veeco. *Innova SPM*. 2008 [cited; Available from: http://www.veeco.com/pdfs/datasheets/B67_RevA1_Innova_Datasheet.pdf.

35. Humphris, A.D.L., M.J. Miles, and J.K. Hobbs, *A mechanical microscope: High-speed atomic force microscopy.* Applied Physics Letters, 2005. **86**: p. 034106.

36. Van Gorp, B., A.G. Onaran, and F.L. Degertekin, *Integrated dual grating method for extended range interferometric displacement detection in probe microscopy.* Applied Physics Letters, 2007. **91**: p. 083101.

37. Lawrence, E.M., K.E. Speller, and D. Yu, *MEMS characterization using Laser Doppler Vibrometry.* Proceedings of SPIE, 2003. **4980**: p. 51.

38. Polytec, I. *MSA-500 Micro System Analyzer*. 2008 [cited 2008 September 24]; Available from: http://www.polytec.com/usa/_files/OM_BR_MSA-500_2008_06_US_draft.pdf.

39. Novak, E., *MEMS metrology techniques.* Proceedings of SPIE, 2005. **5716**: p. 173.

40. Coppola, G., et al., *A digital holographic microscope for complete characterization of microelectromechanical systems.* Measurement Science and Technology, 2004. **15**(3): p. 529-539.

41. Emery, Y., et al. *Digital holography microscopy (DHM): fast and robust systems for industrial inspection with interferometer resolution*. in *Optical Measurement Systems for Industrial Inspection IV*. 2005. Munich, Germany: SPIE.

42. Seebacher, S., et al., *The determination of material parameters of microcomponents using digital holography.* Optics and Lasers in Engineering, 2001. **36**(2): p. 103-126.

43. Brown, G.C. and R.J. Pryputniewicz, *Holographic microscope for measuring displacements of vibrating microbeams using time-averaged, electro-optic holography.* Optical Engineering, 1998. **37**(5): p. 1398-1405.

44. Hariharan, P., *Optical holography*. 1984: Cambridge University Press New York.

45. Veeco. *Wyko NT9800 Datasheet* 2008 [cited; Available from: http://www.veeco.com/pdfs.php/282.

46. Polytec. *HS10 long-range laser scale*. 2007 [cited; Available from: http://www.renishaw.com/en/6484.aspx.

47. GmbH, P. *TMS-100 TopMap Metro.Lab*. 2007 [cited; Available from: http://www.polytec.com/usa/_files/OM_DS_TMS-100_2007_03_US.pdf.

48. Polytec. *MSV-400 Microscope Scanning Vibrometer - Technical Data*. 2008 [cited; Available from: http://www.polytec.com/int/158_467.asp?

49. Polytec. *TMS-100 TopMap Metro.Lab*. 2007 [cited; Available from: http://www.polytec.com/usa/_files/OM_DS_TMS-100_2007_03_US.pdf.

50. Dektak. *Dektak 150 Surface Profiler Datasheet*. 2007 [cited; Available from: http://www.veeco.com/pdfs.php/384.

51. Lyncee. *Lyncee Tec - Key feartures*. 2007 [cited 2007 November 30, 2007]; Available from: http://www.lynceetec.com/content/view/181/155/.

52. Polytec, I. *MSA-400 Micro System Analyzer*. 2005 [cited 2007 July 13]; Available from: http://www.polytec.com/usa/_files/LM_BR_MSA-400_2005_11_3000_E(1).pdf.

53. Graebner, J.E., *Optical scanning interferometer for dynamic imaging ofhigh-frequency surface motion.* Ultrasonics Symposium, 2000 IEEE, 2000. **1**.

54. Kim, B., et al., *Scanning grating microinterferometer for MEMS metrology.* Journal of manufacturing science and engineering, 2004. **126**(4): p. 807-812.

55. Trisnadi, J.I., C.B. Carlisle, and R. Monteverde, *Overview and applications of Grating-Light-Valve-based optical write engines for high-speed digital imaging (Invited Paper)[5348-05].* Proceedings - SPIE The International Society for Optical Engineering, 2004: p. 52-64.

56. Manalis, S.R., *Interdigital cantilevers for atomic force microscopy.* Applied Physics Letters, 1996. **69**(25): p. 3944.

57. Solgaard, O., F.S.A. Sandejas, and D.M. Bloom, *Deformable Grating Optical Modulator.* Optics Letters, 1992. **17**(9): p. 688-690.

58. Wagner, J.W. and J.B. Spicer, *Theoretical noise-limited sensitivity of classical interferometry.* J. Opt. Soc. Am. B, 1987. **4**(8): p. 1316-1326.

59. Freschi, A.A. and J. Frejlich, *Adjustable phase control in stabilized interferometry.* Opt. Lett, 1995. **20**(6): p. 635-637.

60. Yoshino, T., et al., *Laser diode feedback interferometer for stabilization and displacement measurements.* Appl. Opt, 1987. **26**(5): p. 892-897.

61. Liu, J. and I. Yamaguchi, *Surface profilometry with laser-diode optical feedback interferometer outside optical benches.* Applied Optics, 2000. **39**(1): p. 104-107.

62. He, L., *Vibration-compensated interferometry system using phase-modulating interference fringe subdivision technology.* Applied Optics, 2006. **45**(31): p. 7987-7992.

63. de Groot, P., *Vibration in phase-shifting interferometry.* J. Opt. Soc. Am. A, 1995. **12**(2): p. 354-365.

64. Holmgren, O., et al., *Imaging of in-and out-of-plane vibrations in micromechanical resonator.* Electronics Letters, 2005. **41**(3): p. 121-122.

65. Zhou, G. and F.S. Chau, *Grating-Assisted Optical Microprobing of In-Plane and Out-of-Plane Displacements of Microelectromechanical Devices.* Microelectromechanical Systems, Journal of, 2006. **15**(2): p. 388-395.

66. Kim, B., F.L. Degertekin, and T.R. Kurfess, *Micromachined scanning grating interferometer for out-of-plane vibration measurement of MEMS.* Journal of Micromechanics and Microengineering, 2007. **17**: p. 1888-1898.

67. Madou, M.J., *Fundamentals of Microfabrication: The Science of Miniaturization*. 2002: CRC Press.

68. Tan, S.M., in *Linear Systems*.

69. Karhade, O.G., Degertekin, F. L, Kurfess, T. R. *Scanning Micro Interferometer with Tunable Grating*. in *Proceedings of the 15th International Symposium on Electromachining*. 2007. Pittsburgh, PA.

70. Schmittdiel, M., *Active control of a diffraction grating interferometer for microscale devices*, in *School of Mechanical Engineering*. 2004, Georgia Institute of Technology.

71. Karhade, O.G., F.L. Degertekin, and T.R. Kurfess. *Scanning Micro Interferometer with Tunable Grating*. in *Proceedings of the 15th International Symposium on Electromachining*. 2007. Pittsburgh, PA.

72. *NI-PXI-7831R*. National Instruments 2008 [cited; Available from: http://sine.ni.com/nips/cds/view/p/lang/en/nid/11828.

73. Karhade, O.G., F.L. Degertekin, and T.R. Kurfess, *SOI-based micro scanning grating interferometers: device characterization, control and demonstration of parallel operation.* J. Micromech. Microeng, 2008. **18**(045007): p. 045007.

74. Karhade, O.G., L. Degertekin, and T.R. Kurfess, *Scanning micro-interferometer array with sub-picometer resolution for MEMS inspection.* Sensors Applications Symposium, 2008. SAS 2008. IEEE, 2008: p. 113-118.

75. Karhade, O.G., *SOI-Based Micro Scanning Grating Interferometer - Device Characterization Control and Demonstration of Parallel Operation.* Journal of Micromechanics and Microengineering, 2008. **18**(045007).

76. De Groot, P., *Extending the unambiguous range of two-color interferometers.* Applied Optics, 1994. **33**(25/1).

77. Gelmini, E., U. Minoni, and F. Docchio, *Tunable, double-wavelength heterodyne detection interferometer for absolute-distance measurements.* SPIE MILESTONE SERIES MS, 1995. **115**: p. 649-651.

78. Strand, T. and Y. Katzir, *Extended unambiguous range interferometry.* Appl. Opt, 1987. **26**(19): p. 4274.

79. Culshaw, B., *Optical fibre sensing and signal processing*. 1984: Peregrinus.

80. Hung, S., et al., *Dual-Stage Piezoelectric Nano-Positioner Utilizing a Range-Extended Optical Fiber Fabry–Perot Interferometer.* Mechatronics, IEEE/ASME Transactions on, 2007. **12**(3): p. 291-298.

81. Van Gorp, B., A. Onaran, and F. Degertekin, *Integrated dual grating method for extended range interferometric displacement detection in probe microscopy.* Applied Physics Letters, 2007. **91**: p. 083101.

82. Onaran, A., et al., *A new atomic force microscope probe with force sensing integrated readout and active tip.* Review of Scientific Instruments, 2006. **77**: p. 023501.

83. Veeco. *Veeco Probes Catalogue*. 2008 [cited; Available from: http://www.veeco-europe.com/data/editor/documents/probe-catalogue.pdf.

APPENDICES

7.1 Finite element code for iterative simulations of structures with varying dimensions

```
!Omkar Karhade
!Georgia Tech
!µSGI simulations

!***PROGRAM INITIALIZATION***!
FINISH                                  !FINISH AND EXIT ANY EXISTING JOB
/CLEAR,NOSTART                          !CLEAR THE DATABASE
/FILENAME,MICROSI15e10,1                !SET THE JOBNAME TO 'MICROSI', START NEW ERROR AND LOG FILES

SAVE,DATA,,,ALL


s_l=250                                 !Plate length (µm)
s_elec=80                               !Electrode width
s_w=200                                 !Plate width
!s_t=2.5                                !Plate thickness
s_g=100                                 !grating half length
s_g_h=125                               !grating hole half side width
s_g_h1=150                              !grating hole half side length
s_g_s=115                               !grating surface half side
g_p=40                                  !grating period
g_w=13                                  !grating width
w_conn=20                               !half width of the connections

d_el=1                                  !Gap
pamb=.1                                 !ambient pressure (MPa)
visc=18.3e-12                           !viscosity kg/(µm)(s)
pref=.1                                 !Reference pressure (MPa)
mfp=64e-3                               !mean free path (µm)
Knud=mfp/d_el                           !Knudsen number
dmp_alph=8539.1
dmp_bt=1.2E-7
E_si=169E3                              ! Young's modulus (kg/s^2/µm)
a_si=1e-6                               ! Alpha of silicon (/deg)
res_stress=12                           ! Residual stress (kg/s^2/µm = MPa)
res_temp=res_stress/(E_si*a_si)
iter=1

*DIM,result,,10,2
```

```
*DO,s_t,2.7,2.7,.4                     ! Optionally change variable values for
                                       iterative simulations
                                       ! Delete the results file beforehand from
                                       the directory of using this

/PREP7
/title, Response of uSGI
/com    uMKS units
/com,   Small deflection assumption

et,1,200,6                             ! Meshing facet
ET,2,plane42                           ! no viscocity region
ET,3,45                                ! Structural element

mp,ex,3,169e3                          ! Si
mp,dens,3,2300e-18
mp,nuxy,3,.2
mp,damp,1,dmp_bt                       ! Material damping (from squeeze film
                                       results)
!mp,damp,2,0
!mp,dmpr,1,10709
!mp,dmpr,2,0
mp,ex,2,169e-6                         ! Si
mp,dens,2,2300e-27
mp,nuxy,2,.2
mp,alpx,3,a_si

! Build the model

rectng,-s_l+s_elec,s_l-s_elec,-s_w,s_w ! Membrane
rectng,-s_g_h1,s_g_h1,-s_g_h,s_g_h
asba,1,2
numstr,area,4
rectng,-s_g_s,s_g_s,-s_g_s,s_g_s       ! Grating
rectng,-s_g,s_g,-s_g,s_g
asba,4,5
rectng,-w_conn,w_conn,s_g_s,s_g_h
rectng,-w_conn,w_conn,-s_g_s,-s_g_h
rectng,-s_l,-s_l+s_elec,-s_w,s_w       ! Plate domain
rectng,s_l-s_elec,s_l,-s_w,s_w

*DO,NFING,-s_g/g_p,s_g/g_p-1,1
rectng,-s_g,s_g,NFING*g_p+(g_p-
g_w)/2,NFING*g_p+g_w+(g_p-g_w)/2       ! Grating fingers
*ENDDO

asel,all
aglue,all
asel,all
asel,,loc,x,-s_l,-s_l+s_elec
asel,a,loc,x,s_l-s_elec,s_l
```

```
aatt,1,1,1
asel,,loc,x,-s_elec,s_elec
aatt,2,2,2
allsel,all

esize,10
AMESH,all                                  ! Mesh plate domain
esize,,2
type,3
mat,3
real,3
asel,all

vext,all,,,,,s_t                           ! Extrude structural domain
allsel,all
allsel,all

nsel,s,loc,x,-s_l                          ! Clamp one end
d,all,ux
d,all,uy
d,all,uz

                                           ! Induce a displacement corresponding
nsel,,loc,x,s_l                            to stress in other end
d,all,ux,-2*s_l*res_stress/E_si
d,all,uy
d,all,uz

allsel,all
aclear,all
save

nsel,s,loc,z
nsel,u,loc,x,-s_l+s_elec,s_l-s_elec
cm,base,nodes
emtgen,'base',,,'uz',-d_el                 ! generate Transducer elements
allsel,all
nsel,s,loc,z,-d_el
d,all,uz,0
nsel,s,loc,z,-d_el
d,all,volt,0
allsel,all

allsel,all
fini

/solu
antype,static,new
cmsel,s,base
d,all,volt,25                              ! Apply 25V
```

```
allsel,all
pstress,on
!nlgeom,on                              ! Optionally use non-linear geometries
solve
fini

                                        ! Get z displacement for the center of the
n1=node(50,50,s_t)                      grating
*GET,result(iter,1,1),NODE,n1,U,z       ! Save it in result array

!/solu
!antype,modal,new                       ! Optionally do a modal analysis
!MODOPT,damp,2,1E3,200E3
                                        ! Note: nlgeom should not be on for
!pstress,on                             pstress on in modal
!alphad,dmp_alph
!outres,all,all
!mxpand,10
!solve
!finish

!*GET,result(iter,2,1),mode,1,freq,imag

iter=iter+1
parsav,all,results,                     ! Save results to "results" file

!***PROGRAM REINITIALIZATION***!!

RESUME,DATA,,,,
PARRES,,RESULTS,

*ENDDO                                  ! Go to next step
```

Example of the result variable in the results file

```
*DIM,RESULT  ,ARRAY,     10,      2,      1,
*SET,RESULT  (          1,          1,          1), -
1.897968714360
*SET,RESULT  (          2,          1,          1),-
0.7739008222002
*SET,RESULT  (          3,          1,          1),-
0.1731741236429
*SET,RESULT  (          4,          1,          1),-
0.7321408033868E-01
*SET,RESULT  (      5,      1,      1),-0.3913939384123E-01
```

7.2 *Optical setup simulation – diffraction optics based code*

```
clear all
close all

% ALL DISTANCES ARE ON Z AXIS

% f0: at the pupil
% f1: before the first grating
% f2: after the first grating
% f3: before first lens
% f4: after first lens
% f5: before sample
% f6: after sample
% f7: before second lens
% f8: after second lens
% f9: before second grating
% f10: after second grating
% f11: after adding the two beams
% f12: at the photodiode

% 40 periods, 2 µm finger, 3 µm space
finger = 2e-6;
space = 3e-6;

N = 2^16;   % number of points : 2^15
lambda = 633e-9;

L = 14400e-6;
grating_start = -100e-6;
grating_end = 100e-6;
dx0 = L/N;
k = 2*pi / lambda;
f = 1e-3;  % focal distance of the lens
R_sample = 0.7; % sample reflectivity

z_pg=8e-3;  % z_pg : distance from pupil to grating
z_gl=.5e-3; % z_gl : distance from grating to lens
z_ls=0;    % z_ls : distance from lens to sample (defined in the loop)
z_pd=8e-3;  % z_pd : distance from grating to photodiode

order0 = zeros(1,N);
order1 = zeros(1,N);

order1start=-1.3e-3;
order1end=-.7e-3;
order0start=-.3e-3;
order0end=.3e-3;

%tic
% DEFINE GAUSSIAN BEAM
beam_width = 280e-6;
pupil_width = 100e-6;
beam = sqrt(exp(-(-N/2+1:N/2).^2./(beam_width/2/dx0).^2));
```

```
% 0) CROP THE BEAM
f0 = zeros(size(beam));
f0(N/2-1-
round(pupil_width/dx0/2):N/2+round(pupil_width/dx0/2))=beam(N/2-1-
round(pupil_width/dx0/2):N/2+round(pupil_width/dx0/2));

p=0;
% 1) PROGAGATE TILL GRATING
[f1,dx1,x1]=fresnel(f0,dx0,z_pg,lambda);
figure;
p=p+1;subplot(3,2,p);plot(x1,abs((beam).^2));xlim([-500e-6 500e-
6]);title('1. Gaussian beam');xlabel('Distance from axis
(m)'),ylabel('Normalized intensity');
p=p+1;subplot(3,2,p);plot(x1,abs((f0).^2));xlim([-500e-6 500e-
6]);title('2. Cropped beam');xlabel('Distance from axis
(m)'),ylabel('Normalized intensity');
p=p+1;subplot(3,2,p);plot(x1,abs((f1).^2));xlim([-500e-6 500e-
6]);title('3. At the grating');xlabel('Distance from axis
(m)'),ylabel('Normalized intensity');

f_grating = zeros(1,N);
for i = 1:N
    if (rem(i*dx1,finger+space) < space)
        f_grating(i) = 1;
    end
    if (i*dx1-dx1*N/2 < grating_start) || (i*dx1-dx1*N/2 > grating_end)
        f_grating(i) = 0;
    end
end

% 2) PASS THROUGH 1ST GRATING
f2= f_grating.*f1; dx2 = dx1; x2=x1;
p=p+1;subplot(3,2,p);plot(x2,abs((f2).^2));xlim([-500e-6 500e-
6]);title('4. After grating');xlabel('Distance from axis
(m)'),ylabel('Normalized intensity');

% 2B) BEAM REFLECTED FROM GRATING
f_inverse_grating = zeros(1,N);
    for i = 1:N
        if (rem(i*dx1,finger+space) < space)
            f_inverse_grating(i) = 1;
        end
        if (i*dx1-dx1*N/2 < grating_start) || (i*dx1-dx1*N/2 >
grating_end)
            f_inverse_grating(i) = 0;
        end
    end
f2 = f_inverse_grating.*f1;
p=p+1;subplot(3,2,p); plot(x2,abs((f2).^2));xlim([-500e-6 500e-
6]);title('4B. Beam reflected from grating');xlabel('Distance from axis
(m)'),ylabel('Normalized intensity');

% 3) 1ST GRATING TO 1ST LENS
[f3,dx3,x3]=fresnel(f2,dx2,z_gl,lambda);
p=p+1;subplot(3,2,p); plot(x3,abs((f3).^2));xlim([-500e-6 500e-6]);
title('5. At the lens');xlabel('Distance from axis
(m)'),ylabel('Normalized intensity');

% 4) FIRST LENS
```

```
f_lens(1:N) = exp(-j*k*((-N/2+1:N/2)*dx3).^2/(2*f));
f4 = f3.*f_lens; dx4 = dx3; x4 = x3;

iter=1;
for disp=-100e-9:30e-9:300e-9

    close all;

    z_ls=1e-3+disp;    % z_ls: 2 x distance from the lens to the
substrate

    % 5) FIRST LENS TO SAMPLE
    [f5,dx5,x5]=fresnel(f4,dx4,z_ls,lambda);
    figure;p=0;
    p=p+1;subplot(3,2,p); plot(x5,abs((f5).^2)); xlim([-1500e-6 1500e-
6]);title('6. At the sample');xlabel('Distance from axis
(m)'),ylabel('Normalized intensity');

    % 6) PASS THROUGH SAMPLE
    f6 = f5.*R_sample; dx6 = dx5; x6 = x5;

    % 7) SAMPLE TO 2ND LENS
    [f7,dx7,x7]=fresnel(f6,dx6,z_ls,lambda);
    p=p+1;subplot(3,2,p); plot(x7,abs((f7).^2));xlim([-1500e-6 1500e-
6]);title('7. Back to lens');xlabel('Distance from axis
(m)'),ylabel('Normalized intensity');

    % 8) 2ND LENS
    f8 = f7.*f_lens; dx8 = dx7; x8 = x7;

    % 9) 2ND LENS TO GRATING
    [f9,dx9,x9]=fresnel(f7,dx7,z_gl,lambda);
    p=p+1;subplot(3,2,p); plot(x9,abs((f9).^2));xlim([-1500e-6 1500e-
6]);title('8. Back to grating');xlabel('Distance from axis
(m)'),ylabel('Normalized intensity');

    f_grating = zeros(1,N);
    for i = 1:N
        if (rem(i*dx9,finger+space) < space)
            f_grating(i) = 1;
        end
        if i*dx9-dx9*N/2 < grating_start || i*dx9-dx9*N/2 > grating_end
            f_grating(i) = 0;
        end
    end

    % 10) PASS THROUGH 2ND GRATING
    f10= f_grating.*f9; dx10 = dx9; x10=x9;
    p=p+1;subplot(3,2,p); plot(x9,abs((f9).^2));xlim([-1500e-6 1500e-
6]);title('9. After passing through the gratings second
time');xlabel('Distance from axis (m)'),ylabel('Normalized intensity');

    % 11) ADD THE INTERFERING BEAMS

    if dx2==dx10
        f11=f2+f10;dx11=dx10;x11=x10;
    elseif dx2>dx10
        f2_new=zeros(1,N);
        for i=1:N
            f2_new(i)=f2(round(N/2+(i-N/2)*dx10/dx2));
```

```
        end
        f11=f2_new+f10; dx11=dx2; x11=x2;
    else
        f10_new=zeros(1,N);
        for i=1:N
            f10_new(i)=f10(round(N/2+(i-N/2)*dx2/dx10));
        end
        f11=f10_new+f2;dx11=dx10;x11=x10;
    end

    p=p+1;subplot(3,2,p); plot(x2,abs((f2).^2));xlim([-1500e-6 1500e-
6]);title('10. Addition of two interfering beams (4B and 9) at the
grating');xlabel('Distance from axis (m)'),ylabel('Normalized
intensity');

    %AT PHOTODIODE
    [f12,dx12,x12]=fresnel(f11,dx11,z_pd,lambda);
    p=p+1;subplot(3,2,p); plot(x12,abs((f12).^2));xlim([-1500e-6 1500e-
6]);title('11. At the PD');xlabel('Distance from axis
(m)'),ylabel('Normalized intensity');


    for i=1:N
        if (x12(i)>order0start)&&(x12(i)<order0end)
            order0(i)=1;
        end
        if (x12(i)>order1start)&&(x12(i)<order1end)
            order1(i)=1;
        end
    end
    order0profile=order0.*f12;
    order1profile=order1.*f12;

    I1(1,iter) = sum(abs(order0profile.^2));
    I0(1,iter) = sum(abs(order1profile.^2));
    I1(1,iter) = max(abs(order0profile.^2));
    I0(1,iter) = max(abs(order1profile.^2));
    I0(2,iter) = disp;
    iter=iter+1;
end
figure;plot(I0(2,:),I1(1,:));xlabel('Displecement of sample
(m)');ylabel('Normalized intensity of the first order');
```

FILE fresnel.m

```
function[f1,dx1,x1]=fresnel(f0,dx0,z,lambda)
N = length(f0);
k = 2*pi/lambda;
zcrit= N*dx0^2/lambda;

if z < zcrit
du=1./(N*dx0);
u = [0:N/2-1 -N/2:-1]*du; % Note order of points for FFT
H = exp(-i*2*pi^2*u.^2*z/k); % Fourier transform of kernel
f1=ifft(fft(f0).*H);%Convolution
f1=f1.*exp(-j*2*pi*z/lambda); % ADDED NOW
dx1=dx0;
```

```
x1 = [-N/2:N/2-1]*dx1;%Baselineforoutput
end

if z >= zcrit
x0=[-N/2:N/2-1]*dx0;%Inputf0isinnaturalorder
g = f0 .* exp(i*0.5*k*x0.^2/z); % First phase factor
G = fftshift(fft(fftshift(g))); % Fourier transform
du=1./(N*dx0);dx1=lambda*z*du;
x1=[-N/2:N/2-1]*dx1;%Baselineforoutput
f1=G.*exp(i*0.5*k*x1.^2/z);%Secondphasefactor
f1=f1.*dx0./sqrt(i*lambda*z);
f1 = f1.*exp(-j*2*pi*z/lambda); % ADDED NOW (THE PHASE CHANGE DUE TO Z
TRAVEL)
end
```

7.3 Implementation on FPGA and RT using LabVIEW

The active path stabilization is implemented on FPGA using LabVIEW FPGA module. LabVIEW gives a user friendly tool to program the hardware. The graphical user interface (GUI) of LabVIEW shows the program in the form of block diagrams and the data flow through the blocks. It is easy to understand the program using the GUI of LabVIEW, hence snapshots of the code is shown in Figure 112 to Figure 115. This program is run on FPGA PXI-7831R, and is called from a Real-Time (RT) program run on a RT controller. Data is continuously transferred between the FPGA and the RT.

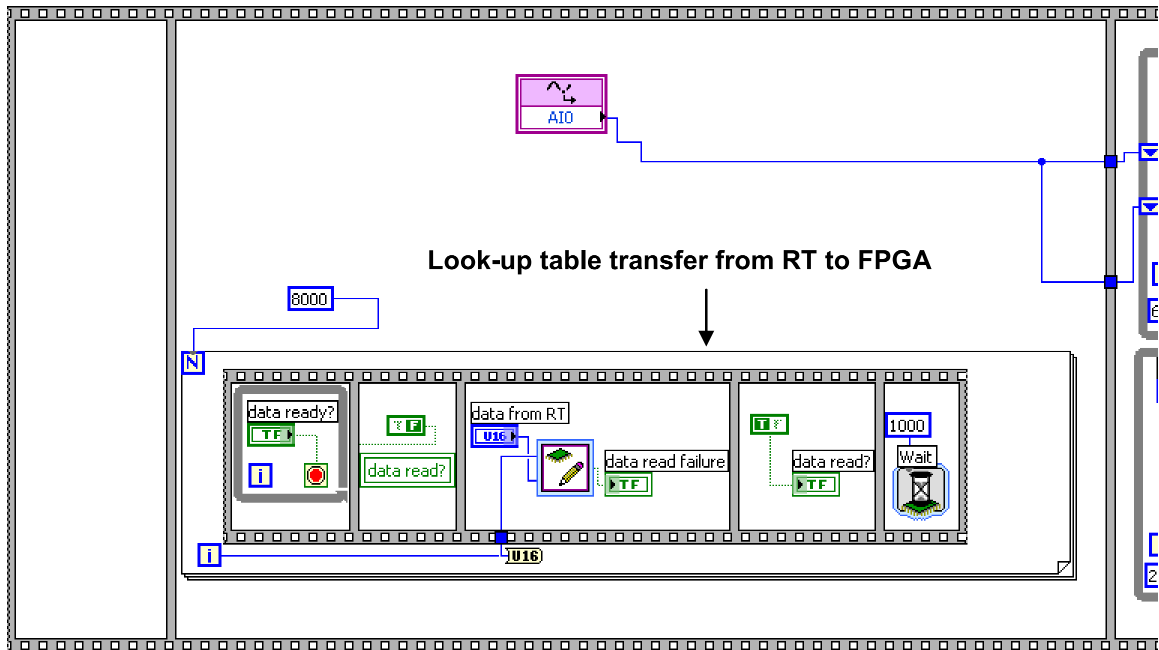

Figure 112 – LabVIEW FPGA code – block 1 receives the calibration chart (non-linearity lookup table) from the RT

Figure 112 shows the first step of the code which acquires the look-up table from the RT. The RT runs another program to generate the look-up code and transfers it to the FPGA using a double hand-shake method. For each element of the array, the RT signals that the data is ready. The FPGA tells the RT that it is reading data and reads the data. After reading the data the FPGA informs the RT machine that the data is read and then waits for some time to allow the RT to read FPGA's status. The RT updates the data with the next element and again lets the FPGA know that the data is ready. The look-up table consists of 8000 elements which is slightly less that the maximum size of the look-up table permitted by the FPGA.

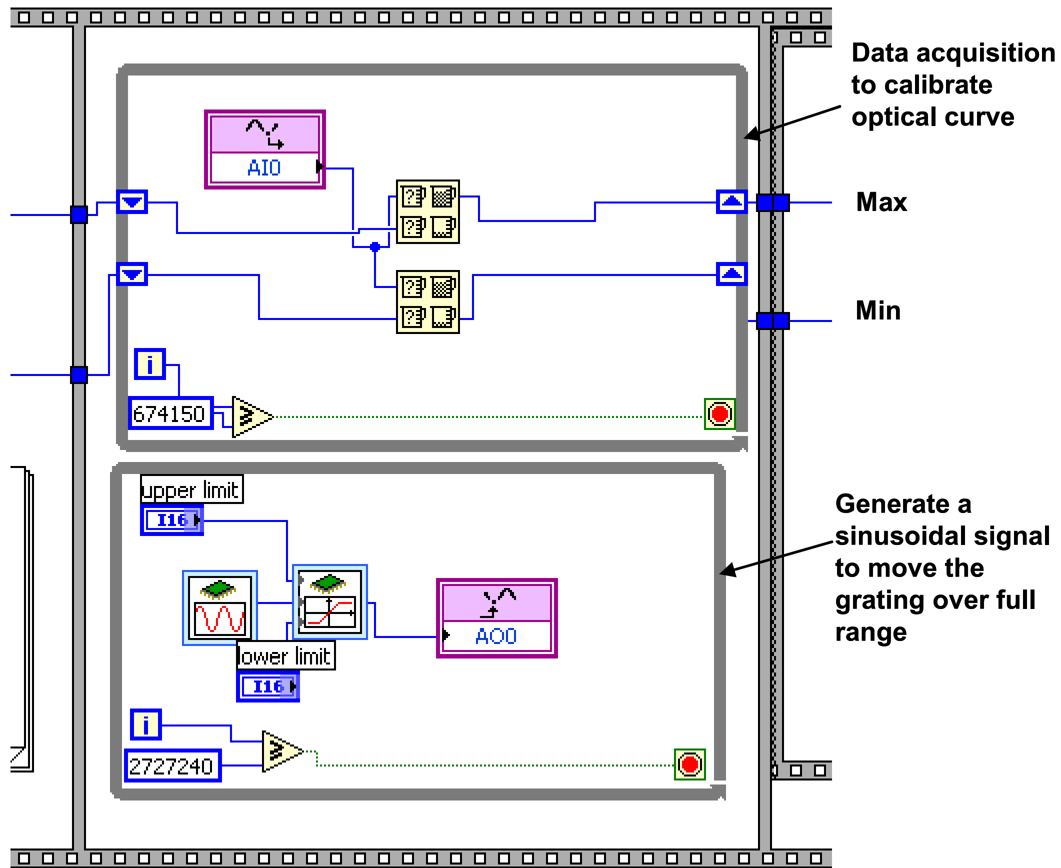

Figure 113 – Step 2 – Finding the desired point of operation by calibration of the optical curve.

In the step 2, as shown in the Figure 113, two loops are run in parallel. One of the loops generates a sinusoidal motion of the grating, truncated at the range limits. The other loop acquires the photo-detector signal simultaneously. The loop also compares the acquired data to find the maximum and minimum of the data range. These points give the upper and lower limits of the optical curve which in turn defines the optical curve. The desired point of operation is roughly at the mean of these values and is obtained in the next step shown in Figure 114.

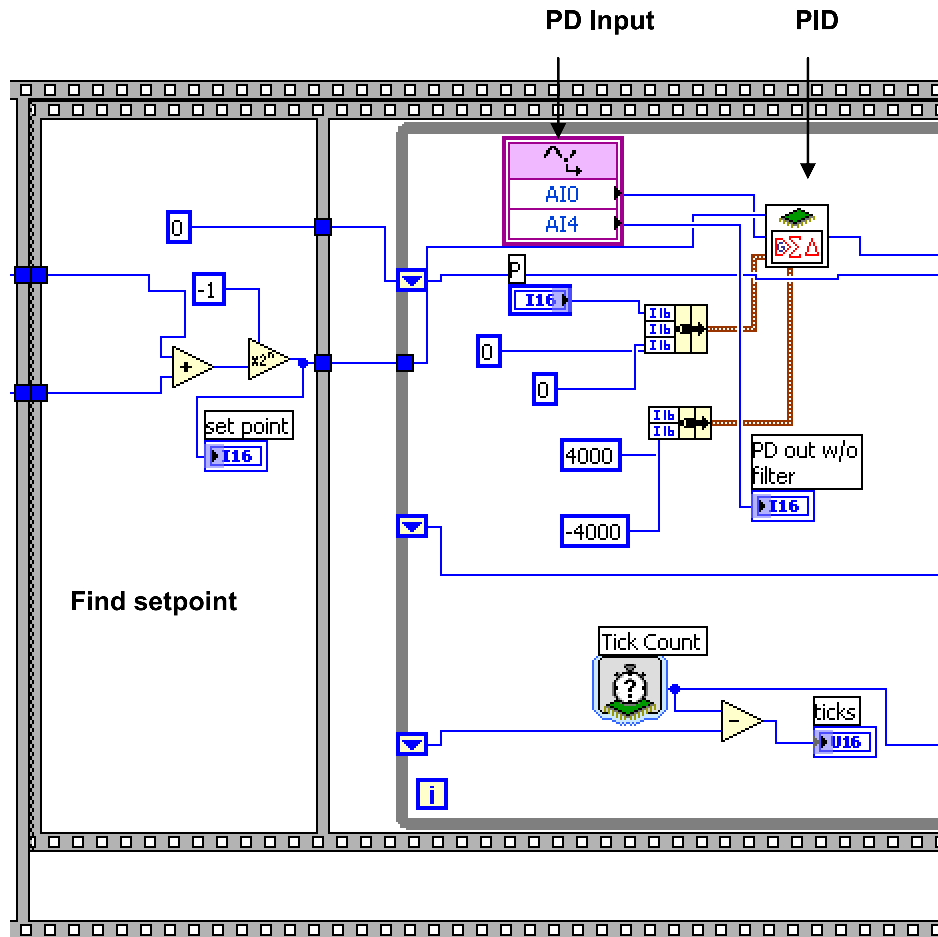

Figure 114 – Step -3 (half screen) The setpoint is found and PID control with gain reversal and look-up table is implemented.

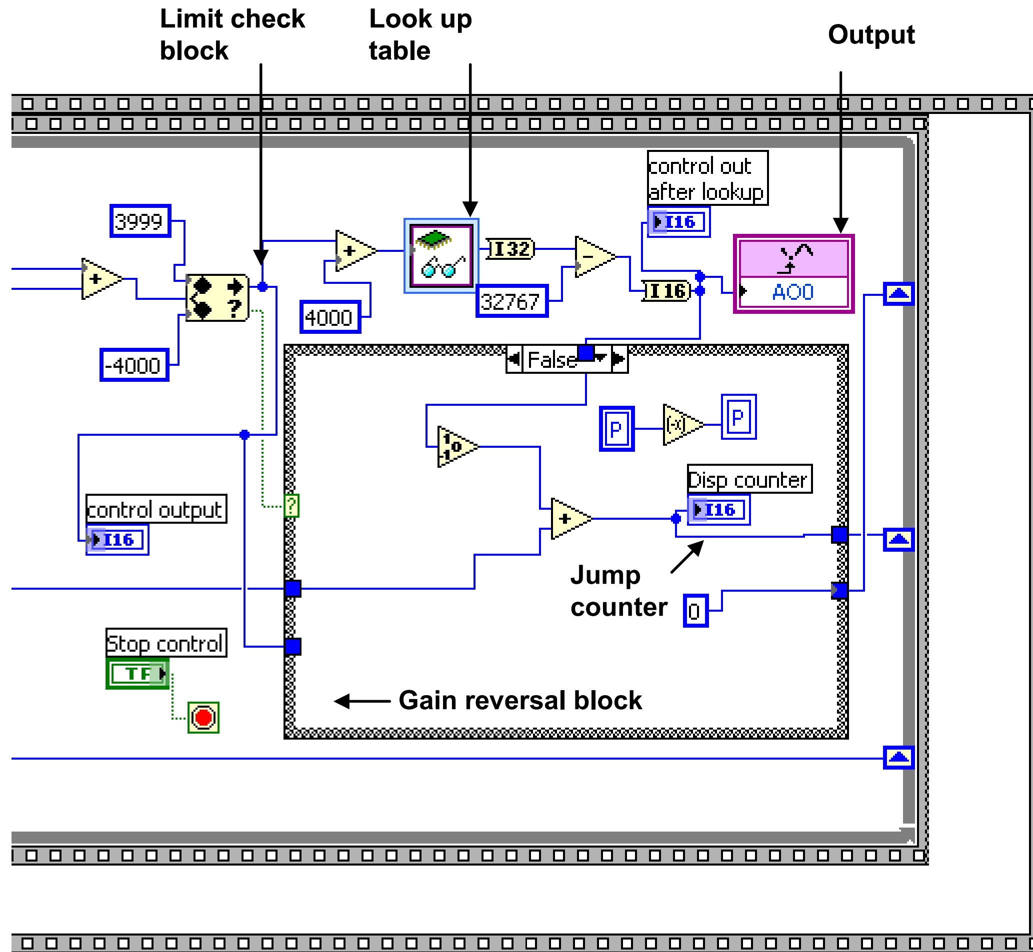

Figure 115 – Step 3- second half of the screen

Figure 114 and Figure 115 show the third step of the program which runs the controller and also implements the gain reversal and non-linearity compensation using look-up table. The controller is fed with the gains and the setpoint obtained from averaging the maximum and minimum PD output. The controller output is truncated at the limits by the limit check blocks. The truncated output is then fed to the look-up table which generates the corresponding grating actuation voltage at the analog output. If the controller output reaches its limits then the gain reversal block activates. This block inverts the gain fed to the controller. It also keeps a count of the jumps with their directions.